A STUDY OF INCLUSIVE NEUTRINO INTERACTIONS IN A MARBLE TARGET

JAAP PANMAN

A STUDY OF INCLUSIVE NEUTRINO INTERACTIONS IN A MARBLE TARGET

ACADEMISCH PROEFSCHRIFT

ter verkrijging van de graad van doctor in de Wiskunde en Natuurwetenschappen aan de Universiteit van Amsterdam, op gezag van de rector magnificus, Dr. D.W.Bresters, hoogleraar in de Faculteit der Wiskunde en Natuurwetenschappen, in het openbaar te verdedigen in de Aula der Universiteit (tijdelijk in de Lutherse Kerk, ingang Singel 411, hoek Spui) op woensdag 16 september 1981 des namiddags te 13.30 uur.

door

JACOB KLAAS PANMAN
geboren te Groningen

promotor : Prof. dr. A.N.Diddens

co-referent : Prof. dr. J.C.Kluyver

The work described in this thesis is part of the research programme of the "Nationaal Instituut voor Kernfysica en Hoge-Energiefysica (NIKHEF)". The author was financially supported by the "Stichting voor Fundamenteel Onderzoek der Materie (FOM)".

CONTENTS

INTRODUCTION

In this thesis results of the analysis of neutrino interactions obtained with the electronic detector of the CHARM (Amsterdam-CERN-Hamburg-Moscow-Rome [1]) collaboration are described. An experimental study of the structure of the weak neutral-current interaction and of the structure of nucleons will be reported.

The detector was designed for the study of neutrino interactions at the CERN (European Organization for Nuclear Research, Geneva, Switzerland) Super Proton Synchrotron (SPS). The main design aim was to optimize the detector for the measurement of neutral-current interactions (muonless events), although also charged-current interactions (events with a muon in the final state) can be studied. The requirement of the measurement of the energy and the direction of the energy-flow of hadronic showers led to the choice of marble as target material.

The neutrino is a point-like particle which has only weak interactions and is therefore an extraordinary tool to study these interactions. In addition, the internal structure of nucleons can be studied with neutrino scattering experiments. The advantage of the use of neutrinos as probes is the simple form of the interaction and the large momentum transfers which can be obtained. Furthermore, the use of weakly interacting probes makes it possible to study the distribution of matter and antimatter in the nucleon separately. The price one has to pay is the low cross-section of neutrinos.

High-energy accelerators have made the study of neutrino interactions possible. The experimental verification of the muon-associated neutrino as a second kind of neutrino in 1962 [2] and the discovery of the neutral-current in 1973 [3] were important results. The linear rise of the neutrino cross-section made it possible to perform more quantitative measurements at the higher-energy accelerators of FNAL (Fermi National Accelerator Laboratory, Batavia, USA) and CERN, providing neutrino beams of a few hundred GeV. Bubble chambers (e.g. the Fermilab 15 foot bubble chamber [4], and the Gargamelle (GGM) [5] and BEBC (Big European Bubble Chamber) [6] bubble chambers at CERN) have contributed a lot to the understanding of neutrino interactions. The inclusive character of the measurements opened the way for the large electronic detectors of the CITF (California Institute of Technology-Fermilab) [7] and HPWF (Harvard-Pennsylvania-Wisconsin-Fermilab) [8] collaborations. The HPWF and CITF experiments used a separate hadron calorimeter and muon spectrometer.

These first generation high-energy neutrino experiments have contributed to the succes of the quark-parton model. The first experimental indication of the existence of partons in the proton was obtained by electron scattering experiments at SLAC (Stanford Linear Accelerator Center, Stanford, USA) in 1968 [9]. Further evidence strongly supporting the quark-parton model was provided by the low-energy neutrino experiments at the CERN PS (Proton Synchrotron) in the early 1970's. After the start of the operation of the neutrino beams at the CERN SPS (Super Proton Synchrotron) in 1977 the high-statistics measurements of the CDHS (CERN-Dortmund-Heidelberg-Saclay) [10] collaboration were reported in 1977 and subsequent years, where an electronic detector was used which merged the functions of calorimeter and muon spectrometer into magnetized iron toroids.

Different experimental groups have made different choices of target mass and measurement precision. On one side there are the bubble chambers with a moderate mass, which can study exclusive properties of the interactions. On the other side are the massive calorimeters which see less details, but provide high event rates. These massive counter experiments measure usually only

the hadronic energy and the kinematic variables of the outgoing muon in charged-current interactions. In the experiment of the CHARM collaboration described in this thesis a compromise is chosen between the two previously mentioned types of experiments. Although in addition to the variables usually measured by counter experiments also the direction of the hadronic energy-flow is measured, still only inclusive studies are possible. The fine spatial resolution enables one to separate events induced by neutral-current and charged-current processes on an event-by-event basis for a large kinematic region, larger than the region explored by iron calorimeters, but comparable to the domain available to bubble chambers. As a consequence the target mass is smaller than that of iron calorimeters, thus providing a lower event rate, which is nevertheless still significantly higher than the event rates obtained in bubble chambers.

The different characteristics of the various experiments are complementary to each other. Furthermore, the analysis is usually not straightforward, and different groups choose different options. Results on the same issues are obtained with completely different systematic uncertainties, which provide an important check on the results.

The CHARM detector has already been used for a wide range of experimental studies. Results on the inverse muon decay reaction [11], the polarization of muons produced in charged-current neutrino interactions [12] (a joint experiment with the CDHS collaboration), prompt neutrino production in 400 GeV proton nucleus interactions [13], neutral-current and charged-current neutrino cross-sections [14], and y-distributions of neutral-current and charged-current neutrino interactions [15] were already reported.

This thesis is organized as follows. In chapter 1 an introduction to the present theory of weak interactions is given, followed by an introduction to the quark-parton model and its consequences for neutrino interactions. The neutrino beam used in this experiment is described in chapter 2. Chapter 3 deals with the neutrino detector of the CHARM collaboration. In chapter 4 the reconstruction program used in the analysis is described. Finally, in chapter 5 the results of the analysis are given. In this chapter results on total cross-sections of both neutral-current and charged-current interactions of neutrinos and antineutrinos and differential cross-sections of charged-current interactions are given.

Chapter 1

THEORY

1.1 WEAK INTERACTIONS

1.1.1 Early theories of the weak interaction

In the early 1970's the weak interaction phenomena were well described by the V-A theory, or better its current x current generalization. In this theory, the effective Lagrangian has the form

$$L_{eff} = \frac{G}{\sqrt{2}} \cdot J_\lambda(x) \cdot J^{\lambda\dagger}(x)$$

with the Fermi coupling constant G. The current $J_\lambda(x)$ appearing in this equation is the sum of a leptonic and hadronic part both being of V-A structure:

$$J_\lambda = \mu \cdot \gamma_\lambda \cdot (1 + \gamma_5) \cdot \nu_\mu + e \cdot \gamma_\lambda \cdot (1 + \gamma_5) \cdot \nu_e + u \cdot \gamma_\lambda \cdot (1 + \gamma_5) \cdot [d \cdot \cos\theta_c + s \cdot \sin\theta_c]$$

in terms of the lepton fields μ, ν_μ, e, ν_e and the quark fields u (up), d (down) and s (strange). The rotation through the Cabibbo angle θ_c [16] in the last term describes the concept that the quarks of the strong interaction are not the eigen-states of the weak interaction.

The Lagrangian, providing a good description of the data in lowest order calculations, gives divergent results in next to lowest order diagrams, e.g. in the case of the diagram in fig.1(a) contributing to the lowest order diagram in fig.1(b), the integral over the internal loop is divergent.

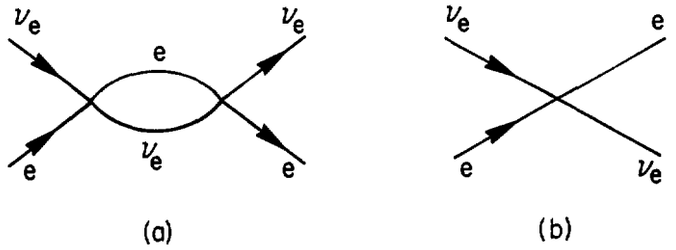

Figure 1: Contributions to $\nu_e e \to \nu_e e$.

However, also the first order diagram in fig.1(b) yields on dimensional grounds a cross-section $\sigma \simeq G^2E^2$ which will eventually violate unitarity at centre-of-mass energies around 600 GeV.

In analogy to the theory of electromagnetic interactions, quantum electrodynamics (QED), where these effects are damped by the photon propagator, one may introduce an intermediate charged vector boson: W. In order to yield the same succesful low-energy behaviour as the current x current theory this intermediate boson has to be massive (say $M_W > 10$ GeV). The low-energy results are restored with the definition of the dimensionless coupling constant, g:

$$\frac{g^2}{8M_W^2} = \frac{G}{\sqrt{2}}$$

(in the limit $Q^2 \ll M_W^2$). The diagram of fig.1(b) is modified into the diagram of fig.2 and its amplitude at high energies is damped by the boson propagator.

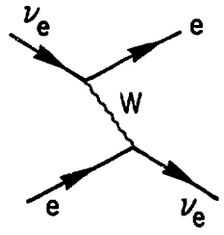

Figure 2: The lowest order diagram of $\nu_e e \to \nu_e e$ with boson propagator.

However, the analogy with QED is not complete; while the photon is massless, the vector W-bosons have a large mass, and consequently a longitudinal polarization mode. It is this longitudinal degree of freedom which causes diagrams like the one shown in fig.3(a) to yield infinite amplitudes.

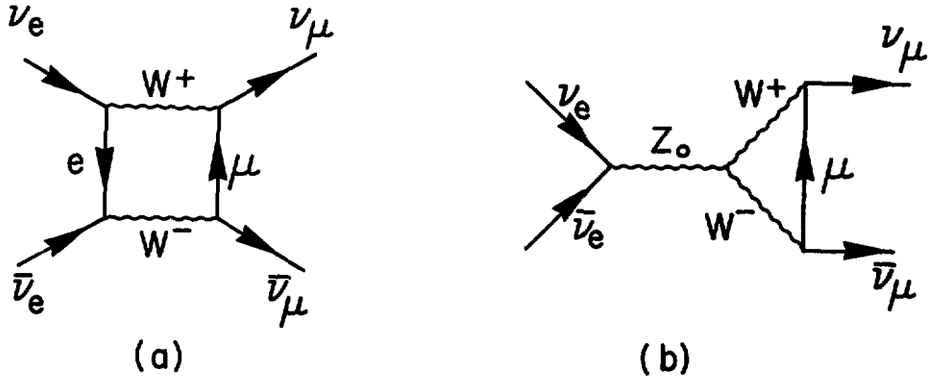

Figure 3: Possible contributions to the ν_e-$\bar{\nu}_e$ cross-section.

One way of curing this problem is to add a neutral vector boson field Z_0. With a suitable choice of the coupling constants, the graph of fig.3(b) cancels the divergences of the previous one. These coupling constants emerge naturally in gauge theories like the Glashow-Salam-Weinberg model [17]. Some properties of this model will be discussed below in more detail.

1.1.2 GIM-mechanism

In the intermediate vector boson theory, the current

$$u\gamma_\lambda\cdot(1 + \gamma_5)\cdot(d\cdot\cos\theta_c + s\cdot\sin\theta_c)$$

gives effective strangeness-changing neutral-currents, which are not observed experimentally with the expected strength. The decay $K^0_1 \to \mu^+\mu^-$ would occur through the diagram in fig.4(a) with rates comparable to the charged kaon decay $K \to \mu\nu$.

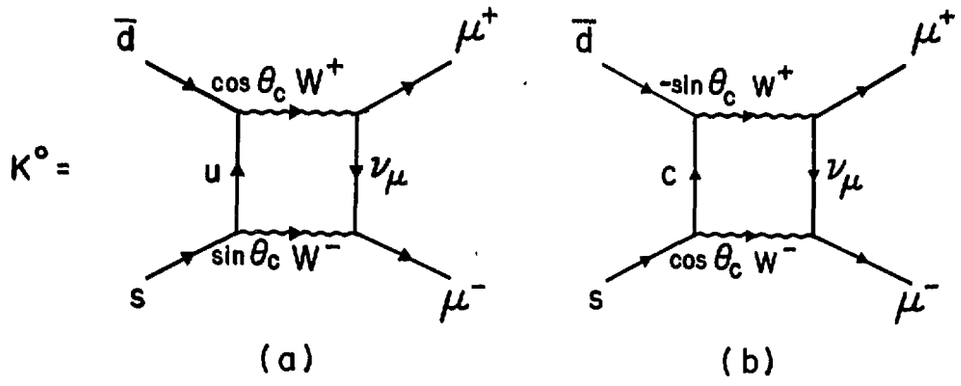

Figure 4: Contributions to $K^0_1 \rightarrow \mu^+\mu^-$.

It was realized by Glashow, Iliopoulos, and Maiani [18], that the introduction of a fourth quark, the charmed (c) quark, with charge +2/3 possessing a new quantum number, would cure this problem (GIM-mechanism). In the example the u-exchange line can then also be replaced by a c-exchange (fig.4(b)). With properly chosen coupling constants this new diagram cancels the old one sufficiently to explain the observed rates when the mass of the charmed quark is not larger than a few GeV. With the introduction of the fourth quark the weak hadronic-current has two terms:

$$\begin{aligned} &u\gamma_\lambda\cdot(1+\gamma_5)\cdot(d\cdot\cos\theta_c + s\cdot\sin\theta_c) \\ &c\gamma_\lambda\cdot(1+\gamma_5)\cdot(s\cdot\cos\theta_c - d\cdot\sin\theta_c) \end{aligned} \qquad (1)$$

corresponding to two families of quarks, (u,d) and (s,c). The most important term in the diagrams of fig.4 is the lowest order term, which is independent of the quark masses. From the formulation of the hadronic-current in equation (1) follows that the diagram with the u-exchange has a coefficient $\cos\theta_c\cdot\sin\theta_c$, whereas the c-exchange has a coefficient $-\sin\theta_c\cdot\cos\theta_c$, thus cancelling the u-exchange diagram. The next to lowest order term depends on the masses and the experimentally observed decay rates are explained if the mass difference of the charm and up-quark is not larger than a few GeV.

1.1.3 The standard theory of electromagnetic and weak interactions

The standard Glashow-Salam-Weinberg [17] theory of electroweak interactions is a gauge theory based on local gauge symmetries. The theory is renormalizable. This means that, once a finite number of infinities having been absorbed in suitably chosen physical constants, the calculation of physical processes yields finite results. It was well known that gauge theories involving only massless fields are renormalizable. It was shown by 't Hooft [19], that also gauge theories with massive fields can be renormalized if the masses are introduced by a mechanism of spontaneous symmetry breaking.

The lepton part of the standard theory is based on the observations:

1. There are only left-handed charged leptonic-currents, which connect e.g. the electron-type leptons only to each other, and not to the muon-type or other leptons (separate lepton number conservation).

2. Electric charge is conserved.

These properties are obtained by the assignment of weak-isospin, $\vec{T}$ and weak-hypercharge, Y. Using the electron-type leptons as an example:

A left-handed doublet, with $\vec{T} = 1/2$

$$L = 1/2 \cdot (1 + \gamma_5) \cdot \begin{bmatrix} \nu_e \\ e \end{bmatrix}$$

The third component $T_3 = +1/2$ is assigned to the neutrino and $T_3 = -1/2$ to the electron.

A right-handed singlet, with $\vec{T} = 0$.

$$R = 1/2 \cdot (1 - \gamma_5) \cdot e$$

The hypercharge is determined by the electric charge, Q, and the relation

$$Q = T_3 + Y/2$$

A similar assignment holds for muon-type leptons. For simplicity the τ-type leptons are ignored here.

The quark sector is built in a similar way grouping u and d′-quarks and c and s′-quarks in left-handed singlets u, d′, c, s′. The quarks heavier than charm are ignored here. The GIM mechanism is incorporated in the model, and d′ and s′ stand for the Cabibbo mixed states:

$$d' = d \cdot \cos\theta_c + s \cdot \sin\theta_c$$

$$s' = s \cdot \cos\theta_c - d \cdot \sin\theta_c$$

where d and s denote the eigen-states of the strong interactions. The assignment of quantum numbers is summarized in table 1.

The weak-isospin and weak-hypercharge symmetries of the Lagrangian correspond to the composite gauge group

$$G = SU(2) \times U(1)$$

To both symmetry groups correspond a vector boson field, with a different coupling constant: g for the SU(2) group, and g′ for U(1). We have:

1. Three W-bosons corresponding to the SU(2) group. One of them is neutral, the other two are charged.

2. One B^0-boson corresponding to the U(1) group.

The neutral W mixes with the B-field and yields two orthogonal states. One state is massless and is identified with the photon. The other is a heavy neutral particle responsible for the weak neutral-current interaction. The coupling constants corresponding to these fields are also combinations of the two different constants of the two groups.

The physical intermediate vector bosons in the theory are:

2 massive charged bosons, W^+ and W^-,

1 massive neutral boson, Z^0, and

1 massless neutral boson, the photon.

The interaction Lagrangian is a sum of the usual weak charged-current interaction, the electromagnetic interaction and the weak neutral-current interaction:

$$L_{interaction} = L_{cc} + L_{em} + L_{nc}$$

The coupling constants of these interactions are given below.

1. The charged-current couples with the constant g of the SU(2) group and is left-handed. The V-A theory is restored in the low-energy limit with the following relation between the Fermi constant, G, and the W-mass, M_W,

$$G/\sqrt{2} = g^2 / 8M_W^2 \qquad ; \; G = (1.16632 \pm 0.00004)\; 10^{-5}\; GeV^{-2}$$

2. The electromagnetic interaction is a pure vector interaction. The usual electromagnetic interaction is restored by the relation:

$$e = gg' / \sqrt{(g^2+g'^2)} \qquad ; \; e^2 = 4\pi\alpha = 4\pi/(137.03604 \pm 0.00011)$$

Hence the two coupling constants are constrained by this relation and there is only one free parameter left. Commonly this parameter is the electroweak mixing angle, θ, defined by

$$\tan\theta = g' / g$$

In terms of this parameter the electron charge is

$$e = g \cdot \sin\theta = g' \cdot \cos\theta$$

3. The weak neutral-current interaction is a mixture of left-handed and right-handed currents. The couplings are usually given relative to the charged-current coupling, and are determined by the weak-isospin and charge quantum numbers. The left-handed and right-handed coupling constants are:

$$\epsilon_l = T_3 - Q \cdot \sin^2\theta$$

$$\epsilon_r = \quad - Q \cdot \sin^2\theta$$

In table 1 these chiral coupling constants are worked out for the elementary fermions. In the following the notation u_l and u_r will be used for the left-handed and right-handed coupling constants of the up-quark, and similarly d_l and d_r for the down-quark.

TABLE 1
Chiral coupling constants predicted in the standard theory.

		left-handed		right-handed	
	Q	T_3	ϵ_l	T_3	ϵ_r
ν_e, ν_μ	0	1/2	1/2	-	-
e, μ	-1	-1/2	$-1/2+\sin^2\theta$	0	$\sin^2\theta$
u, c	2/3	1/2	$1/2-2/3\cdot\sin^2\theta$	0	$-2/3\cdot\sin^2\theta$
d, s	-1/3	-1/2	$-1/2+1/3\cdot\sin^2\theta$	0	$1/3\cdot\sin^2\theta$

The masses of the heavy bosons are predicted in the theory; neglecting radiative corrections one finds

$$M_W = \sqrt{\left[\frac{\sqrt{2}\cdot e^2}{8G}\right]} \cdot \frac{1}{\sin\theta} = \frac{37.3\ GeV}{\sin\theta}$$

$$M_Z = \frac{M_W}{\cos\theta} = \frac{37.3\ \text{GeV}}{\sin\theta\cdot\cos\theta}$$

1.1.4 Measurement of $\sin^2\theta$ in inclusive neutrino interactions

The standard model of weak interactions contains only one free parameter: $\sin^2\theta$. This parameter can be measured in neutrino experiments. In addition, tests of the validity of the model can be made. These measurements are based on the determination of total cross-sections for charged-current and neutral-current processes in both neutrino and antineutrino interactions [20]. We use the definitions:

$$R = \frac{\sigma(\nu N \to \nu X)}{\sigma(\nu N \to \mu^- X)}$$

$$\bar{R} = \frac{\sigma(\bar{\nu} N \to \bar{\nu} X)}{\sigma(\bar{\nu} N \to \mu^+ X)}$$

$$r = \frac{\sigma(\bar{\nu} N \to \mu^+ X)}{\sigma(\nu N \to \mu^- X)}$$

There are several ways to extract $\sin^2\theta$ from a measurement of R, $\bar{R}$ and r, a model-independent method, in which R, $\bar{R}$ and r are used, and a model-dependent method, where the measurement of r is not needed. Both methods will be described below.

The model-dependent determination

In this method a value of R and $\bar{R}$ is predicted for different values of $\sin^2\theta$, and compared with the measurements. An additional model of the differential cross-section is needed to predict the values of R and $\bar{R}$ for a fixed value of $\sin^2\theta$. For this purpose a model based on the quark-parton model [21] will be used. The cross-sections are integrated over the beam-spectrum, taking the experimental cuts into account.

The charged-current (CC) cross-sections are independent of $\sin^2\theta$. The neutral-current (NC) cross-sections are calculated for different values of the parameter. The various cross-sections are calculated within the frame-work of the quark-parton model with quantum chromodynamic corrections included.

In this model, the total cross-sections of interest are incoherent sums of the cross-sections of the constituent quarks. The quark momentum distribution functions are parametrized following Buras and Gaemers [22], slightly modified by Kim et al. [23]. This parametrization will be described in more detail in a following section. These functions describe the quark-structure of the nucleon as seen at different four-momentum transfers. The free parameters of the model of nucleon structure are adjusted to fit the available data on structure functions obtained in charged-current neutrino interactions and electron-proton and muon-proton interactions.

The uncertainties of the parametrization of the structure functions introduce an uncertainty in the determination of $\sin^2\theta$. Kim et al. estimate an uncertainty of 0.009 on the value of $\sin^2\theta$ introduced by these model uncertainties.

The model-independent determination

In this method a suitable combination of the total cross-sections is used, in which model-dependent corrections are kept small. In return the measurement of r is needed in addition to R and $\bar{R}$. It was first noticed by Paschos and Wolfenstein [24] that for targets which can be considered as having isospin zero the following general result holds:

$$\frac{\sigma(\nu \to \nu) - \sigma(\bar{\nu} \to \bar{\nu})}{\sigma(\nu \to \mu^-) - \sigma(\bar{\nu} \to \mu^+)} = 1/2 - \sin^2\theta \qquad (2)$$

This relation follows from general isospin arguments and holds for the differential cross-sections as well. It is therefore possible to apply cuts in the data, provided the same cuts are taken in the numerator and the denominator. The equation is valid in the presence of scaling violations, provided the experimental beam spectra are the same for neutrinos and antineutrinos. This condition is usually not satisfied in the experiments. The equation is not strictly valid due to the kinematic suppression of charmed and even strange quarks. These threshold effects play a role to the extent that the neutrino and antineutrino beam spectra are different.

The uncertainty introduced by these effects can be estimated with the use of the parametrization of the structure functions of Kim et al. [23] introduced above. We estimate an uncertainty of 0.008 on the value of $\sin^2\theta$, in agreement with the calculations of Paschos [25].

1.1.5 Tests of the theory

The particular choice made in the Glashow-Salam-Weinberg model for the mechanism of symmetry breaking fixes the mass relation

$$M_Z = M_W / \cos\theta$$

This is equivalent to the statement that neutral and charged-currents have equal strength. In the more general case, going beyond the Glashow-Salam-Weinberg model, the relative strength of NC and CC interactions is given by an additional free parameter, ρ, which is defined by

$$\rho = \left[\frac{M_W}{M_Z \cdot \cos\theta} \right]^2$$

This parameter is equal to one in the standard theory.

In a quark-parton like model, with vanishing Cabibbo angle (neglecting the strange and charmed sea) the relations

$$g_l^2 = \rho^2 \cdot (u_l^2 + d_l^2) = \frac{R - r^2 \cdot \bar{R}}{1 - r^2} \qquad (3)$$

$$g_r^2 = \rho^2 \cdot (u_r^2 + d_r^2) = \frac{\bar{R} - R}{(1/r) - r} \qquad (4)$$

hold for the left-handed and right-handed neutral-current coupling constants. Here u_l, d_l (u_r, d_r) are the left(right)-handed coupling constants of the up and down-quark, given for the standard model in table 1.

These equations are only valid for the total inelastic cross-section ratios. Hence the ratios appearing in these equations must be corrected for experimental cuts. In addition, a correction has to be made for the contribution of the strange and charmed quarks to the cross-section.

The equations (3) and (4) are readily derived with the use of the quark-parton model. A justification of the notations will be given in a following section. With the assumption that only up and down quarks contribute, we can write for the isoscalar cross-sections

$$\sigma(\nu \to \mu^-) = A \cdot (q + \bar{q}/3)$$
$$\sigma(\bar{\nu} \to \mu^+) = A \cdot (\bar{q} + q/3)$$
$$\sigma(\nu \to \nu) = A \cdot \{g_l^2 \cdot (q+\bar{q}/3) + g_r^2 \cdot (\bar{q}+q/3)\}$$
$$\sigma(\bar{\nu} \to \bar{\nu}) = A \cdot \{g_r^2 \cdot (q+\bar{q}/3) + g_l^2 \cdot (\bar{q}+q/3)\}$$

in which q is the quark content and $\bar{q}$ the antiquark content of the nucleon, and A is a single constant. The factors 1/3 follow from general helicity arguments, and the assumption that only V and A currents contribute. Thus the neutral-current cross-sections can be written in terms of the charged-current cross-sections and the coupling constants:

$$\sigma(\nu \to \nu) = g_l^2 \cdot \sigma(\nu \to \mu^-) + g_r^2 \cdot \sigma(\bar{\nu} \to \mu^+)$$
$$\sigma(\bar{\nu} \to \bar{\nu}) = g_r^2 \cdot \sigma(\nu \to \mu^-) + g_l^2 \cdot \sigma(\bar{\nu} \to \mu^+)$$

With these simple expressions we find the following relations for the neutral to charged-current cross-section ratios in terms of the coupling constants and the charged-current cross-section ratio r:

$$R = g_l^2 + g_r^2 \cdot r$$
$$\bar{R} = g_l^2 + g_r^2 \cdot (1/r)$$

Solving this equations for g_l^2 and g_r^2 yields equations (3) and (4). With the following relations for the coupling constants, which follow from table 1:

$$u_l^2 + d_l^2 = (1/2) - \sin^2\theta + (5/9) \cdot \sin^4\theta \qquad (5)$$
$$u_r^2 + d_r^2 = (5/9) \cdot \sin^4\theta \qquad (6)$$

and $\rho = 1$ for the Glashow-Salam-Weinberg model, the Paschos-Wolfenstein relation (2) is obtained for the total cross-sections.

Unlike the measurement of $\sin^2\theta$, which is a free parameter of theory, a measurement of ρ tests the theory. ρ and $\sin^2\theta$ can be extracted separately from the data. They can be written in terms of g_l and g_r:

$$\rho = \sqrt{((9/5) \cdot g_r^2)} + \sqrt{(2 \cdot g_l^2 - (1/5) \cdot g_r^2)} \qquad (7)$$

$$\sin^2\theta = \left[1 + \sqrt{(1 + (10/9) \cdot [(g_l/g_r) - 1])} \right]^{-1} \qquad (8)$$

which follows from equations (3), (4), (5), and (6).

1.2 DEEP INELASTIC NEUTRINO NUCLEON SCATTERING

1.2.1 Notation

The notation used for the kinematics of the inclusive charged-current neutrino nucleon reaction

$$\nu + N \to \mu + X$$

is most easily given with the use of fig.5. X stands for any hadronic final state.

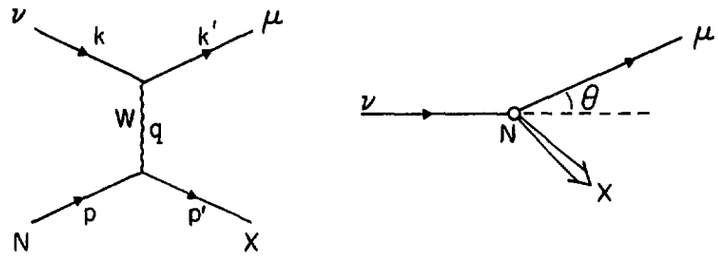

(a) Diagram (b) Laboratory frame

Figure 5: Diagram (a) of the neutrino-nucleon interaction, and (b) the interaction in the laboratory system.

The definitions used in the following are:

k, k'	four-momenta of neutrino and muon.
p, p'	four-momenta of incoming nucleon and the outgoing hadronic final state.
$k-k'$	four-momentum transfer.
E	neutrino energy in the laboratory frame.
E_μ	muon energy in the laboratory frame.
M	rest mass of the nucleon.
E_h^{tot}	total energy of hadronic final state in the laboratory system.
θ	angle of muon with respect to neutrino direction in the laboratory system.
$Q^2 = -(k-k')^2 \simeq 2E \cdot E_\mu \cdot (1-\cos\theta)$:	the second equality holds for a negligible muon mass.
$\nu = p \cdot q/M = E - E_\mu = E_h^{tot} - M$	
$W^2 = (p+q)^2 = M^2 + 2M\nu - Q^2$:	the squared invariant mass of the hadronic final state.

Two dimensionless variables, usually called scaling variables, are:

$$x = Q^2/2M\nu$$
$$y = \nu/E$$

The hadronic energy measured with calorimetric techniques is more closely related to ν than to $E_h^{tot} = \nu + M$. In the following we use the experimentalists' jargon and define

$$E_h \equiv \nu$$

Three variables are sufficient to describe the interaction; we will use most frequently E, x, y. However, sometimes the physics will be more transparent with the use of E, Q^2 and ν.

1.2.2 Kinematic domain

The kinematic region probed in neutrino experiments is limited by the maximum neutrino energy, E_{max}, available. This is shown in the Q^2-ν plot of fig.6(a). The physical region is given by the requirements:

1. $x \leq 1$ or $W^2 \geq M^2$ giving the condition $Q^2 \leq 2M\nu$ (contour a).

2. $|1-\cos\theta| \leq 1$ giving the condition $Q^2 \leq E_{max}\cdot(E_{max}-\nu)$ (contour b) $\nu < E_{max} - Q^2/2E_{max}$, and

3. $Q^2 > 0$.

The contour $W^2 = M^2$ (or x=1) corresponds to elastic scattering. The inelastic domain is bound by contour a' corresponding to $W^2 = (M+M_\pi)^2$, where M_π is the pion mass. Contours a' and b can only be drawn for a fixed neutrino energy. For the sake of visibility an energy of 20 GeV is chosen to draw the curves in fig.6. In the experiment described in this thesis the maximum neutrino energy is 200 GeV. In the variables x and y these conditions translate to

$$0 < x \leq 1$$

and

$$0 < y \leq \frac{1}{1 + Mx/E_{max}}$$

as shown in fig.6(b). The corresponding contours have corresponding labels in fig.6(a) and 6(b). In practice, the region explored by an experiment is smaller due to acceptance problems near kinematical boundaries.

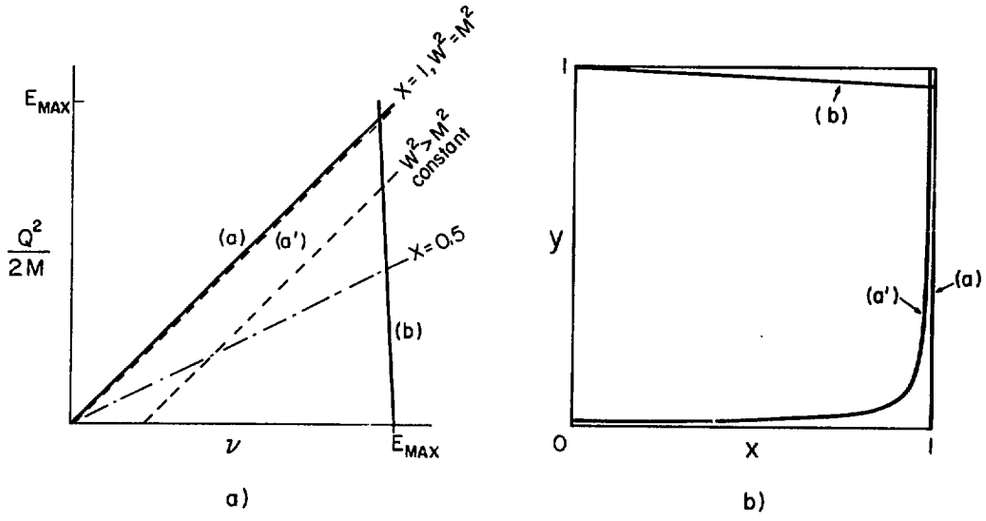

Figure 6: Kinematic domain of neutrino-nucleon scattering, (a) Q^2-ν plot, (b) x-y plot. For explanation see text.

1.2.3 Inclusive cross-section

The double-differential neutrino nucleon inclusive charged-current cross-section, can be written [26]:

$$\frac{d^2\sigma}{dxdy} = \frac{G^2ME}{\pi}\cdot\left[F_2\cdot(1-y-\frac{Mxy}{2E}) + F_1\cdot xy^2 \pm xF_3\cdot y(1-y/2)\right] \qquad (9)$$

for a V-A interaction and a large intermediate boson mass, such that the energy in the centre-of-mass system is small compared to the intermediate boson mass. The structure functions F describe the hadron structure and are a priori different for each process giving in total 12 functions for νn, νp, $\bar{\nu} n$,

$\bar{\nu}p$ scattering. The structure functions depend in general on x and $Q^2 = 2MExy$ (or Q^2 and ν). The third function F_3 contains V,A interference, and its contribution changes sign going from a neutrino beam to an antineutrino beam. The plus sign holds for neutrinos, and the minus sign for antineutrinos. The factor outside the brackets contains a linear dependence on the centre-of-mass energy squared: 2ME. An additional energy-dependence (implied by the Q^2-dependence of the structure functions) can modify the linear energy-dependence of the cross-sections suggested by this factor.

In the following we shall limit ourselves to isoscalar targets, i.e. targets containing equal numbers of neutrons and protons. The 12 functions reduce then to six average functions:

$$F_i^{isoscalar} = (F_i^{proton} + F_i^{neutron})/2$$

The target material used in this experiment, marble ($CaCO_3$), is isoscalar.

1.3 QUARK-PARTON MODEL

1.3.1 Assumptions

The first experimental indication of the existence of point-like particles inside the nucleon was provided by electron scattering experiments performed at SLAC in 1968 [9]. The quark-parton model identifies the quarks introduced as a mathematical tool to describe the properties of hadrons (Spectroscopy, selection rules) [27] with the parton as seen by the electron scattering experiments.

The quark-parton model (QPM) is the subnuclear analogue of the impulse approximation in nuclear physics. The basic assumptions of the QPM are:

1. Hadrons are a collection of point-like partons.

2. Partons behave as if they are free during the interaction with the current; the cross-section is an incoherent sum of single parton contributions.

3. Interactions between partons, at a different time scale, confine partons inside the hadrons.

4. Partons carry the quantum numbers of quarks.

5. The parton masses are negligible.

The quark-parton model was not based on any theoretical justification, the only justification being the good description of the experimental data.

1.3.2 Scaling

Scaling as suggested by Bjorken [28], can be derived without the use of a parton model, in fact it can be derived by dimensional analysis alone. The scaling hypothesis states that in the limit $Q^2 \to \infty$ and $\nu \to \infty$ (keeping the ratio of Q^2 and ν, and thus x constant) the structure functions depend on one dimensionless variable, x, proportional to the ratio of Q^2 and ν, only. Another way of formulating scaling is that the interaction occurs among point-like particles. In order to obtain the scaling limit, the values of Q^2 and ν have to be large compared to any mass-scale involved.

Neglecting Mxy/E, the double-differential cross-section equation (9) can be written in this limit:

$$\frac{d^2\sigma}{dxdy} = \frac{G^2ME}{\pi}\cdot\left[F_2(x)\cdot(1-y) + F_1(x)\cdot xy^2 \pm xF_3(x)\cdot y(1-y/2)\right] \qquad (10)$$

Six isoscalar structure functions, three for neutrino interactions and three for antineutrino interactions, are needed to describe the isoscalar cross-sections. This formulation of the cross-section shows the most important consequences in a transparent way.

1. The factor in square brackets has no explicit or implicit E-dependence; the cross-section rises linearly with the neutrino energy.

2. The y-distributions are described by second order polynomials in y, and do not change with neutrino energy. The structure functions are only weight factors of the terms of the polynomial.

Experimentally it has been discovered that the structure functions scale for Q^2-values as low as a few GeV^2. The fact that this occurs for Q^2-ranges close to the nucleon mass is surprising and is called precocious scaling.

1.3.3 Interpretation of the x-variable in the QPM

The scaling variable x introduced by Bjorken has a simple interpretation in the quark-parton model. With the assumptions that the partons interact as free particles and their mass is negligible, one can derive a simple interpretation of x.

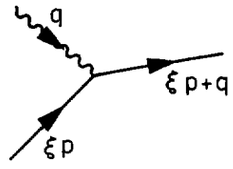

Figure 7: Current-quark interaction.

Let p be the nucleon momentum, ξ the fraction of the momentum carried by the parton, and q the momentum transfer by the current, then (see fig.7) writing the masses of the incoming and outgoing partons as m_i and m_f respectively:

$$m_i^2 = \xi^2 p^2$$

$$m_f^2 = (\xi p + q)^2$$

With both masses equal and negligible with respect to p, one obtains:

$$\xi = \frac{-q^2}{2q\cdot p} = \frac{Q^2}{2M\nu} = x$$

With this interpretation the structure functions are quark-momentum distribution functions in the nucleon. The scaling property of the structure functions states now that for sufficiently large Q^2, such that the nucleon does not interact coherently, the structure of nucleons probed at different Q^2 is the same for constant x.

1.3.4 Callan-Gross relation

For spin 1/2 partons (quarks), with negligible transverse momentum, the Callan-Gross relation [29] holds:

$$F_2(x) = 2xF_1(x) \tag{11}$$

The relation corresponds to a vanishing contribution of the scalar W-absorption cross-section, compared to the right and left-handed cross-sections. Assuming the validity of the Callan-Gross relation the double differential inclusive cross-section (10) simplifies to

$$\frac{d^2\sigma}{dxdy} = \frac{G^2ME}{\pi} \cdot \frac{1}{2} \cdot \left[F_2(x) \cdot \{1+(1-y)^2\} \pm xF_3(x) \cdot \{1-(1-y)^2\} \right] \tag{12}$$

The y-dependence contains only terms proportional to a constant and a $(1-y)^2$ distribution:

$$\frac{d^2\sigma}{dxdy} = \frac{G^2ME}{\pi} \cdot \frac{1}{2} \cdot \left[\{F_2(x) \pm xF_3(x)\} + (1-y)^2 \cdot \{F_2(x) \mp xF_3(x)\} \right] \tag{13}$$

With this relation between F_1 and F_2 we are left with four independent structure functions, two for neutrino (F_2,F_3) and two for antineutrino (F_2',F_3') interactions. A violation of the Callan-Gross relation i.e.

$$R(x) = \frac{F_2(x) - 2xF_1(x)}{F_2(x)} \neq 0$$

adds an extra term inside the square brackets of the form:

$$-\frac{R(x)}{2} \cdot y^2 \tag{14}$$

and provides a way to check the assumptions made.

1.3.5 Interpretation of y-distributions

In the quark-parton picture the basic interaction is the interaction of the neutrino with the constituent quarks. In a V-A theory of the weak-currents the y-dependence of the interaction takes the simple form:

$$\frac{d\sigma}{dy}(\nu q \text{ and } \bar{\nu}\bar{q}) \propto 1$$

for neutrino-quark and antineutrino-antiquark interactions corresponding to an isotropic distribution in the centre-of-mass frame. The interaction of antineutrinos with quarks or neutrinos with antiquarks takes the form:

$$\frac{d\sigma}{dy}(\bar{\nu}q \text{ and } \nu\bar{q}) \propto (1-y)^2$$

corresponding to a suppression for 180 degrees scattering in the centre-of-mass system. This behaviour follows simply from the spin-dependence of the

interaction, and is the same as for neutrino-electron and antineutrino-electron scattering. The spin-dependence of the interaction is given by angular momentum conservation and the fact that both V and A currents conserve helicity.

We write $q(x)/x$ and $\bar{q}(x)/x$ for the probability of finding a quark and an antiquark in a nucleon at a given x. With this notation $q(x)$ and $\bar{q}(x)$ are the momentum distribution functions of quarks and antiquarks in the nucleon. The cross-sections are proportional to the probability of finding a quark or antiquark at a given x, and to the point-like neutrino-quark cross-section. The point-like cross-section is proportional to the centre-of-mass energy squared of the neutrino-quark system, $2ME \cdot x$. In this expression $\sqrt{2ME}$ is the centre-of-mass energy in the neutrino-nucleon system. The factor x enters because x is the fraction of the momentum of the nucleon carried by the struck quark. The neutrino-nucleon cross-section is then proportional to the momentum distribution functions $q(x)$. We obtain for an isoscalar target:

$$\frac{d^2\sigma(\nu N)}{dxdy} \simeq 2ME \cdot \{q(x) + (1-y)^2 \cdot \bar{q}(x)\}$$

$$\frac{d^2\sigma(\bar{\nu}N)}{dxdy} \simeq 2ME \cdot \{q'(x) \cdot (1-y)^2 + \bar{q}'(x)\}$$

The distributions $q(x)$ and $q'(x)$, as probed by neutrinos and antineutrinos respectively, may be different. Neutrinos and antineutrinos probe the amount of quarks and antiquarks in a nucleon separately.

From this formulation of the cross-sections and equation (13) the relation between the quark-momentum distribution functions $q(x)$ and $\bar{q}(x)$ and the structure functions becomes transparent:

$$\begin{aligned} F_2(x) &= q(x) + \bar{q}(x) \\ xF_3(x) &= q(x) - \bar{q}(x) \end{aligned} \qquad (15)$$

for neutrinos and similarly for antineutrinos:

$$\begin{aligned} F_2'(x) &= q'(x) + \bar{q}'(x) \\ xF_3'(x) &= q'(x) - \bar{q}'(x) \end{aligned} \qquad (16)$$

As the quark and antiquark-momentum distribution may be different as probed by neutrinos and antineutrinos, the structure functions can also be different.

1.3.6 Valence and sea-quarks

In the static quark picture of hadron structure, the quantum numbers of baryons are carried by three quarks (introduced to explain the observed selection rules and mass spectra).

Analogous to the valence electrons of atoms, these quarks are usually referred to as "valence-quarks". In the same picture these valence-quarks are surrounded by a cloud of "sea-quarks".

This sea of quarks is created in a similar way to the electron-positron cloud of a charged particle in quantum electrodynamics (QED). The presence of gluon fields mediating the force between quarks gives rise to the production of quark-antiquark pairs and their subsequent annihilation. This process is analogous to vacuum polarization in QED, and yields a sea with equal contributions of quarks and antiquarks.

We introduce the notation $q_s(x)$ and $q_v(x)$ for the momentum-distribution of sea and valence-quarks respectively, and $\bar{q}_s(x)$ and $\bar{q}_v(x)$ for the antiquark distributions. The quantum numbers of nucleons are carried only by quarks, hence for a nucleon

$$q_v(x) \neq 0$$

$$\bar{q}_v(x) = 0$$

and for the sea

$$q_s(x) = \bar{q}_s(x)$$

With the relations:

$$q(x) = q_v(x) + q_s(x)$$

$$\bar{q}(x) = \bar{q}_s(x)$$

and equations (15) and (16), simple interpretations are obtained for the structure functions

$$F_2(x) = q_v(x) + 2q_s(x)$$

$$xF_3(x) = q_v(x) \qquad (17)$$

1.3.7 Relation of cross-sections in the quark-parton model

In the QPM, the inclusive neutrino cross-sections can be written as the sum of contributions of different quark flavours

$$\sigma = \Sigma_i \sigma_i \qquad ; i = u, d, s, c$$

where we limit ourselves to a system of four quark flavours. The neutrino-quark cross-sections factorize in a product of the point-like cross-section proportional to the centre-of-mass energy squared in the neutrino-quark system (see section 1.3.5), $2ME \cdot x$, which gives a cross-section proportional to

$$\frac{G^2 ME}{\pi} \cdot x$$

and the probability of finding a quark of that flavour at a given x in the nucleon, $q_i(x)/x$.

TABLE 2
GIM structure of charged-current neutrino-quark interactions.

$$\begin{aligned}
&\nu d \to \mu^-(\cos^2\theta_c \cdot u + \underline{\sin^2\theta_c \cdot c}) \\
&\nu s \to \mu^-(\underline{\cos^2\theta_c \cdot c} + \sin^2\theta_c \cdot u) \\
&\nu \bar{u} \to \mu^-(\cos^2\theta_c \cdot \bar{d} + \sin^2\theta_c \cdot \bar{s}) \cdot (1-y)^2 \\
&\underline{\nu \bar{c} \to \mu^-(\cos^2\theta_c \cdot \bar{s} + \sin^2\theta_c \cdot \bar{d})} \cdot (1-y)^2 \\
&\\
&\bar{\nu} u \to \mu^+(\cos^2\theta_c \cdot d + \sin^2\theta_c \cdot s) \cdot (1-y)^2 \\
&\underline{\bar{\nu} c \to \mu^+(\cos^2\theta_c \cdot s + \sin^2\theta_c \cdot d)} \cdot (1-y)^2 \\
&\bar{\nu} \bar{d} \to \mu^+(\cos^2\theta_c \cdot \bar{u} + \underline{\sin^2\theta_c \cdot \bar{c}}) \\
&\bar{\nu} \bar{s} \to \mu^+(\underline{\cos^2\theta_c \cdot \bar{c}} + \sin^2\theta_c \cdot \bar{u})
\end{aligned}$$

The quarks appearing in the charged-current cross-sections correspond to the GIM-currents of the electroweak Lagrangian introduced in section 1.1.2. The contributions of the various quark flavours to charged-current interactions are summarized in table 2. The contributions to the cross-sections follow from the fact that a W^+-exchange raises the quark charge by one unit and a W^--exchange lowers it by the same amount. Contributions involving charm-quarks are underlined in the table. The structure functions are composed of all possible contributions of the different quark flavours. Two approximations will be given, one far above the charm threshold, such that kinematic suppression of charm production can be neglected, and one below charm threshold, such that no charm production is considered. The isoscalar structure functions are averages of neutron and proton structure functions. Far above threshold we first write the proton and neutron contribution separately:

$$\begin{aligned}
F_2(\nu p) &= 2x\cdot\{d^p(x) + \bar{u}^p(x) + s^p(x) + \underline{\bar{c}^p(x)}\} \\
F_2(\nu n) &= 2x\cdot\{d^n(x) + \bar{u}^n(x) + s^n(x) + \underline{\bar{c}^n(x)}\} \\
F_2(\bar{\nu} p) &= 2x\cdot\{u^p(x) + \bar{d}^p(x) + \bar{s}^p(x) + \underline{c^p(x)}\} \\
F_2(\bar{\nu} n) &= 2x\cdot\{u^n(x) + \bar{d}^n(x) + \bar{s}^n(x) + \underline{c^n(x)}\} \\
xF_3(\nu p) &= 2x\cdot\{d^p(x) - \bar{u}^p(x) + s^p(x) - \underline{\bar{c}^p(x)}\} \\
xF_3(\nu n) &= 2x\cdot\{d^n(x) - \bar{u}^n(x) + s^n(x) - \underline{\bar{c}^n(x)}\} \\
xF_3(\bar{\nu} p) &= 2x\cdot\{u^p(x) - \bar{d}^p(x) - \bar{s}^p(x) + \underline{c^p(x)}\} \\
xF_3(\bar{\nu} n) &= 2x\cdot\{u^n(x) - \bar{d}^n(x) - \bar{s}^n(x) + \underline{c^n(x)}\}
\end{aligned} \tag{18}$$

The factor two enters because both V and A currents contribute. In contrast to the definition of q(x), which is a momentum distribution function, the flavour probability function $u^p(x)$ is defined as the probability of finding a u-quark in a proton at a given x, and similarly $\bar{u}^p(x)$ for anti u-quarks. The momentum distribution function is then written $x\cdot u^p$. The definitions of $d^p(\bar{d}^p)$, $s^p(\bar{s}^p)$, $c^p(\bar{c}^p)$ are analogous for the d, s and c-quarks. Similarly, u^n denotes the probability function of finding a u-quark in a neutron. The plus and minus signs in equation (18) follow from equation (15) and (16). We have explicitly ignored any Q^2-dependence of the quark-probability functions. The quark probability functions for neutrons and protons are related by isospin symmetry. In the following we use the definitions:

$$\begin{aligned}
u(x) &= u^p(x) = d^n(x) \\
d(x) &= d^p(x) = u^n(x) \\
s(x) &= s^p(x) = s^n(x) \\
c(x) &= c^p(x) = c^n(x)
\end{aligned}$$

with these definitions the isoscalar structure function are written:

$$\begin{aligned}
F_2(\nu N) &= x\cdot\{u(x) + d(x) + \bar{u}(x) + \bar{d}(x) + 2s(x) + 2\underline{\bar{c}(x)}\} \\
F_2(\bar{\nu} N) &= x\cdot\{u(x) + d(x) + \bar{u}(x) + \bar{d}(x) + 2\bar{s}(x) + 2\underline{c(x)}\} \\
xF_3(\nu N) &= x\cdot\{u(x) + d(x) - \bar{u}(x) - \bar{d}(x) + 2s(x) - 2\underline{\bar{c}(x)}\} \\
xF_3(\bar{\nu} N) &= x\cdot\{u(x) + d(x) - \bar{u}(x) - \bar{d}(x) - 2\bar{s}(x) + 2\underline{c(x)}\}
\end{aligned} \tag{19}$$

With the definitions of the probability functions given above the following sum rules hold:

$$\begin{aligned} {}_0\int^1 \{u(x) - \bar{u}(x)\}dx &= 2 \\ {}_0\int^1 \{d(x) - \bar{d}(x)\}dx &= 1 \\ {}_0\int^1 \{s(x) - \bar{s}(x)\}dx &= 0 \\ {}_0\int^1 \{c(x) - \bar{c}(x)\}dx &= 0 \end{aligned} \qquad (20)$$

These rules mean nothing more than that the proton contains three valence-quarks, two u and one d, and that the proton has neither strangeness nor charm.

With the assumption of SU(4) symmetry of quark flavours, expected to be valid at infinite energies, and remembering that u and d-quarks are the valence-quarks of nucleons we write

$$\bar{u}(x) = \bar{d}(x) = s(x) = c(x) = \bar{s}(x) = \bar{c}(x)$$

With these relations we obtain the important result that the structure functions F_2 and xF_3 as seen by neutrinos and antineutrinos are the same:

$$\begin{aligned} F_2^{neutrino}(x) &= F_2^{antineutrino}(x) \\ xF_3^{neutrino}(x) &= xF_3^{antineutrino}(x) \end{aligned} \qquad (21)$$

In this case the structure functions can be obtained by simply adding and subtracting the neutrino and antineutrino x-distributions. From equation (12) follow

$$\frac{d\sigma(\nu N)}{dx} + \frac{d\sigma(\bar{\nu}N)}{dx} = \frac{4G^2ME}{3\pi}\cdot F_2(x) \qquad (22)$$

$$\frac{d\sigma(\nu N)}{dx} - \frac{d\sigma(\bar{\nu}N)}{dx} = \frac{2G^2ME}{3\pi}\cdot xF_3(x) \qquad (23)$$

However, when the neutrino energy is not sufficiently high the mass of the charmed quark cannot be ignored (the effective mass is estimated to be $\simeq$1.5 GeV). Working below charm threshold the s-coupling will be Cabibbo suppressed, also the coupling with the d-quark will be slightly modified. We easily read off from table 2, suppressing the processes including charm, that the structure functions for protons and neutrons separately are obtained from equation (18) with the substitution

$$\begin{aligned} u^i(x) &\to u^i(x) \\ d^i(x) &\to \cos^2\theta_c \cdot d^i(x) \\ s^i(x) &\to \sin^2\theta_c \cdot s^i(x) \\ c^i(x) &\to 0 \end{aligned}$$

where i stands for n,p separately. Similar substitutions hold for the anti-quark distributions. Using these substitutions and averaging over protons and neutrons the following expressions for the structure functions below charm threshold are obtained:

$$
\begin{aligned}
F_2(\nu N) &= x\cdot\{(u+d)\cdot\cos^2\theta_c + 2s\cdot\sin^2\theta_c + (\bar{u}+\bar{d})\} \\
F_2(\bar{\nu}N) &= x\cdot\{(u+d) + 2\bar{s}\cdot\sin^2\theta_c + (\bar{u}+\bar{d})\cdot\cos^2\theta_c\} \\
xF_3(\nu N) &= x\cdot\{(u+d)\cdot\cos^2\theta_c + 2s\cdot\sin^2\theta_c - (\bar{u}+\bar{d})\} \\
xF_3(\bar{\nu}N) &= x\cdot\{(u+d) - 2\bar{s}\cdot\sin^2\theta_c - (\bar{u}+\bar{d})\cdot\cos^2\theta_c\}
\end{aligned}
\qquad (24)
$$

For a zero Cabibbo angle the result of equation (21) is reproduced, and for a non-zero angle the differences are non-zero:

$$
\begin{aligned}
F_2(\nu N) - F_2(\bar{\nu}N) &= \sin^2\theta_c\cdot(\bar{u} + \bar{d} - u - d) \\
xF_3(\nu N) - xF_3(\bar{\nu}N) &= \sin^2\theta_c\cdot(4s - u - d - \bar{u} - \bar{d})
\end{aligned}
\qquad (25)
$$

The structure functions F_2 and $xF_3(x)$ are different for neutrino and antineutrino processes, and in the analysis a correction has to be made when they are obtained by adding and subtracting the neutrino and antineutrino differential cross-sections.

The structure function of the s-quark can be obtained independently from dimuon events. The first observation of dimuon events was reported by the HPWF collaboration [30] and soon confirmed by the CITF collaboration [31]. Dimuon events are attributed to the decay of charmed particles into a muon and a neutrino; the production of charm-quarks off strange-quarks is favoured by the Cabibbo factor $\cos^2\theta_c = 0.95$ for this reaction rather than the factor $\sin^2\theta_c = 0.05$ for the production off down-quarks (see also table 2). The contribution to the total cross-section can also be obtained by a comparison of neutrino and antineutrino y-distributions (see section 1.3.9), and is of the order of ≈5%.

In this experiment the energy-range is such that the situation is expected to be between the two approximations given above. Most of the momentum transfers are above charm threshold, but are not sufficiently high to justify the approximation of SU(4) symmetry.

1.3.8 Gross-Llewellyn-Smith sum rule

The normalizations for the valence-quarks (equation (20)) and the forms obtained for the structure function xF_3 suggest the Gross-Llewellyn-Smith sum rule [32]:

$$
{}_0\int^1 F_3(x)dx = 3
$$

just counting the number of valence-quarks in the nucleon. This equation is expected to be exact in the case of SU(4) symmetry, or in the three-quark SU(3) case for vanishing Cabibbo angle.

1.3.9 The shape parameter of the y-distribution

The y-dependence in the double-differential cross-section can reveal the fraction of the momentum of the nucleon carried by antiquarks, and can give information on the strange-quark content.

Substituting the formulation of the structure functions of equation (19) in terms of the flavour probability functions into the double-differential cross-section (13) and integrating over x yields:

$$\frac{d\sigma(\nu N)}{dy} = A\cdot\{(1-\alpha) + \alpha(1-y)^2\}$$

$$\frac{d\sigma(\bar{\nu}N)}{dy} = A\cdot\{\bar{\alpha} + (1-\bar{\alpha})\cdot(1-y)^2\} \qquad (26)$$

with the assumption of charge symmetry:

$$\left.\frac{d\sigma(\nu N)}{dy}\right|_{y=0} = \left.\frac{d\sigma(\bar{\nu}N)}{dy}\right|_{y=0} \qquad (27)$$

which enables us to use a single normalization constant A. We have defined the shape parameter of the y-distributions:

$$\alpha = \frac{\int x\cdot\{\bar{u}(x) + \bar{d}(x) + 2\bar{c}(x)\}dx}{\int x\cdot(u + d + \bar{u} + \bar{d} + 2s + 2\bar{c})dx}$$

$$\bar{\alpha} = \frac{\int x\cdot\{\bar{u}(x) + \bar{d}(x) + 2\bar{s}(x)\}dx}{\int x\cdot(u + d + \bar{u} + \bar{d} + 2\bar{s} + 2c)dx} \qquad (28)$$

With the usual assumptions we can equate both denominators and we obtain the difference in the shape parameters of the neutrino and antineutrino y-distributions:

$$\bar{\alpha} - \alpha = \frac{2\cdot\int x\cdot\{\bar{s}(x) - \bar{c}(x)\}dx}{\int x\cdot(u+d+\bar{u}+\bar{d}+s+\bar{s}+c+\bar{c})dx} \qquad (29)$$

For a vanishing contribution of the charmed quark we can determine the fractional momentum carried by the strange-quark in the nucleon.

The assumption of charge symmetry (equation (27)) can be tested by comparing the experimentally observed cross-sections $d\sigma/dy$ for neutrinos and antineutrinos at $y = 0$. From equation (12) it follows that only F_2 contributes at $y = 0$; the contribution of xF_3 vanishes at $y = 0$. From the QPM formulation of F_2 one can directly obtain the expected value of $d\sigma/dy$ at $y = 0$. From equation (21) one reads off that charge symmetry is expected to be exact for an SU(4) symmetric model. In the SU(3) symmetric model it is only exact for a vanishing Cabibbo angle (see equation (25)). From the difference of F_2 for neutrinos and antineutrinos compared to the average F_2 (equation (24)), one expects that $d\sigma/dy$ at $y = 0$ is of the order of a few percent higher for antineutrinos compared to neutrinos (with $\sin^2\theta_c = 0.05$, $\alpha \simeq \bar{\alpha} \simeq 0.15$).

1.3.10 Total cross-sections

The measurement of total cross-sections of neutrino and antineutrino interactions can provide information on:

1. The relative momentum fraction carried by antiquarks in the nucleon.
2. The relative momentum carried by partons, which do not couple to the weak interaction.

In the approximation of no strange and charmed sea-distributions, we obtain, by integrating the double-differential cross-section and inserting the quark-parton interpretation of the structure functions (equations (15) and (16)), for the cross-section ratio:

$$r = \frac{\sigma(\bar{\nu} \to \mu^+)}{\sigma(\nu \to \mu^-)} = \frac{\bar{q} + q/3}{q + \bar{q}/3} \tag{30}$$

in which the quark and antiquark contributions are defined:

$$q = \int x\{u(x) + d(x)\}dx$$

$$\bar{q} = \int x\{\bar{u}(x) + \bar{d}(x)\}dx$$

We see immediately:

$$1/3 \leq r \leq 3$$

where the lower limit is reached for vanishing antiquark contribution and the upper limit for vanishing quark contribution. The relative contribution of antiquarks in the nucleon can be obtained by rearranging equation (30) and reads in terms of r:

$$\frac{\bar{q}}{q+\bar{q}} = \frac{1}{2} \cdot \frac{3r-1}{1+r} \tag{31}$$

The sum of the two charged-current total cross-sections gives the momentum sum rule (see equation (22)):

$$\frac{3\pi}{4G^2ME} \cdot \{\sigma(\nu N \to \mu^- X) + \sigma(\bar{\nu} N \to \mu^+ X)\} = {}_0\int^1 F_2(x)dx \tag{32}$$

and is interpreted in the QPM as the total momentum fraction of the nucleon carried by the quarks. The difference from one of this quantity measures the momentum fraction carried by other partons, which do not couple to weak and electromagnetic interactions. The observed non-saturation of the momentum sum rule (equation (32)) shows that around one half of the momentum of nucleons is carried by partons not coupling to electromagnetic and weak interactions. These other partons can be identified with the bosons mediating the force between quarks, the gluons.

1.3.11 Relation to electron-deuteron scattering

With the use of the QPM, the structure function F_2 obtained in electron scattering experiments is related to F_2 obtained in neutrino experiments.

The electromagnetic interaction is parity conserving, and cannot see the difference between quarks and antiquarks, hence the cross-section does not contain the F_3 structure function, which is a result of V and A interference for neutrino scattering.

The electromagnetic-current couples to the charges of the partons. The quark-parton interpretation of the electromagnetic structure function F_2 below charm threshold for an isoscalar target, say deuterium, is then:

$$F_2(eN) = (1/2) \cdot x \cdot [(5/9) \cdot \{u(x) + \bar{u}(x) + d(x) + \bar{d}(x)\} + (2/9) \cdot \{s(x) + \bar{s}(x)\}]$$

The coefficient (5/9) is obtained by adding the squared charges of the u and d-quark. The coefficient (2/9) is twice the squared charge of the s-quark. The overall coefficient (1/2) enters due to the averaging over protons and neutrons. The normalizations defined in equations (20) are used here. The weak-current has V and A parts of equal strength, which gives a factor 2 in the cross-section (section 1.3.7), whereas the electromagnetic-current is only a vector.

With the simplification $\theta_c = 0$ in equation (24) for the neutrino structure functions and the usual assumption of isospin symmetry, the ratio of the electromagnetic and weak structure function for isoscalar targets is:

$$\frac{F_2(eN)}{F_2(\nu N)} = \frac{(5/9)\cdot(u+\bar{u}+d+\bar{d}) + (2/9)\cdot(s+\bar{s})}{2\cdot(u+\bar{u}+d+\bar{d})} \geq \frac{5}{18}$$

The limiting case 5/18 is reached for vanishing strange-quark contributions.

The experimental verification of this ratio is an important check of the basic ideas underlying the QPM. The comparison [33] shows agreement with the factor 5/18 and therefore supports the quark-quantum numbers.

1.3.12 Scale breaking

The property of scaling of the structure functions was derived under the assumption of the absence of any mass-scale comparable to the momentum transfer involved. We have already seen that the non-negligible mass of the charm-quark may play a role for the structure functions.

Upon crossing the charm threshold new channels open up and a change of the structure functions may be expected, corresponding to an SU(4) symmetry far above threshold. The effects of non-negligible masses involved in the process can be represented by a modification of the scaling variable.

Georgi and Politzer [34] have derived such a modified scaling parameter, ξ, which takes all mass effects into account. Scaling in terms of ξ holds when the coupling constant is small, but is independent of mass effects. The modified parameter is:

$$\xi = \frac{Q'^2}{2M\nu} \cdot \frac{2}{1 + \sqrt{(1-Q^2/\nu^2)}} \qquad (33)$$

where

$$2Q'^2 = Q^2 + m_f^2 - m_i^2 + \sqrt{(Q^4 + 2Q^2\cdot(m_f^2 + m_i^2) + (m_f^2 - m_i^2)^2)}$$

in which:

m_i mass of the initial state quark,
m_f mass of the final state quark.

The variable ξ has a simple parton-model interpretation when the struck quark is light. In this limit equation (33) reduces to

$$\xi = \frac{Q^2 + m_f^2}{M\cdot(\nu + \sqrt{(\nu^2+Q^2+m_f^2)})}$$

which is the solution of the constraint that the produced parton is on its mass shell:

$$(\xi p + q)^2 = m_f^2$$

(ξ is here the fraction of the nucleon momentum carried by the parton.) For negligible quark masses this reduces to the Nachtmann [35] variable, describing target mass effects only:

$$\xi = \frac{Q^2}{M\cdot(\nu + \sqrt{(\nu^2+Q^2)})} \qquad ; Q^2 \gg m_i^2,\ m_f^2 \qquad (34)$$

and is only considerably different from x at large x. This form reduces only for small x to the Bjorken scaling variable:

$$\xi \to x = \frac{Q^2}{2M\nu} \qquad ; \nu^2 \gg Q^2 \gg m_i^2,\ m_f^2$$

An other approximation holds for the threshold region of a heavy quark flavour with mass m. In that case $Q^2 \simeq m^2$, the production of the new flavour will be predominantly at low x:

$$\xi = \frac{Q^2 + m^2}{2M\nu} = x + \frac{m^2}{2M\nu} \qquad ; \nu^2 \gg Q^2 \qquad (35)$$

In this case low x does not mean low ξ. With the simple consequence of the parton interpretation, $\xi \leq 1$ and the relation $Q^2 = 2xM\nu$, an upper bound can be derived for x in reactions in which heavy quark flavours are produced:

$$x \leq Q^2 / (Q^2 + m^2)$$

The scaling of the structure functions as a function of ξ means that they are shifted, in terms of x, towards low x, and for Q^2 just larger than m^2 only the tail of the structure functions contributes to the heavy quark production. For increasing Q^2 an increasing fraction of the structure functions shifts now into the physical region $0 < x \leq 1$.

1.3.13 Continuous scale breaking

Scaling is also the consequence of the point-like structure of the particle, as seen by the probe with a necessarily finite resolution. When a new structure is resolved inside the particle, scaling will not hold. This new structure may come in successive discrete layers:

nucleus → nucleon → quark

Scaling is observed for the first layer until its structure is resolved. At sufficiently high Q^2, there will be a rescaling in terms of the new elementary constituents. This new scaling will be violated when the structure of this new constituent is resolved in its turn. Then a rescaling will occur, etc.

However, when the scale breaking is caused by a continuous process, no rescaling will occur. When quarks are surrounded by a virtual cloud of gluons and quark-antiquark pairs such a scale breaking can be introduced. Qualitatively the effects of such a mechanism can be seen from the diagrams drawn in fig.8. The quark in fig.8(a) is seen by the current with a momentum fraction x. In fig.8(b) the momentum transfer is higher and makes the bremsstrahlung process more probable. The quark radiates a gluon, and shares its momentum with the gluon. A fraction y ($y < 1$) of the quarks original momentum fraction x is kept by the quark. Consequently, the gluon obtains the fraction 1-y of x. The quark is now seen by the current with a reduced fraction $xy < x$.

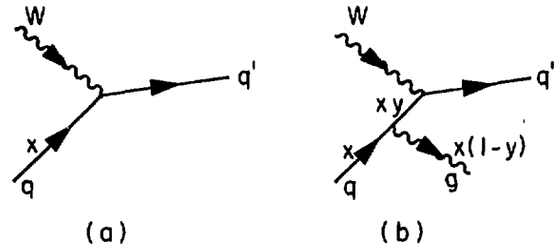

Figure 8: Current-quark interaction without (a) and with (b) gluon bremsstrahlung.

This mechanism changes the structure functions; these functions become larger at small x and smaller at large x (they shrink towards x = 0).

1.4 QUANTUM CHROMODYNAMICS

The electromagnetic and weak interactions can be described by a gauge theory. We shall discuss a gauge theory for strong interactions. The successes of the QPM suggest a theory in which quarks are asymptotically free at large momentum transfers. On the other hand, the theory of strong interactions has to explain why quarks are not seen as free particles. Although one hopes that the theory provides this quark confinement, it is certainly not proven.

The building blocks of the theory are the quarks of the QPM and vector bosons, gluons. Quarks and gluons carry colour charges analogous to the electric charge of quantum electrodynamics (QED).

However, there are some basic differences in the comparison of colour and electric charge.

1. There are three colours (and three anticolours) as opposed to only one electric charge.

2. Photons are neutral, gluons carry colour charges. This means that gluons couple to each other.

An important axiom is that hadrons are colour singlets, "white". For baryons this is achieved by a state containing three quarks, each a superposition of three colours; mesons are made of a quark and an antiquark carrying a colour and its anticolour. The SU(3) of colour is an exact symmetry, so that the three colour states are degenerate. Gluons are thought to be massless, which together with exact colour symmetry leads to a renormalizable theory. This field theory is called quantum chromodynamics (QCD). There are indications of the existence of three colours, some of these are:

The e^+e^- annihilation cross-section is roughly three times as large as expected for colourless quarks.

The π^0 decay width into two photons is explained by three colours.

Colour provides a way to form a totally antisymmetric wave function for the Δ^{++}.

As compared to QED a new feature of the theory is the gluon-gluon coupling.

The coupling constant of QCD is a running coupling constant; its value depends on the momentum transfer. The effective coupling constant, calculated to first order, reads in terms of the mass-scale Λ, a free parameter in the theory [36]:

$$\alpha_s(Q^2) = \frac{12\pi}{(33-2f)\cdot\log(Q^2/\Lambda^2)} \qquad (36)$$

where f is the number of quark flavours. For less then 16 quark flavours, this form shows the asymptotic freedom property, small coupling at large Q^2, as is required by renormalizability.

At $Q^2 \simeq \Lambda^2$ the coupling becomes very large, and the perturbation theory approach is not applicable. At this point it is hoped that the non-perturbative part of the theory will take care of confinement.

The mass parameter Λ emerges even in a massless theory, massless quarks and massless gluons. As mentioned, the equation (36) gives the value of $\alpha_s(Q^2)$ in a first order perturbation expansion. However, at present energies the value of α_s is large enough to suspect important contributions of higher order terms. In second order the form of α_s will be [36]:

$$\alpha_s(Q^2) = \frac{12\pi}{(33-2f)\cdot\log(Q^2/\Lambda'^2)}\cdot\left[\,1 - \frac{\beta_1\cdot\log\log(Q^2/\Lambda'^2)}{\beta_0^2\cdot\log(Q^2/\Lambda'^2)}\,\right] \qquad (37)$$

where $\beta_1 = 102 - (38/3)f$ and $\beta_0 = 11 - (2/3)f$. It is clear from equation (36) and (37) that the functional forms of α_s in terms of Λ and Λ' are different, and that it matters whether the first or second order (or next order) formulation of α_s is used. When a value of Λ is extracted from experimental data one has to give the formalism within which it is obtained. Furthermore, the relative importance of second and next order contributions may be different for different processes. This leads to an arbitrariness in the definition of Λ extracted from the data for different processes.

1.4.1 Application to deep-inelastic scattering

We have seen that the coupling constant becomes small for large Q^2 (i.e. small distances), and in this regime the perturbation expansion may give reasonable convergence.

Most of the QPM picture is restored in perturbative QCD, however, a breaking of scaling is predicted. The structure functions are expected to depend on Q^2 in addition to the x-dependence. The Q^2-dependence is introduced by the mechanism of gluon bremsstrahlung (fig.8).

At a given Q^2, say Q_0^2, the theory is incapable of predicting the shape of the structure function. This shape is a consequence of the non-perturbative aspects of the theory, which are not (yet) calculable.

However, given the structure function at Q_0^2, the theory is able to predict the variation with Q^2. The Altarelli-Parisi equation [37] relates the structure functions at different Q^2:

$$Q^2\cdot\frac{dq(x,Q^2)}{dQ^2} = \frac{\alpha_s(Q^2)}{2\pi}\cdot\int_x^1\frac{dy}{y}\cdot q(y,Q^2)\cdot P_{qq}(x/y) \qquad (38)$$

This form of the equation is valid in the leading order approximation for a non-singlet structure function $q(x,Q^2)$. Non-singlet functions are those that do not contain quark-antiquark pairs (flavour-singlets), like xF_3.

The integrand contains the splitting distribution function which describes the splitting of a quark into a quark and a gluon; this particular $P_{qq}(z)$ describes the probability of finding a quark in a quark at a value of z, the fraction of the original momentum fraction x. The distribution function has the form:

$$P_{qq}(z) = \frac{3}{4}\cdot\left[\frac{1+z^2}{(1-z)_+} + \frac{3}{2}\cdot\delta(z-1)\right]$$

with the Dirac δ-function and in which the formal definition of the distribution function $(1-z)_+$ is given by the requirement that the integral equation

$$\int_0^1 dz \frac{g(z)}{(1-z)_+} = \int_0^1 dz \frac{g(z) - g(1)}{(1-z)}$$

is valid for all functions g(z). After substitution of the function P_{qq} the evolution equation for xF_3 is given by:

$$Q^2\cdot\frac{dxF_3(x,Q^2)}{dQ^2} = \frac{\alpha_s(Q^2)}{3\pi}\cdot\left[\{3 + 4\log(1-x)\}\cdot xF_3(x,Q^2) + \right.$$

$$\left. \int_x^1 dy \left(\frac{2}{1-y}\right)\cdot\{(1+y^2)\cdot\left(\frac{x}{y}\right)\cdot F_3\left(\frac{x}{y},Q^2\right) - 2xF_3(x,Q^2)\}\right]$$

where

$$B = \frac{33-2f}{12\pi}$$

and where $\alpha_s(Q^2)$ is used as defined above. The corresponding evolution equations for functions containing quark-antiquark pairs, contain also gluon distributions, and will not be given here (they can be found in e.g. [37]).

This rather complicated form of the predictions can be tested experimentally in different ways. Some of these methods will be given in the following. Tests of QCD are limited to the evolution of the structure functions with Q^2. The x-dependence of the structure functions at fixed Q^2 is not predicted by the theory.

1.4.2 The moment method

Because the integro-differential equation (38) cannot be solved analytically, one approach is to define moments: The n^{th} moment of $q(x,Q^2)$ is

$$M(Q^2,n) \equiv \int_0^1 x^{n-1}\cdot q(x,Q^2)dx \qquad (39)$$

The evolution equations can be solved in terms of the moments, which yields a possibility of experimental verification of these equations.

The basic problem of the analysis using moments is that a measurement over the full x-range for all Q^2 is required. This is clearly not satisfied due to the kinematical limits of the various experiments. The analysis needs in those regions a filling procedure with guesses, obtained in other regions. This introduces an arbitrariness, which is difficult to control.

More theoretical problems are:

The choice between the x-scaling variable or ξ-scaling variable, as introduced by Nachtmann [35].

The question whether data from the resonance region have to be included.

Due to these experimental and theoretical problems we have not attempted an analysis using moments.

1.4.3 Explicit functional form for $q(x,Q^2)$

This method proposed by Buras and Gaemers [22] is based on an explicit parametrization of the structure functions, which satisfies the moment equations. Because QCD does not predict the x-dependence, a functional form is used, which gives empirically a reasonable description of the experimental data. Once the x-dependence is given at a fixed Q^2, the Q^2-dependence is imposed by QCD depending on the value of Λ, the free parameter of the theory. The parametrization is based on the leading order formalism, with the definition of α_s of equation (36).

The valence and sea-quarks are parametrized separately in the model of Buras and Gaemers. The structure function xF_3 is closely related to the valence-quark momentum distribution function (see equation (19) and (24)), the difference being proportional to the difference of the strange and charmed sea. For the valence-quark momentum distribution function the parametrization of Buras and Gaemers is:

$$x \cdot q_{valence}(x,Q^2) = \frac{3}{\beta(\eta_1,\eta_2+1)} \cdot x^{\eta_1} \cdot (1-x)^{\eta_2}$$

where

$$\eta_1 = \eta_{01} + \eta_{11} \cdot s \cdot 4/25$$

$$\eta_2 = \eta_{02} + \eta_{12} \cdot s \cdot 4/25$$

and

$$s = \log\left[\frac{\log(Q^2/\Lambda^2)}{\log(Q_0^2/\Lambda^2)} \right]$$

where Q_0^2 is a fixed value of Q^2. The Euler β-function ensures:

$$\int_0^1 F_3 dx = 3$$

The values of Λ, η_{01} and η_{02} are free parameters in this model of the valence structure function. The evolution equation fixes the values of η_{11} and η_{12} for a given set (η_{01},η_{02}) independent of Λ. The values of η_{11} and η_{12} are found fitting the first twelve moments (equation (39)) given by the parametrization to the behaviour predicted by the solution of the evolution equation in terms of the moments:

$$M(Q^2,n) = M(Q_0^2,n) \cdot \exp(-s \cdot \gamma^n)$$

where γ^n is an analytical function of n [22]. A parametrization of the sea is necessary to obtain F_2. The structure functions of the sea are split into contributions of the u, d, s, and c quarks. The sea contributions are parametrized in terms of the normalizations a(s) and the exponents b(s):

$$x \cdot q_{sea}(x,s) = a(s) \cdot (1-x)^{b(s)}$$

for u, d, s, and c and similarly for the gluon distribution. The latter distribution is necessary in order to be able to solve the evolution equations for these singlet contributions. The up and down sea are assumed to be identical. The evolution of the sea structure functions can be determined from their first two moments. A detailed prescription is given in [22] and [23]. At Q_0^2 the various sea contributions are assumed to have the same x-dependence, i.e.

$$b(s=0) = \eta_s$$

where η_s is a free parameter in the model. Additional free parameters to fix the normalization of the sea are the ratio of the antiquarks to the total quark contribution at $Q^2 = Q_0^2$:

$$\bar{q}/(q+\bar{q})$$

and the ratio of the strange sea to the up sea, also defined at Q_0^2:

$$\bar{s}/\bar{u}$$

The normalization of the charmed sea follows from the assumption:

$$c = 0 \quad \text{for} \quad Q^2 < 1.8\ \text{GeV}^2$$

The gluon normalization follows from momentum conservation. The part of the cross-section which is related to charm production is parametrized according to equation (35) in section 1.3.12 ("soft rescaling"). With these parametrizations and the QPM formulations of the structure functions given in section 1.3.7 the model can be constructed.

The advantage of this approach is that only a part of the full x-range is needed, and hence regions where large experimental or theoretical uncertainties dominate can be excluded. The main disadvantage is the arbitrariness of the functional form, which is not at all imposed by QCD. However, this parametrization is useful as a phenomenological description of the data.

1.4.4 Non-perturbative effects

At present energies non-perturbative effects may be large. Coherent phenomena such as transverse momentum effects, resonance production, diquark scattering, and elastic scattering result in $1/Q^2$ and $1/Q^4$ etc. corrections to the perturbative QCD predictions. These effects are referred to as "higher-twist effects".

These effects introduce scaling violations, which are difficult to separate from the log Q^2-dependence of the simple QCD predictions. No calculations of these effects exist yet. The parametrization of higher-twist effects commonly introduced is [38]:

$$f(x,Q^2) \rightarrow f(x,Q^2)\cdot\left[\,1 + \frac{\mu_1^2}{Q^2(1-x)} + \frac{\mu_2^4}{Q^4(1-x^2)}\,\right]$$

where μ_1 and μ_2 are free parameters. The inclusion of these terms in the analysis decreases the amount of violation of scaling attributed to perturbative QCD, and hence the estimate of Λ will decrease. This parametrization is arbitrary to a large extent, it only reflects the prejudice that these non-perturbative effects die out with increasing Q^2 as powers of Q^2, and that they are more important for large x than for small x.

Chapter 2

THE NEUTRINO BEAM

2.1 INTRODUCTION

Basically two types of neutrino beams are used for the study of neutrino interactions:

1. Wide-band beams, where the maximum possible number of secondary particles are focused. These kinds of beams provide high event rates. However, the spectrum peaks at low energies and is not well known. Furthermore, the high-energy part of the spectrum is not very pure as far as the polarity of the particles is concerned.

2. Narrow-band beams, where particles in a small momentum-bite are focused. The event rates in these beams are one to two orders of magnitude lower than in wide-band beams. In return a well defined spectrum is obtained, with an energy-angle correlation. The beam can provide a hard spectrum with good purity.

The experiment was performed at the narrow-band neutrino beam of the CERN SPS. This beam will be described in the following sections.

2.2 THE CERN NARROW-BAND BEAM

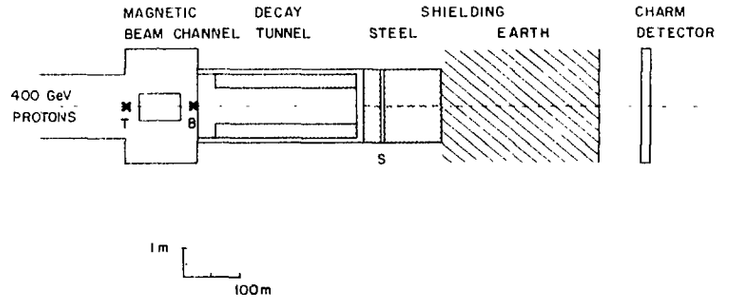

Figure 9: A schematic layout of the NBB. Marked are: (T) the position of the production target; (B) the position of the beam current transformers in the secondary beam; (S) the solid-state counters in the shield (see text).

Schematically the components of the CERN narrow-band beam (NBB) can be summarized as follows (see fig.9):

1. A target region where secondary hadrons are produced by the proton beam from the SPS.

2. A magnetic beam forming channel of 120 m length.

3. A 300 m long decay tunnel, required in order to produce neutrinos by the decay of hadrons.

4. A shield composed of iron, earth and rock, to absorb the hadrons and range out the muons in order to obtain a nearly pure neutrino beam.

2.2.1 Layout of the CERN NBB

The beam is designed to meet the demands of large acceptance and high purity [39].

The proton target consists of a string of five beryllium rods of 100 mm length. Each rod is inserted with both ends into holes of a beryllium plate. The target box contains three different targets, with diameters of 10 mm, 3 mm and 2 mm. The 3 mm target was used during data-taking. The proton beam is extracted from the SPS at 400 GeV.

During NBB operation the fast extraction is used yielding spills of 23 μs length. Depending on proton beam intensity and secondary beam polarity the proton beam is extracted in one to five spills. The time between spills is 23 μs. The choice of number of spills is a compromise between minimal dead-time of the experiment and minimal cosmic background. The time-structure of the burst is visible in fig.10, were the event time distribution of neutrino interactions (after selection) is shown for one SPS operation period (a few weeks).

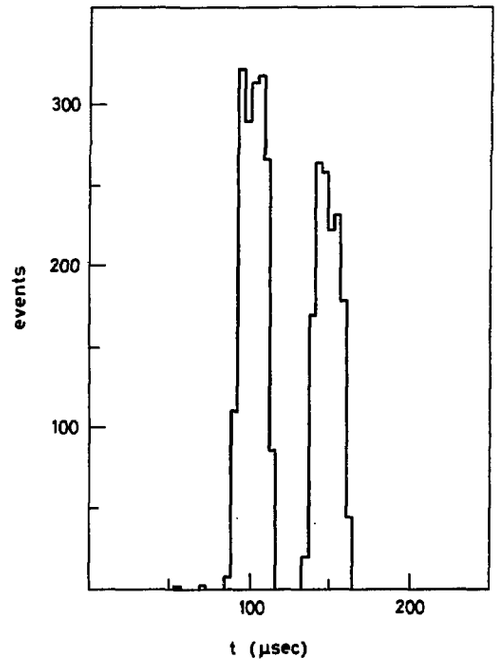

Figure 10: The time distribution of events recognized as neutrino interactions in the CHARM detector recorded during one SPS operation period. The origin of the time axis is the start of the gate during which triggers are accepted in the neutrino detector. The time-difference between the start of the trigger gate and the accelerator burst is kept constant.

The magnetic channel focuses charged secondary particles of one polarity. The beam line was used at a central momentum of 200 GeV/c. The channel transports particles with a maximum $\delta p/p$ of ±10%, resulting in an r.m.s. momentum spread of 4.5% $\delta p/p$. The central momentum is known with an accuracy of 1.0 % to 1.5%.

Particles produced within a forward cone of approximately 10 μsterrad are transmitted through the beam line. The secondary beam is nearly parallel when it enters the decay tunnel. Its angular divergence is ±0.22 mrad in both planes. In the design of the beam line a compromise is chosen between maximum neutrino event rate and optical properties. The beam is not parallel in the decay tunnel due to the size of the production target and optical aberrations, which are a consequence of the momentum acceptance of the magnetic channel.

The decay tunnel is evacuated, and has a pressure of 1 torr. The tunnel is followed by a shield consisting of a 180 m long iron cylinder with a diameter of 2.5 m. The end of the system is formed by a 230 m long earth shield.

Neutrinos are produced by the decay of pions and kaons. The channel is designed in such a way that mainly decays of particles in the decay tunnel contribute to the neutrino flux at the position of the experimental detectors.

The proton beam and the target are on an axis which makes an angle of 11 mrad with respect to the final beam direction in the decay tunnel. Furthermore, the bendings of the beam in the magnetic channel are performed in two planes. With this technique one has achieved that the secondary beam does not point towards the experiment until the last bend before it enters the decay tunnel. Thus the background of neutrinos from decays of hadrons before the decay tunnel is reduced. This feature enables one to calculate the energy spectrum and the spatial properties of the neutrino beam accurately.

2.2.2 Monitoring system of the CERN NBB

The intensity and position of the extracted proton beam, secondary beam and of the muons in the shield is monitored by a system of detectors [40,41].

There is quite some redundancy in the information provided by this detector system. This fact enables us to make various checks on the performance of the monitors.

The detectors, which were used during the data-taking and the analysis, can be summarized as follows:

Detectors around the target in the primary proton beam

A beam current transformer (BCT) is placed in the proton beam to measure its intensity. Just in front of the target a system of secondary emission foils is mounted consisting of an intensity monitor (SEM), two pairs of split foils to monitor the horizontal and vertical asymmetry and two foils with holes of different diameter in order to measure the width of the beam. This system is mainly used for on-line purposes to provide a check on the quality of the steering of the proton beam.

The multiplicity is measured with a foil mounted downstream from the target. The positions of these monitors are shown in fig.11.

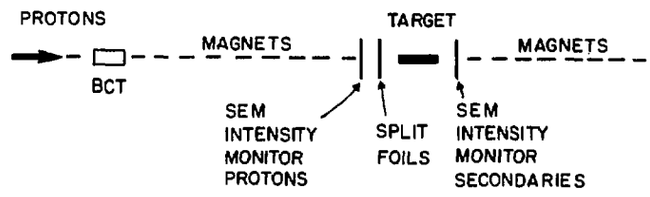

Figure 11: Detectors around the target in the primary proton beam.

Secondary hadron beam monitors

A threshold Cerenkov counter mounted behind the momentum defining collimators records the time structure of the secondary beam. The signal of this counter is used to measure the effective dead-time of the neutrino detector.

Two beam current transformers (BCT) are used for the intensity measurement. They have an inner hole diameter of 20 cm and 10 cm respectively. The BCTs are placed just in front of the entrance of the decay tunnel. The BCT with the large hole diameter is used in the analysis to determine the absolute particle fluxes.

The current induced in the BCT is integrated over a gate time fully covering the extraction spill time. Four time samples of this integrated current are taken (fig.12) at times T_a, T_b, T_c, and T_d such that

$$2\cdot(T_b - T_a) = T_c - T_b = 2\cdot(T_d - T_c)$$

The machine burst occurs between T_b and T_c.

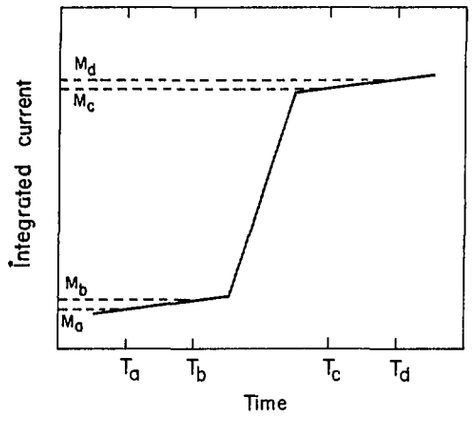

Figure 12: Integrated current in the BCT. The accelerator burst occurs between T_b and T_c.

In order to correct for offset currents an analogue circuit calculates the corrected measurement M from the four time samples M_{a-d} using the relation

$$M = M_a - 2M_b + 2M_c - M_d$$

All five signals M, M_{a-d} are digitized by ADCs. The result M is calibrated with a current pulse of the same time structure as the extracted beam. An accuracy of 3% can be obtained in the absolute calibration of this device.

In the same region a differential Cerenkov counter is used to determine the relative abundance of the different particle types. This is done by recording the current of this counter integrated during a machine burst for different gas pressures.

The profiles of the hadron beam are measured in front of and behind the decay tunnel. Depending on the intensity of the beam a system of either secondary emission foils or ionization chambers is used. These measurements are used during data-taking only to monitor the quality of the secondary hadron beam. Due to the bad background conditions these monitors provide only a rough measurement of the width of the beam. The positions of the monitors in the secondary beam are shown in fig.13.

Muon counters in the shield

The muon flux in the shield is measured in various air gaps in the iron [41]. In six gaps in the shielding silicon solid-state detectors are placed, at iron depths between 10 m and 120 m.

The detectors are mounted on a support structure, which is movable to provide the possibility of an alignment with respect to the beam. On each support seven counters are mounted along a horizontal radius, 15 cm apart. The first counter is positioned on the beam axis, the last one at a radius of

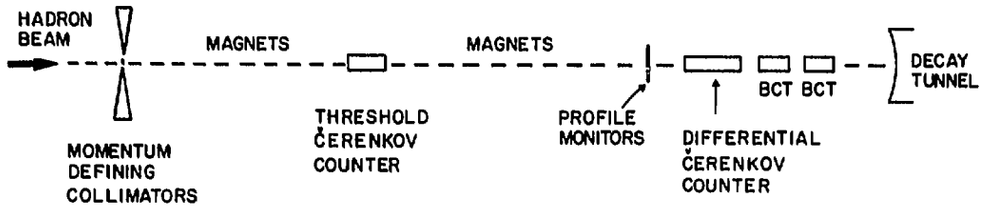

Figure 13: Monitors in the secondary hadron beam.

90 cm. In addition, a few circles with radii of multiples of 15 cm are equipped with eight detectors. Depending on the gap one or more of those circles of detectors are operational.

A movable box containing a stack of five counters is used to fix a relative calibration of the counters within one gap. This box can also be used to provide a more detailed mapping of the muon flux. One additional box travels between the gaps and serves to fix the calibration from gap to gap.

Different detector types are used at different places, according to the large variation in flux-density at different iron depths and radii. The surface varies from 30 mm^2 to 200 mm^2 and the thickness from 100 µm to 1000 µm.

To obtain the detector signals, charge integration is used, with a correction for the leakage current of the detector. The necessary leakage current correction is measured between machine bursts and is updated every 15 minutes.

The signal obtained with the muon detectors is a result of the ionization in the sensitive volume caused by the muons and by secondary radiation produced by the muons in the shield. This background contribution is as large as 20% in some cases. The secondary radiation has a broader spatial structure than the muons and causes a position dependent calibration of the detectors. A detector calibrated at a certain position in the shielding needs to be recalibrated if it is used at a different radius from the beam axis in the same gap, or if it is used in a different gap.

The background is a severe problem for the absolute measurement of muon fluxes. However, the relative calibration of counters within one ring is not changed by this background. The relative calibration of these detectors within a ring of eight is known with an accuracy better than 1%.

For the measurement of the shape of the muon flux a correction has to be applied for this background. The correction is measured using emulsion techniques or alternatively by the use of different absorbers in front of the detectors. An absolute calibration of these counters is difficult.

Therefore, these detectors were only used as relative monitors, providing a relative normalization of the positive beam with respect to the negative beam. The system is also used to provide a relative normalization for periods, during which the BCT-information was unreliable or not available.

2.3 PROPERTIES OF THE NBB

2.3.1 Narrow-band nature

The energy-spectrum of the NBB has two components, one corresponds to pion decays and another to kaon decays.

At the position of the experiment the energy of the neutrinos is correlated with the radial distance from the beam axis. This property of the NBB is a result of the small momentum spread and the small divergence of the secondary hadron beam, together with the neutrino production, which occurs predominantly by the two-body reactions $\pi \rightarrow \mu\nu$ and $K \rightarrow \mu\nu$. The two component structure causes an ambiguity in the energy-radius correlation.

2.3.2 The hadron beam

In order to be able to calculate the neutrino energy spectrum one must have detailed knowledge of the properties of the secondary hadron beam.

The calculation of these properties necessarily starts with a description of the production of particles by the proton beam. Absolute cross-sections as a function of secondary momentum and production angle have been measured in a beam in the North Area (NA) of the CERN SPS [42]. These measurements were performed in a low intensity beam where the secondary particles were counted and recognized individually.

Also the beam acceptance as a function of momentum and production angle has to be known. The acceptance was obtained by a simulation of the magnetic components in the beam, taking into account apertures of the magnets, collimators, and the absorption due to the material in the beam. The calculations were performed using the beam simulation program TURTLE [43].

From the production data and the acceptance, the relative abundance of different particle types can be computed, and of course corrections for the decay of pions and kaons have to be made. These particle ratios are directly measurable in the NBB itself. As mentioned already, for this purpose a specially designed Cerenkov counter is placed in the straight section between the last bending magnet and the entrance of the decay tunnel [44]. Due to the high intensity and short spill length individual particle identification is impossible. The integrated current of this counter is measured at different pressures of the gas in the counter. The surface under the different peaks attributed in the pressure-curve to pions, kaons and protons is integrated, thus providing a relative measurement of the particle abundances.

The direct measurement of the particle ratios can be compared with the calculation based on the production measurements. Both results are given in table 3. The uncertainty in the results of the NA measurements is 3%.

TABLE 3
Particle ratios in the NBB.

	NBB-measurements	Parametrization of NA-measurements
K^-/π^-	0.049 ± 0.0015	0.050
K^+/π^+	0.147 ± 0.0044	0.149
p/π^+	4.4 ± 0.2	4.05

The results for the kaon to pion ratio agree, but the proton to pion ratio is 10% higher in the direct measurement compared to the calculation. This can be explaned by a small difference in momentum-calibration of the beam line used in the production cross-section measurement relative to the NBB momentum setting, as a change of 1% in the central momentum of the beamline causes a change of 3.5% in the p/π ratio in the same direction, according to calculations based on the parametrization of the production spectra measured in the North Area of the CERN SPS.

In order to avoid problems of this kind the result of the direct measurement is used throughout the analysis.

However, more detailed information than the relative particle fluxes are needed for the computation of the neutrino spectrum. A full description of the phase-space density of the beam in the decay tunnel is necessary. This can be seen in fig.14, where some correlations are shown in the angle and momentum variables. These correlations are obtained with the above méntioned beam simulation program.

For this calculation the particle production spectra and angular distributions and the positions, sizes, apertures, and magnetic fields of the mag-

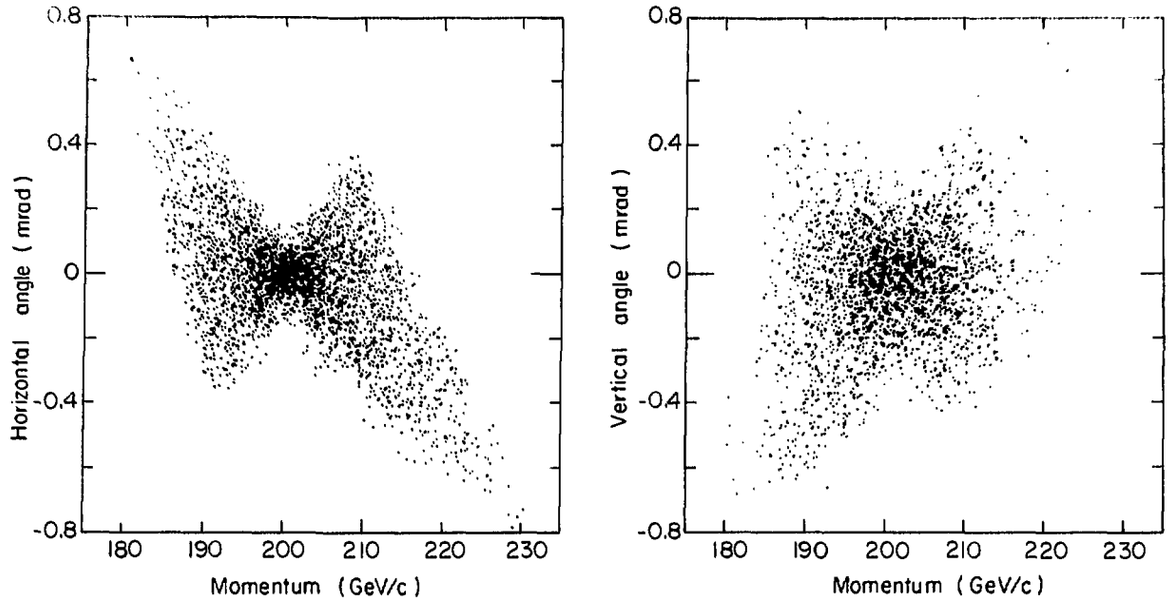

Figure 14: Simulated phase-space densities for particles in the NBB. The angular distribution of particles entering the decay tunnel is shown for both projections as a function of the particle momentum.

nets in the beamline have to be known. The program simulates trajectories of individual particles through the beamline. Apart from a small contribution of earlier decays (see a following section), only decays of parents in the straight section of the beamline behind the last bending magnet (including the decay tunnel) contribute to the neutrino flux at the position of the neutrino detector. The neutrino spectrum incident on the neutrino detector follows then from the phase-space density of the parents entering the decay region and the decay kinematics, which will be described in the following section.

2.3.3 Narrow-band energy-spectrum

Kinematics

The energy E of a neutrino produced by the decay of a parent particle with velocity v, when measured in the lab system is given by the Lorentz transformation:

$$E = \gamma \cdot E^{cm} \cdot (\beta \cos\theta^{cm} + 1) \qquad (40)$$

where

β = v/c, c being the velocity of light.
γ = $1 / \sqrt{(1-\beta^2)}$
E^{cm} = neutrino energy in the rest system of the parent.
θ^{cm} = decay angle of the neutrino with respect to the parent particle momentum in the rest system.

Consider a two body decay into a muon with mass m and a massless neutrino then E^{cm} is fixed and can be written as

$$E^{cm} = (M_p^2 - m^2) / 2M_p \qquad (41)$$

where M_p is the parent mass. For spinless particles the decay is isotropic in the rest system, and hence flat in $\cos\theta^{cm}$. For a monochromatic beam with a high-energy (where we can put $\beta = 1$) the energy-spectrum will then be flat from E = 0 up to the maximum energy

$$E_{max} = 2 \cdot \gamma \cdot E^{cm}$$

Putting $\gamma = E_p/M_p$, where E_p is the energy of the parent, we get

$$E_{max} = E_p(1 - m^2/M_p^2)$$

Numerically, for a 200 GeV parent beam the maximum energy is

$E_{max}(K) = 191$ GeV for kaon decays and
$E_{max}(\pi) = 85$ GeV for pion decays.

Due to the limited radial dimension of the neutrino detector, the effective spectrum for the experiment has a cut-off at the lower part of the spectrum (see fig.15).

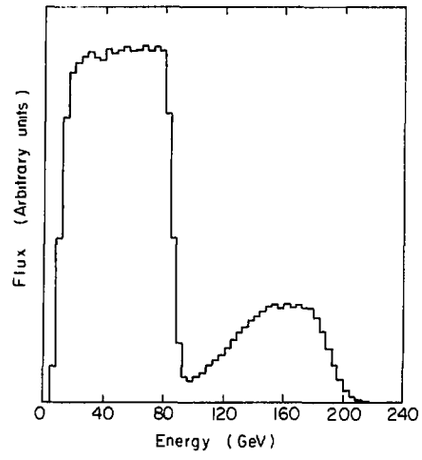

Figure 15: The energy spectrum of the neutrino beam calculated for this experiment. Only neutrinos within a radius of 120 cm were accepted. The low-energy part corresponds to pion decays, the high-energy part to kaon decays. Due to the limited radial acceptance of the detector, the two components do not extend to zero energy. The cut-off at the high-energy side of the two components is not sharp due to the momentum spread in the hadron beam.

For the muon energy-spectrum of this monochromatic beam this will yield a flat behaviour from a minimum energy depending on the mass of the parent up to 200 GeV. The minimum muon energies are then 9 GeV for kaon decays and 115 GeV for pion decays.

As a direct consequence of equations (40) and (41) the neutrino energy E is fixed by the knowledge of the decay angle for a given parent particle decay in a monochromatic beam. This decay angle is given in the experimental set-up by the radial distance from the beam axis at which an event was measured.

Energy radius correlation

The largest fraction of decays of pions and kaons is into a muon and a neutrino. This percentage is nearly 100% for pions and 63.5% for kaons. This fact together with the small momentum spread and the small divergence of the secondary hadron beam yields a two-band structure in the energy-radius plane as seen by the experiment.

However, the fixed energy-radius relation is smeared out by the following experimental conditions:

1. The hadron beam is not strictly monochromatic but has a certain momentum spread.

2. The hadron beam is not parallel but has a small divergence.

3. The decays do not occur at a fixed point but along the full length of the decay tunnel.

The effect of the length of the decay tunnel is mostly visible at large radii, where the parallax is the largest. At medium radii, where the variation of the energy with radius is largest, the influence of the divergence is seen. The momentum spread smears the distribution equally at all radii and dominates near the beam axis.

Depending on which energy-radius band an event belongs the energy resolution of the kaon part of the spectrum is ≈5% near the beam axis and ≈15% at ca. 1 m radius; for the pion part this amounts to 5% and 30% respectively. The resolution in neutrino energy as a function of the radius is shown in fig.16.

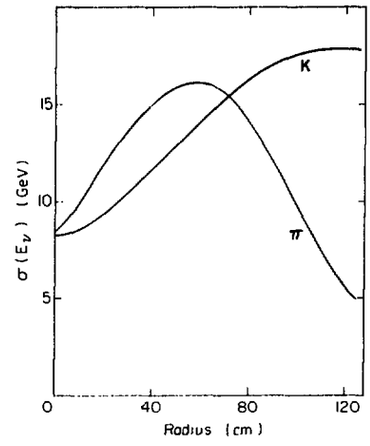

Figure 16: Neutrino energy resolution as function of the radius in the neutrino detector.

2.3.4 Other components

The two components of the NBB as described above provide the majority of the neutrino events obtained in the detector. However, also other components contribute to the flux. These other components are due to:

1. other decay modes of the kaon;

2. wide-band background;

3. decay of muons.

The energy-radius correlation as it was measured in this experiment is shown in fig.17.

Other kaon decay modes

The two body decay of the kaon into a muon and a neutrino contributes 63.5% of all kaon decays. The next largest contribution to the neutrino flux is formed by the decay $K \rightarrow \mu\nu\pi^0$. In table 4 a list of decay modes [45] contributing to this background is given in more detail. In this table the decay branching ratios (B.R.) and the appoximate event rates (flux weighted with neutrino energy) are given for the various components relative to the pion two-body decay contribution. The decay $K \rightarrow e\nu_e\pi^0$ gives rise to electron-neutrinos the interactions of which are classified in the neutrino detector as neutral-current events.

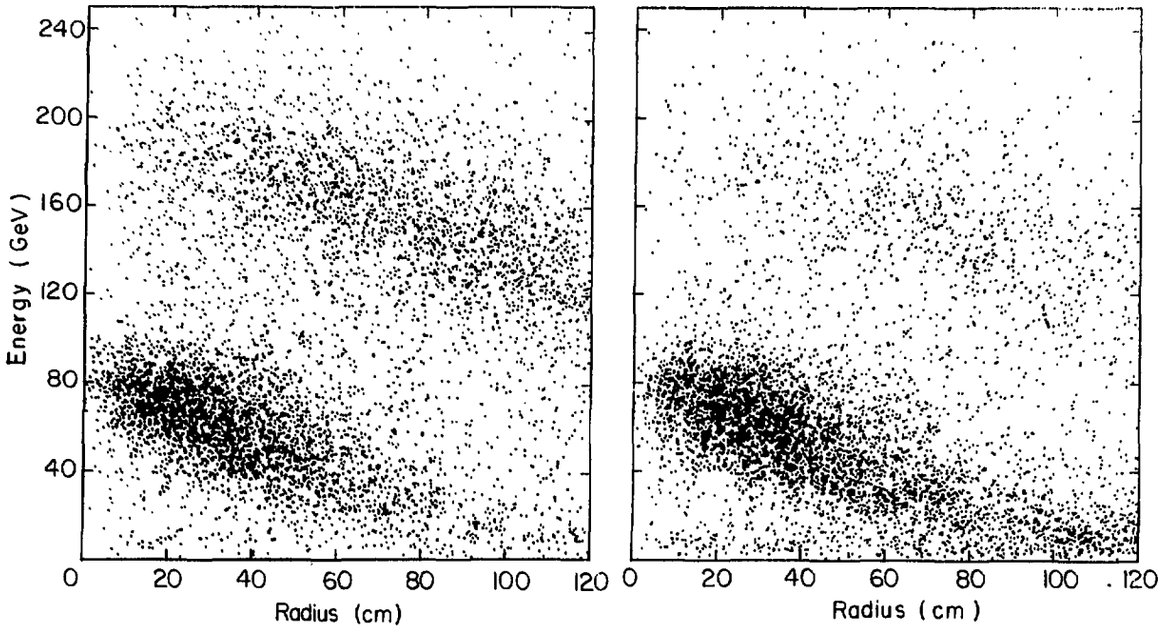

Figure 17: Measured energy-radius correlation of charged-current events for (a) the neutrino beam and (b) the antineutrino beam. The high-energy band corresponds to kaon decays, the low-energy band to pion decays. The different K/π ratios are clearly visible from the different populations of the two bands in the two beams. The events between the two bands are partly due to the limited precision of the energy measurement in the neutrino detector and partly due to neutrinos from the decay $K \to \mu\nu\pi^0$. The component of wide-band background is visible predominantly at low neutrino energies (< 30 GeV) in the antineutrino exposure. This background is relatively more important at large radii.

TABLE 4
Contributions to the muon-neutrino event rate.

Decay	B.R.	ν (R<120)	$\bar{\nu}$ (R<120)	$\bar{\nu}$ (R<90)
$\pi \to \mu\nu$	0.9997	1.0	1.0	1.0
$K \to \mu\nu$	0.6350	0.876	0.292	0.220
$K \to \mu\nu\pi^0$	0.0320	0.022	0.007	0.006
$K \to \pi\pi^0$	0.2116	0.0013	0.0004	0.0003
$K \to \pi\pi\pi$	0.0559	0.0012	0.0006	0.0004
$K \to \pi\pi^0\pi^0$	0.0173	0.0001	0.00003	0.00003
$K \to \mu\nu\gamma$	0.0058	0.0045	0.0015	0.0012

Wide-band background
This is the name for the collection of neutrinos which is produced by decays before the momentum selection of the secondary beam. This background can be studied by running the beam with the momentum defining collimators closed. Its contribution to the flux is ≃2% for a neutrino beam and ≃10% for an anti-neutrino beam.

Decay of muons
The contribution of the decay of muons into two neutrinos and an electron to the total neutrino flux is very small (< 2.10^{-3}). This is estimated simulating the trajectories of muons in the decay tunnel, the shielding, and the surrounding material.

2.3.5 Muon flux

The measurements of the muon flux in the shield can be compared with a calculation based on the simulation of the muon trajectories. As a starting point the simulation of the secondary hadron beam is used.

The muon momentum vector is derived from the decay kinematics and the parent hadron momentum vector. Like for the decay neutrinos, the angular distribution of the muons will be broader for kaon decays than for pion decays. However, the mean momentum of muons from kaon decays is smaller than that of muons from pion decays.

The trajectories of the decay muons are calculated taking the energy-loss and multiple scattering into account. The approximation of small angle scatters is used, which yields the following formulas for the root mean square displacement δx_{rms} and change in projected angle $\delta\theta_{rms}$ [46]:

$$\delta\theta_{rms} = \frac{20\ \text{MeV/c}}{p\beta} \cdot \sqrt{\lambda} \cdot (1 + 1/9 \cdot {}^{10}\log\lambda)$$

$$\delta x_{rms} = 1/\sqrt{3} \cdot L \cdot \theta_{rms}$$

where

λ = the thickness in radiation length.
L = the traversed length.
p = muon momentum.
β = velocity in terms of the velocity of light.

The track is followed in steps of five radiation lengths. The displacements are taken to be normally distributed.

A comparison of the calculated distribution of muons in the second gap in the shielding (after 30 m of iron) is made with a measurement [47] obtained with the solid-state detectors (fig.18).

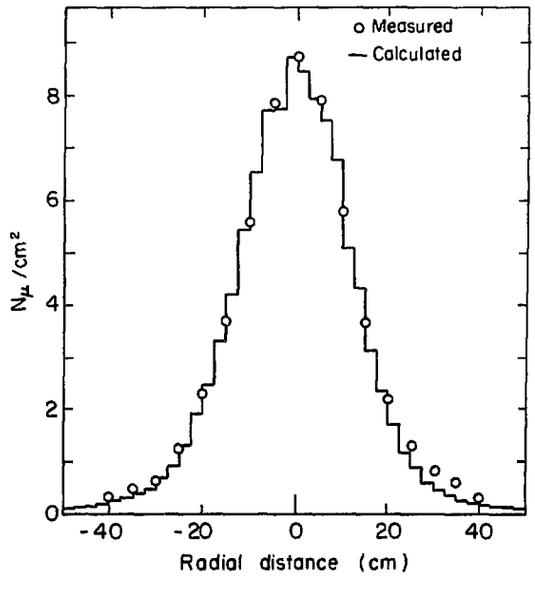

Figure 18: Comparison of the calculated radial distribution of muons in gap II with the measurement (arbitrary units).

This particular gap was chosen because the measurements are here less affected by secondary radiation than in gap 1, while the flux is still considerable. The agreement of the calculation and the measurements is satisfactory.

Although the counting rates of the individual counters depend on the beam steering, the combination of counting rates of a suitably chosen set of counters can be shown to cancel the individual variations to a large extent. The simulation can be used to predict the sensitivity of different counters or combination of counters to small mis-steerings of the hadron beam. The calculation of the sums over the rings is made under the assumption of perfect relative calibration of the counters. According to the calculations, the influence of a 1 cm mis-steering of the secondary beam on the sum of the counting rates of eight counters on a 15 cm ring is 0.1% in the second gap, after 30 m of iron, and 0.2% in the first gap, after 10 m of iron. The main contribution to a change of the detection efficiency when the beam is mis-steered is due to small relative calibration errors of the individual counters. The relative calibration of the solid-state counters on one ring is known to better than 1%, thus the effect of variations in the beam steering on the total muon detection efficiency is smaller than 0.5%.

2.3.6 Beam performance

The operation and stability of the beam can be checked at several points with the monitoring system. As a result of the redundancy in the monitoring system, also a few cross checks of the individual counters are possible. In this way malfunctioning of monitors can be separated from instabilities of the beam. A large mis-steering of the secondary hadron beam may cause the following problems:

- unreliable operation of the beam monitors;
- a shift of the energy-radius relation, which causes a wrong neutrino-energy assignment.

A large mis-steering may indicate more serious problems, it may be the result of the following causes:

- switching-off of a magnet, which may change the focusing in an unknown way;
- a mis-steering of the proton beam, which may give an effective shift in the average momentum and a larger divergence of the secondary beam.

A continuous record of the beam steering is kept, in order to be able to discard data taken under bad conditions.

Measurement of beam position

From the measurements of the muon flux in the shielding an estimation of the hadron beam direction can be obtained. In each gap the centre of the muon flux is obtained from the central detector in combination with eight counters on a ring.

This system contains four axes on which the beam is assumed to have a gaussian intensity profile. The centres on the four axes, defined by the maximum of the beam profile on the axis, define the centre of the flux distribution on the plane. In fact only two axes are needed, and therefore a consistency check can be made on the results of the method. In fig.19 some comparisons are shown.

In this way, the beam centres can be calculated with a precision of ±1 mm in each projection. With this method we find a stability of the beam steering of a few millimeters r.m.s. for typical running conditions.

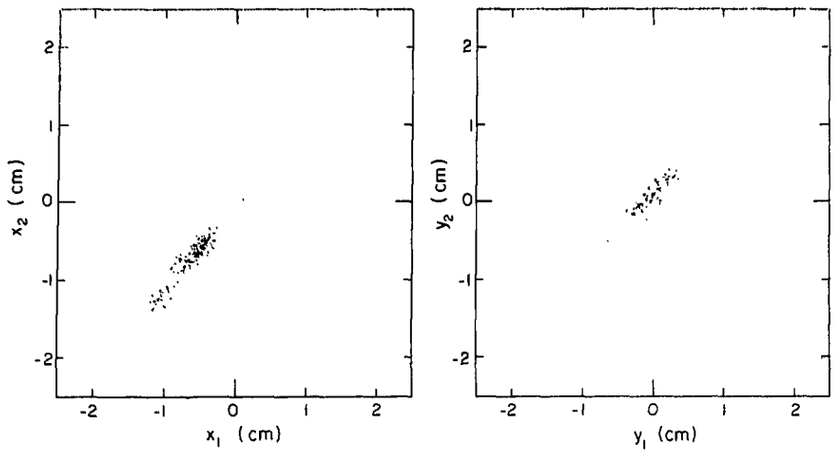

Figure 19: Comparison of two independent measurements of (a) the horizontal beam position, x_i, and (b) the vertical beam position, y_i, in gap II. The calculations are made for individual accelerator bursts.

Chapter 3

THE EXPERIMENTAL SET-UP

3.1 THE DETECTOR

The CHARM detector [48] was built for the study of neutrino interactions produced by the neutrino beams of the CERN 400 GeV Super Proton Synchrotron (SPS). It was principally designed to investigate the neutral-current interaction

$$\nu + N \rightarrow \nu + \text{anything}.$$

A good muon detection efficiency enables one to separate this interaction from the charged-current process

$$\nu + N \rightarrow \mu + \text{anything}.$$

The detector is equipped with a muon spectrometer and is well suited to the measurement of charged-current interactions.

The main design aims were the following:

1. A large target mass to provide a sufficiently large event rate.

2. Measurement of the energy, and of the energy-flow of showers produced in neutrino interactions. The energy-flow measurement requires that the hadronic and electromagnetic parts of showers are approximately equally long in the calorimeter.

3. Identification of muons for the classification of events as neutral or charged-current interactions.

4. Sign and momentum-analysis of muons produced in charged-current interactions.

3.1.1 The target calorimeter

The detector consists of a fine-grain target calorimeter, surrounded by a frame of magnetized iron and followed by a forward muon spectrometer (fig.20).

Marble[1] is used as target material to provide a large mass and to meet the requirement of the energy-flow measurement. The iron, surrounding the marble calorimeter, is used for muon identification, and sign and momentum-analysis, while it also serves as a calorimeter for full containment of showers starting in the marble calorimeter.

The target calorimeter with its iron frame is composed of 78 equal subunits. The subunits consist of an iron frame, 45 cm wide, surrounding a marble plate, with 3x3 m^2 surface area. The marble plate and the iron frame are 8 cm

---

[1] The physical properties of marble, relevant to the experiment, are equal to those of aluminium. However, marble is 10 times cheaper. It is also a good polarization analyser, used for the measurement of the polarization of positive muons. This aspect of the experiment is not described here.

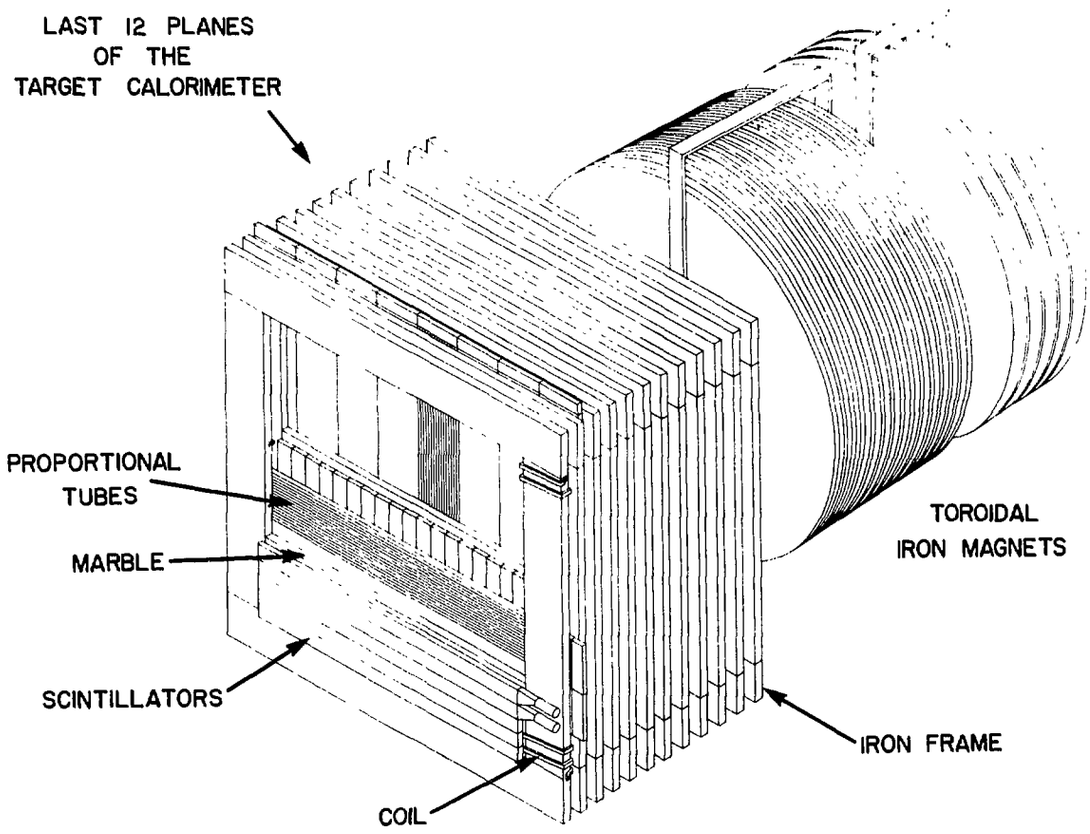

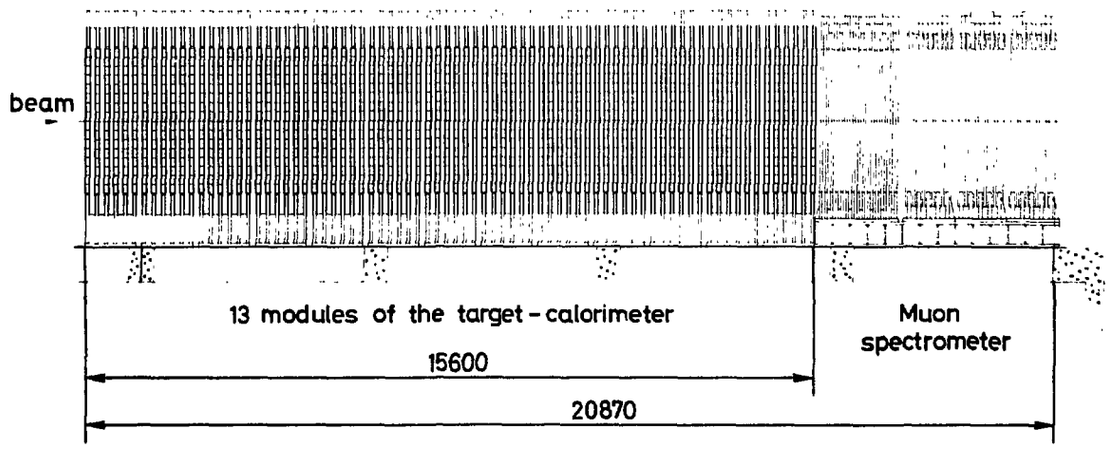

Figure 20: Isometric view of parts of the detector and side view. For explanation see text.

thick. The spacing of the subunits is 20 cm. Groups of six subunits form a module. The iron frames of these six subunits are welded together at the base.

The target plates are interleaved with scintillation counters covering the marble plates and proportional counters covering the full area of 4x4 m^2.

One scintillation counter plane consists of 20 plastic scintillators, 3 m long, 15 cm wide and 3 cm thick. The proportional counter planes consist of 128 tubes, 4 m long, 3x3 cm^2 in cross-section.

Both scintillator counters and proportional tubes alternate in the horizontal and vertical direction, one gap being covered by scintillators and tubes of different orientation.

The frames are magnetized by two copper coils on the vertical legs of each frame. A current of 1000 A in both coils, when acting in the same sense, provides a toroidal field of 1.4 T in the frame.

3.1.2 The end system

The target calorimeter is followed by an end system (fig.21) with a twofold function.

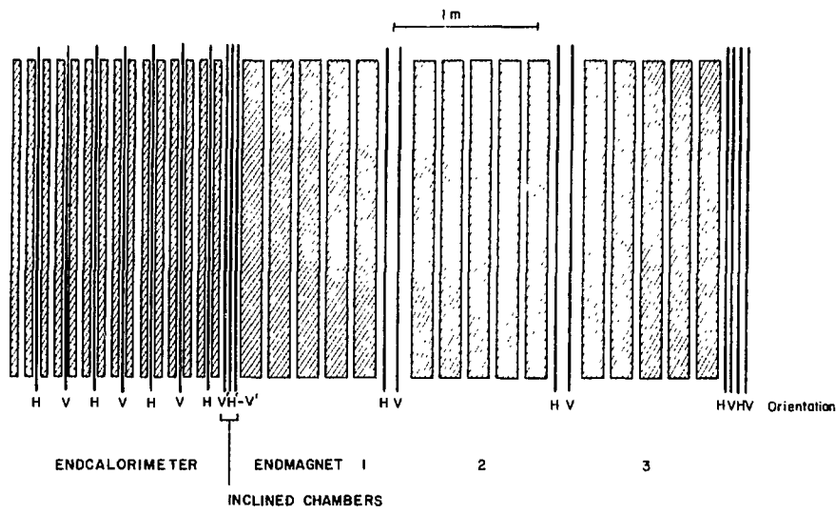

Figure 21: Schematic layout of the end system. The iron discs are shown as shaded rectangles. The orientation of the proportional counter planes (vertical lines) is denoted as H (horizontal wires) and V (vertical wires). The scintillation counter planes are not shown.

The end system serves as muon spectrometer, while the first part is also used for calorimetry.

It consists of iron discs, each 370 cm in diameter. The discs are grouped into four modules, each module giving 75 cm of iron thickness. The discs are magnetized by coils passing through holes in the centre, providing a toroidal field of 1.7 T on average.

The first module, used as end calorimeter, is made out of 15 discs of 5 cm thickness. The three other modules consist of 5 discs of 15 cm thickness each.

Every second gap between the discs in the end calorimeter contains a proportional tube plane, covering an area of 370x370 cm^2. The 16 central tubes are cut into two halves, leaving room for the coils to pass through. The orientations alternate horizontally and vertically. Between the end calorimeter and first end magnet module, three inclined tube planes are placed, rotated 12.5 degrees around the beam axis. One pair of horizontal and vertical tube

planes is placed between the end magnet modules. A double pair of those counter planes terminate the detector behind the last end magnet module.

Six planes of scintillation counters are inserted in the gaps between the iron discs of the end magnet. These counters are used to detect the secondary radiation produced by high-energy muons traversing the iron.

3.1.3 The scintillation counter system

The 3 meter long polyvinyl toluene scintillators (NE114) are terminated on one side by a mirror, and are viewed from the other side by a single photomultiplier (EMI 9839A) through a 50 cm long light-guide. The total mass of scintillator material is 21 tons.

The scintillators provide a good measurement of single particle ionization, a minimum ionizing particles yielding roughly 50 photo-electrons, and a precise measurement of the total energy of hadronic and electromagnetic showers. The good transparancy of the scintillators keeps the variation of the response over the total length of the counter below 30%. The light attenuation of the scintillators deteriorates with time. After three years of operation the yield of photo-electrons of a track traversing the the far end of a scintillator was roughly 20 compared to 50 at the beginning of the scintillator. The attenuation length of each individual scintillator is therefore remeasured monthly.

The signals of the photomultipliers are transported by twisted pair cables [49] to a splitter system. The main part of the signal is fed into the ADC-system via an 80 m long twisted pair cable. This delay enables the trigger logic to generate gating pulses for the ADCs. The trigger logic is fed by the other part of the split signal.

The main signal is divided, 95% being analysed by one 8-bit ADC, 5% by an other 8-bit ADC. This provides the required dynamic range corresponding to 5000 channels.

The ADCs have a buffer storage of 50 events, and are read-out by CAMAC during data-taking.

3.1.4 The proportional drift tubes

The proportional counter planes are formed by 8 chambers each containing 16 extruded aluminium tubes of internal cross-section 29x29 mm^2 [50]. The tubes are 4 m long. A stainless-steel sense wire, 50 μm thick, is stretched along the centre of each tube.

The tubes are used for the measurement of the ionization loss in the calorimeter and for the position measurement of muon tracks with a precision of ≈1 mm. For these purposes both the charge collected at the sense wire (pulse-height) and the drift-time of the electrons in the gas are recorded.

For the ambiguity resolution of straight tracks every third and fourth plane in each module are displaced by half a tube width.

The analogue and digital electronics are mounted directly on the chambers. The digital information is collected by read-out boxes connected to the CAMAC-system.

The chambers are aligned with the use of centring holes at one end and centring slots at the other end. The positions of the sense wires are known with respect to the centring holes with a precision of 0.2 mm. The alignment of the proportional tubes is checked by the use of high-energy muons traversing the detector. The relative positions of the individual wires are known with a precision of 0.3 mm.

3.1.5 The trigger logic

The electronic trigger is based on scintillator information. A discriminator system the threshold of which is set to at least 1/5 of the average energy deposition of a minimum ionizing particle, provides for each scintillator plane the following signals:

1. at least one hit;
2. at least two hits;
3. at least three hits;
4. at least one of the side counters hit (counter 1 and 20);
5. a minimum total energy recorded on that plane.

The plane signals are combined with each other to provide trigger signals corresponding to global requirements at the level of the whole calorimeter. Namely, for each of these five types of basic plane triggers a signal is provided, corresponding to the requirement, that at least one, two, three or four planes give this particular signal. This yields 20 logic pattern signals for the whole calorimeter. In addition, a trigger signal corresponding to a minimum energy deposition in the calorimeter is available. The requirement that a particular plane satisfies one of the five basic conditions can be added to the trigger. This is used to veto incoming charged particles, entering the front of the apparatus. The first scintillator plane covers an area of 4x4 m^2 rather than 3x3 m^2 in order to reject this source of triggers efficiently.

In the narrow-band beam the trigger-rate due to neutrino events is roughly one per accelerator burst for neutrino exposures and five times less for antineutrino exposures. The number of cosmic-ray triggers is reduced by the short gate-time, corresponding to the short accelerator spill. This enables us to choose as trigger a minimum bias trigger corresponding to at least one hit recorded in at least four planes, with the requirement of no hit in the first plane. This trigger corresponds to an energy deposition of ≃1 GeV for showers, and is essentially fully efficient for 1.5 GeV showers as shown in fig.22.

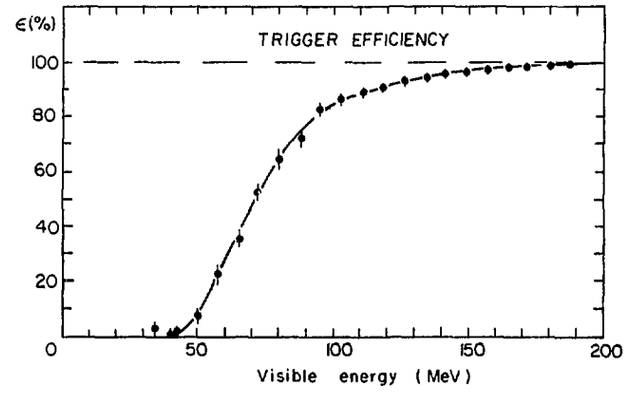

Figure 22: Efficiency of the trigger used in NBB exposures as function of the energy deposition in the scintillators. An energy deposition of 200 MeV corresponds to a hadronic shower energy of 2 GeV for neutral-current events. For charged-current events, the energy deposition of the muon in the scintillators is sufficient for a fully efficient trigger.

The cosmic rate for this trigger is 3500 Hz. With a gate length during the accelerator spill of ≈200 μs, 0.5 to 1 cosmic trigger per burst is accepted. The dead-time is typically ≈10-15%.

3.1.6 The on-line system

The data-taking is steered by two on-line computers (Hewlett Packard 2100 and 21 MXE). One computer (HP 2100) performs the tasks of data acquisition, data-reduction and transfer to tape. Up to 30 neutrino events can be written to tape per machine burst.

Only the non-zero information of the proportional tubes is transferred to the computer and recorded. All scintillator ADC-channels are read-out and checked for consistency and completeness. Only channels with contents corresponding to more than 1/5 ionizing particle are written to tape.

To every event a block is added containing beam-monitor information, the trigger-bit pattern and the contents of some scalers. After every burst a special "monitor-event" is written to tape, which contains beam information and forms a logical separation of machine bursts.

Between machine bursts seven cosmic events are recorded for calibration purposes, and special beam-block events containing information received from the computer of the neutrino facilities monitor (NFM) [41] are written to tape. Every 32 bursts, all ADC-channels are read-out, written to tape, and retained to provide a continuous record of the ADC-pedestals.

One full tape contains ≈30000 triggers, of which in the narrow-band beam a few thousand are taken during the accelerator spill. The rest of the triggers are mainly for calibration purposes.

A selected sample of events is transferred via a link to the other on-line computer (HP 21 MXE). Here hit frequency distributions, pulse-height distributions and other diagnostic information are updated during data-taking, providing a continuous monitor of the detector-operation. An event display and sample analysis of the events and beam-monitor blocks are available.

3.2 MONITORING OF THE NEUTRINO BEAM

3.2.1 Data-handling of beam-monitor signals

The measurements obtained by the various detectors are made available to the on-line system in two ways, namely in the form of direct pulse-trains (hardware information) and information transmitted through one or more computers (software information). The signals transmitted by hardware are recorded on tape as an integral part of the physics events. The software information is received in blocks containing several hundred words, and are recorded block-by-block as special non-physics events.

The organization of data-tapes is synchronized with the machine-bursts in order to be able to correlate the different pieces of information in the off-line stage. The data are recorded in the following sequential order; starting with the first physics-trigger of an SPS-burst:

1. physics-triggers during the burst (zero, one or more up to ≈30);
2. special monitor event to close the burst;
3. 7 cosmic triggers for calibration purposes;
4. pedestal event (one burst out of 32);
5. beam-block events.

This sequence is repeated for every burst. The special monitor event is used to synchronize the sequence and is written for every burst (also if no physics events were recorded and the beam intensity was zero). This event contains, amongst other scalers, a copy of the beam information transmitted by hardware.

The most important scalers are recorded in this monitor-block. Some of them are

BCT signal;

extracted proton beam intensity (SEM);

secondaries produced on the target (SEM);

some muon flux counters in the shield;

pulse-trains from the threshold Cerenkov-counter (this signal is accumulated during the active-time of the apparatus and during the total neutrino burst-gate, to provide a dead-time measurement).

All these signals, apart from the gated pulse-trains, are also available in the data-blocks received from the NFM-computer.

The signals from all beam monitors relevant to the experiment, are available in the software transmitted blocks.

3.2.2 Accumulation of monitor-rates

During the off-line processing of the data, the beam-monitor information is accumulated in order to obtain the integrated intensity of the neutrino beam.

The main points of the scheme adopted in the analysis are described in the following.

Inefficiencies in the transfer of the software data-blocks

As described in section 2.2.2, the signal delivered by the BCT is, after correction for offset currents, digitized by an ADC. The content of the ADC is read by an on-line computer, which transfers the result to the NFM computer. This signal reaches the on-line computer of the experiment via a software link and is called here the software BCT signal. In addition, the ADC content is converted into a pulse-train, which is sent directly to a scaler. The content of this scaler is read by the on-line computer of the experimental set-up. This signal is called the hardware BCT signal. The conversion of the ADC content into a series of pulses is accurate to approximately 1%. Therefore, the BCT signal provided by the software-link is more precise than the accumulated hardware pulse-train. In addition, the software signal is accompanied by the current calibration constant. The main normalization of the beam is provided by the accumulated software signal.

Usually the transfer of the software-blocks is 95%-99% efficient. The missing information is obtained by accumulating the hardware pulse-train during bursts where all information was present and for the burst where the software-blocks were not present separately.

The hardware pulse-train is then calibrated locally and used to fill in the gaps.

Bad quality bursts

It was noticed that the beam quality is likely to be bad for bursts with an intensity much lower than the average. Also possible offsets in electronics providing the monitor signals are relatively more important.

Therefore, thresholds were defined below which an SPS-burst is not used in the analysis. These thresholds are fixed for longer periods, e.g. one SPS-running period, during which the conditions were comparable. This cut is

applied on the hardware BCT signal (see fig.23), which is recorded as a word in every physics event, and in the special monitor event.

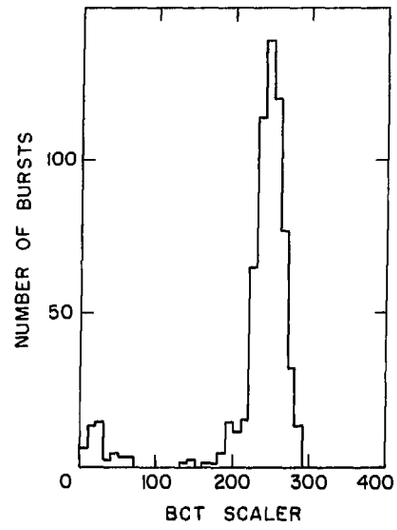

Figure 23: Typical distribution of values of the hardware BCT signal recorded for accelerator bursts during one run. The threshold value is in this case defined at channel 100.

For these bursts all physics triggers, the monitor event, and all software beam-block events are discarded, such that this burst is completely removed. This procedure has the advantage that the data-taking does not need to be interrupted when the accelerator does not operate reliably. The bad cosmic background conditions otherwise introduced are suppressed in this scheme.

Change of conditions

The integration of monitor rates is interrupted when important changes of the operational environment are detected. The main reasons for these interruptions are:

1. change of BCT-amplifier setting;
2. change of run-number (mainly for book-keeping reasons);
3. change of beam settings.

Thus the data are grouped into self-consistent entities. The different parts of data can be added later on, taking the running conditions into account.

Insufficient information

During narrow-band beam exposures it takes about six hours to write a full tape, this tape contains one "run". A few thousand bursts are recorded during one run. The beam quality, the reliability of the intensity monitors, and the efficiency of the transfer of beam information are checked for every run.

The action taken in order to minimize systematic uncertainties is as follows:

1. Runs with a transfer efficiency below 90% are not used for the absolute normalization of the beam.
2. When there is an indication that a particular monitor was not working properly (or its electronics etc.), this monitor is not used. In the

case that other relative monitors, calibrated during neighbouring periods, can provide sufficiently precise information that run is used. Runs, where this is not possible, are discarded for the absolute normalization.

3. Runs with an unsatisfactory beam quality are completely discarded.

Chapter 4

EVENT RECONSTRUCTION

4.1 CALIBRATION

In the first stage of the off-line analysis, a calibration of all pulse-heights is performed. Special tapes containing cosmic ray events are analysed to obtain the attenuation constants of each individual scintillator. These constants vary roughly 1.5% per month and are updated regularly.

Then the cosmic events, recorded during data-taking between the accelerator bursts, are used to establish calibration constants for each scintillator-chain and for the proportional tubes per chamber of 16 tubes. These cosmic-ray events are taken with a trigger requiring a penetration of at least nine planes, in order to suppress large angle tracks.

The response of all scintillator-ADC chains are individually calibrated with signals from cosmic muons recorded between accelerator bursts.

The sensitivity of the system is such that the average signal of a cosmic-ray muon is recorded in channel 30 to 40 of the high-sensitive ADC. The low-sensitive ADC is calibrated with respect to the high-sensitive one with signals in the region where their ranges overlap. These large pulse-heights are not provided by cosmic-ray events, and consequently neutrino-induced showers are used for this calibration.

The saturation limit of the low-sensitive ADC corresponds to ≈150 minimum ionizing particles of a shower crossing one scintillator. Deviations from linearity of the electronics of the scintillator-ADC chains are found to be less than 2% over the whole range. The photomultipliers deviate on average less than 1% from linearity over this range.

The pulse-heights of the tubes are calibrated on a chamber-by-chamber basis using cosmic muon tracks continuously registred during data-taking. The pulse-height measured on a track of a single ionizing particle is determined by the statistical fluctuations of the Landau distribution, the energy-dependent energy-loss, the orientation of the track and space charge effects. A calibration procedure was developed, which is optimized to take the large space-charge effects into account. This procedure only takes tracks with angles less than 45 degrees, and normalizes the tubes to the scintillators for a track at 22.5 degrees. To minimize geometrical effects in this calibration-procedure, only tube-hits are taken without firing neighbours.

These constants are obtained for every tape separately. In a second pass, the cosmic events are filtered out, and the channel contents are converted to energy units, using the previously obtained calibration constants. Intermediate tapes, containing these converted data, are written and used as input for the pattern recognition pass.

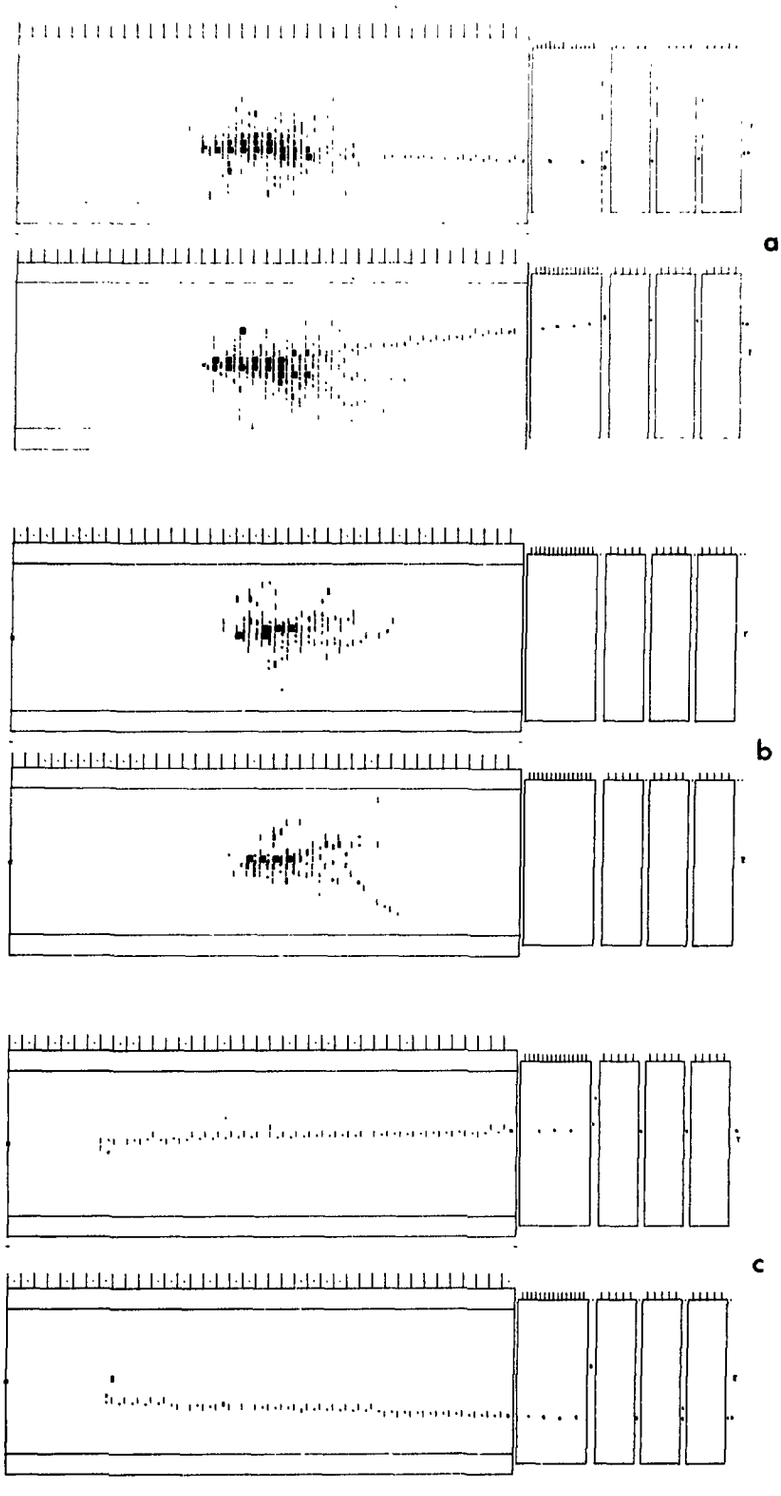

Figure 24: Both projections of the off-line display of a (a) charged-current event (muon and shower), (b) neutral-current event (single shower) and (c) charged-current event (single muon). Vertical bars denote scintillator hits; the thickness of the bars correspond to the recorded energy deposition. Points are drawn for tube hits. The direction of the neutrino beam is from left to right in the figure.

4.2 THE PATTERN RECOGNITION

The pattern recognition program has to cope with different event topologies. These can be classified roughly as follows:

1. Single muon events, i.e. cosmic ray events or neutrino induced events without visible hadronic energy deposition.

2. Muonless events, where only a (hadron or electron) shower is visible.

3. Charged-current events consisting of a hadronic shower and a muon track emerging from the same point. Some of these events contain more than one muon track.

4. Other events like entering muon tracks with bremsstrahlungs showers.

Some off-line event displays are shown in fig.24. First the logic flow of the pattern recognition program will be discussed, then the different processors, which perform the tasks mentioned in the following section will be described in more detail in later sections.

4.2.1 Logic flow of the reconstruction

The first stage of reconstruction is a fast rejection of cosmic-ray events. These cosmic-ray events are recorded during the accelerator spill and fulfil the physics trigger. For events surviving this filter, a search for possible muon tracks, as described below, is made. The tracks found in this stage are classified as shower-tracks or real muon candidates on the basis of their length, and they are classified as tracks entering the front or the sides, or as tracks originating in the apparatus on the basis of their origin.

Before the shower is reconstructed, all real muons are subtracted from the hit and pulse-height patterns, thus only the bare shower is reconstructed. In this stage shower vertex, angle, and energy are determined.

Then an attempt is made to define the momentum of all real muons, which originate in the apparatus, by the deflection in the magnet system. For all muons the minimum momentum is calculated from their range, and their end is defined. For stopping muons the range is used as a momentum estimate.

In the following, the different processors are described in more detail.

4.2.2 The fast cosmic rejection

Events containing a single particle trajectory in the calorimeter, and no other data, are rejected. The tracks are required to enter the apparatus from the start plane or the sides. Tracks of stopping muons, which enter the end or the sides of the apparatus and travel in a direction opposite to the neutrino beam, cannot be rejected. Up to two spurious hits, not lying on the track, are allowed. The total number of cosmic-ray events rejected by this filter is $\simeq 10^5$ for the exposure in the narrow-band beam. This number can be compared with the roughly 15000 neutrino events, which survive all selection criteria, and which were taken during the same exposure. More difficult topologies are rejected after the full reconstruction.

4.2.3 The shower reconstruction

This processor operates on the hit patterns of the scintillators and tubes, after these have been cleaned from muon tracks. In this cleaning procedure the light attenuation in the scintillators is taken into account. The remaining scintillator pulse-heights are also corrected for the attenuation.

The start plane of the shower is defined by the first two consecutive scintillator planes with more than two minimum ionizing particle (m.i.p.) energy deposition. Events where this requirement is not fulfilled, are called showerless. The end is defined by three consecutive planes with less than one m.i.p. The lateral boundaries are defined in a similar way.

The shower energy and barycentres are calculated with the scintillator information inside the box. Tube information in the frames and the end calorimeter is used if the box lies sufficiently close to the edges of the marble calorimeter.

The shower vertex is calculated with an empirical algorithm. The vertex is defined by the intercept of the start-plane of the shower and a straight-line fit to patterns in the first four planes (including the start-plane of the shower). By means of this straight-line fit the energy-flow of the first part of the shower is projected back to the start-plane of the shower, thus providing an estimate of the shower vertex. First, tube hits which cannot be followed to the next plane are removed, in an attempt to remove soft large angle particles from the shower pattern [51].

The elements used in the above mentioned straight-line fit are:

1. the scintillator barycentres on the first four planes;
2. the overall barycentre of the scintillators;
3. the integrated profile of the first four tube planes;
4. all the combinations of clusters on these four tube planes.

Tube clusters are rows of fired tubes on a plane with no gaps. As many fits as there are possible combinations of clusters are performed in this process. The different elements enter in the straight-line fits with a weight according to their pulse-heights. In addition, a narrow tube cluster has more weight than a wide cluster. The relative weight of scintillators and tubes is chosen to give the best results. The straight-line fit with that combination of clusters, which gives the best χ^2 is used to provide the estimate of the vertex position.

For the shower direction an average of two different methods is taken. One estimate is the straight line joining the vertex and the overall scintillator barycentre. The second estimate is formed by the axis through the vertex that divides the tube energy pattern in two equal parts, in each projection. The energy of the individual tubes is weighted with a function which decreases the weight of tubes near the vertex and far from the axis. This weight function enhances the importance of the core of the shower and suppresses fluctuations at the edges of the shower. These fluctuations in the energy deposition are larger in the proportional tubes, because here the charge induced by large angle tracks is collected more efficiently.

4.2.4 Results of the shower reconstruction

Vertex resolution

The resolution, achieved for the vertex of hadronic showers, can be parametrized as follows:

$$\sigma(\text{vertex})_{proj} = \left[\frac{19.5}{\sqrt{(E/GeV)}} + 0.003 \cdot \frac{E}{GeV} \right] \text{cm}$$

where E is the shower energy. In fig.25 this parametrization is shown together with the measurements. The parametrization works for the energy range below 200 GeV; the linear energy-dependence of the second term has no physical meaning. The measured points are obtained from a comparison in charged-current events of the shower vertex and the vertex defined by the muon track extrapolated back to the start plane of the shower.

The quoted resolution function ignores the presence of non-Gaussian tails in the distributions. These tails are taken into account in the analysis.

The resolution expected from the granularity of the detector elements is ≈1.5 cm. The resolution is negatively influenced by the presence of tracks from nuclear fragments travelling in a direction opposite to the shower direction. Also the fact that soft particles at large angles cause more ionization in the gas of the tubes than the leading high-energy particles, makes the vertex measurement more difficult.

In charged-current events, the vertex can be obtained from a combination of the shower vertex and the muon track parameters. This procedure yields at low hadronic energies a considerable improvement compared to the shower vertex alone.

Shower energy calibration and resolution

The energy measurement of hadronic showers was calibrated using showers produced by a beam of momentum-selected pions. A calibration factor was measured for various energies between 15 and 140 GeV. The calibration factor varies slowly with energy as shown in fig.26.

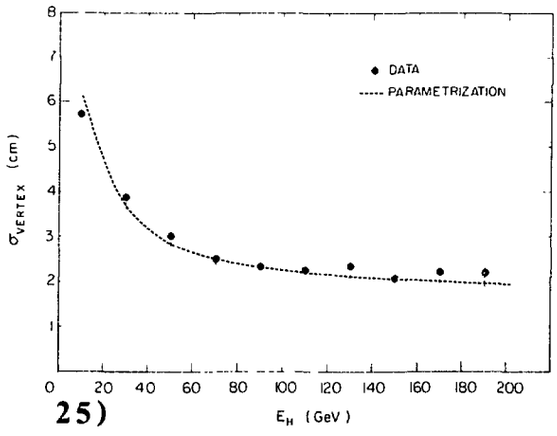

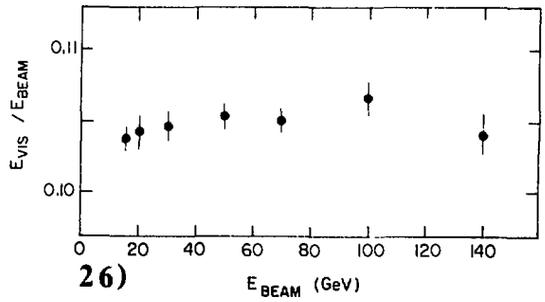

Figure 25: Measured vertex resolution for hadronic showers.

Figure 26: Measured energy calibration factor for hadronic showers.

The energy resolution was also obtained in this way and is represented by a simple energy-dependence:

$$\sigma(E)/E = 0.53 / \sqrt{(E/GeV)}$$

This functional form is expected in calorimetric energy measurements; the number of particle tracks is roughly proportional to the shower energy, which introduces the statistical square-root. A part of the energy of a hadronic shower is released by electromagnetic cascades. Roughly half of the resolution is explained by the variation in the fraction of the electromagnetic

part, and by nuclear binding effects. The resolution is larger than this minimum because the energy released in the active part of the calorimeter is a fraction of the total energy deposition.

Shower angle resolution

The measured shower angle is a result of the average of the method based on the barycentre of the scintillators and the method based on tube information. The two methods, applied separately, give comparable results. In the energy range below 30 GeV almost no improvement is seen averaging the two estimates. This indicates, that the statistical fluctuations of the shower dominate the resolution. For higher energies, the combination of the two estimates gives a considerable improvement compared to the individual results.

The resolution of the angle measurement of hadronic showers was measured using showers produced by the pion beam. The angular resolution can also be measured using the coplanarity requirement of the muon track and the shower vector in charged-current events. Both measurements give the same results. If the vertex obtained from the shower alone is used, the resolution can be parametrized as:

$$\sigma(\theta)_{proj} = \left[\frac{0.16}{\sqrt{(E/GeV)}} + \frac{0.56}{E/GeV} \right] \text{rad}$$

An improvement is obtained for showers where the muon can be used to define the vertex. In this case the resolution can be parametrized as follows:

$$\sigma(\theta)_{proj} = \left[\frac{0.16}{\sqrt{(E/GeV)}} + \frac{0.20}{E/GeV} \right] \text{rad}$$

Both cases of the angular resolution are shown in fig.27.

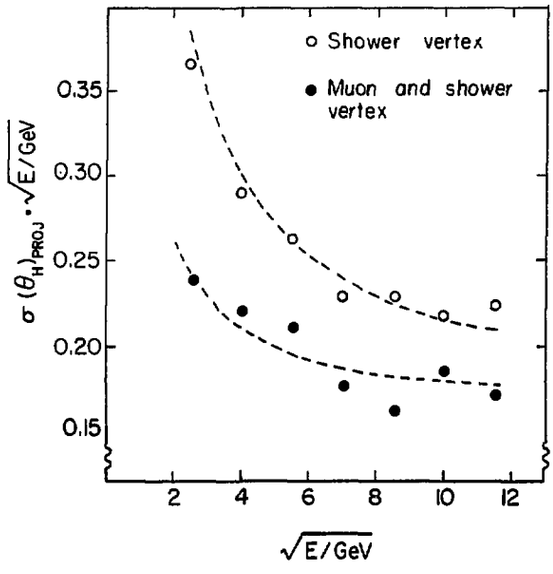

Figure 27: Measured angular resolution of hadronic showers when the shower vertex is used (open circles) and when the muon is used to define the vertex (full circles). The curves are parametrizations given in the text.

The measured points are obtained by the coplanarity method in charged-current events.

The angular resolution of the shower has non-Gaussian tails, due to the influence of the vertex measurement.

4.2.5 The track-finding

The search for muon tracks operates on the signals measured by the proportional drift tubes [52]. The pulse-height information is used, but no use is made of the drift-time information. The algorithm is developed empirically. It was optimized to match the details of the functioning of the proportional drift tubes. The algorithm is based on the high efficiency of the tubes for the recording of muon tracks (≈93%).

The track-finding is preceded by a blanking procedure with the aim of removing all hits associated with the shower and to retain a sufficient number of hits on the muon tracks. The blanking algorithm uses the following criteria either to remove or retain a recorded hit.

1. No hits are removed on planes with less than three signals.

2. On other planes, any signal above a certain threshold is removed, unless it is an isolated hit (no fired neighbour within four tubes on either side). The threshold is chosen such that signals due to one traversing track are accepted for the largest fraction of the Landau distribution, taking the relativistic rise effects into account. If a signal is removed its direct neighbours are also taken out. This is repeated for every neighbour of a removed tube. In the magnet system, the threshold is set higher because here the problem of shower-associated hits is smaller.

3. An additional requirement is imposed on the signals in the last four planes of the end magnet. Here we have a double measurement of the track and keep only those hits, corresponding to a hit on the other plane of the same projection, unless all hits are lost by this requirement.

4. If the end calorimeter has very few signals in total, but the end magnets contain a number of hits consistent with a track, signals corresponding to the hole positions are generated in the end calorimeter. This is done in order to avoid an inefficiency induced by the hole in the end calorimeter. If no track can be associated with these generated hits, they are deleted in a later stage of the track-finding.

Strictly speaking, the latter point does not belong logically to the blanking procedure, but more generally to the preparation of the hit-pattern used as input for the track-finding. After the blanking has been performed, tracks are searched for, using the remaining hits.

The track-finding starts with a combinatorial search for tracks in the end system. The basic assumption is made that tracks in the end system are well enough represented by parabolae. The search is made in the two projections separately, and only in the non-inclined planes. Points are joined into tracks in two passes. In the first pass only tracks which traverse the whole end system are found, with strict criteria on the points lying on a parabola. In the second pass, also shorter tracks can be found with larger tolerances. In both cases, a check on the curvature of the parabola is made, the parabola being defined in a rotated coordinate system with the end points of the track defining the abscissa of the coordinate system.

The tracks found in the projections are then matched into tracks in space using the information of the inclined chambers. The check on the inclined chambers is only required in the case that more than one track is found in a projection. In this case the projections are matched only if two inclined planes have hits in the predicted points.

Tracks in the target calorimeter are followed in a plane-wise backward search. Hits are assigned to tracks in the following hierarchical order:

1. First an attempt is made to continue tracks already found in the end system.

2. Then, an attempt is made to join hits to tracks which terminate in the target calorimeter.

3. On hits still remaining, the hypothesis is tested, whether they can be the end of a track stopping in the target calorimeter. This is done by a search for straight-line combinations with points on the two preceding planes.

In this stage of the search, no hits can be common to two or more tracks. Tracks which have not been continued for two planes in the projection are marked as being complete, and no further continuation will be attempted for these tracks. In this search a hit is joined to a track if it lies sufficiently close to the straight-line prediction of the three preceding points; also a check on the change of slope is made.

After the pass through the calorimeter is complete, the tracks are checked for their straightness. Tracks may fail this test if they are in the iron, or if it has been wrongly followed in the shower region. In this last case, the first points are removed until the first three points are on three consecutive planes.

In the target calorimeter, no information from inclined wires is available and tracks are matched on the basis of their total length and the position of their mid-points and finally on the basis of their end-points.

Points which had been lost by the blanking procedure, are restored to the track. At the end of the track, an extrapolation is made to prolong the track if possible. As a last step, an attempt is made to join tracks which have been found in two sections into one, on the basis of their straight-line parameters.

In events where no tracks are found, a search for large angle tracks is made on the partially blanked hit pattern. The blanking procedure can erase information of large angle tracks due to the larger pulse-heights in the tubes and a geometrically increased probability of firing neighbour-tubes.

The efficiency of the track-finding is checked by an eye scan of the events. The reconstruction efficiency is ≈99.5%. The lost tracks are predominantly large angle tracks of which one projection is hidden by the shower, and tracks traversing the holes in the end calorimeter.

4.2.6 The muon momentum fit

Muons produced in the target calorimeter and which traverse a sufficient amount of iron, are fitted by a classical least-squares method, based on the fit used in the CERN Split Field Magnet detector [53]. The logic is divided into three distinct sections:

1. the point selection;

2. the ambiguity resolution;

3. the fit proper.

The point selection

The point selection starts with the classification of tracks as frame-tracks, end-tracks, mixed-tracks (seen in the frames and in the end system) and tracks consisting of insufficient points. The latter class consists of e.g. tracks

of muons stopping in the marble or in the iron before a sufficient number of counters inside the iron is hit, or steep tracks leaving the sides of the apparatus.

The minimum requirement is six points for end system tracks, and eight points for frame-tracks. In the geometry-fit, the drift-time information of the tubes is used, which forces a strict point selection. The following criteria are used to discard hits, where the drift-time information is considered to be unreliable:

1. The pulse-height is too large, which distorts the drift-time drift-distance relationship, and may mean it is contaminated by the shower or by bremsstrahlung.

2. It has first or second neighbours, unless it is the member of a double-hit, in which the sum of the two drift-distances yields the distance between two adjacent wires. The latter property is also used to resolve the left-right ambiguity for this hit.

In this way up to five hits are selected in each projection in the target calorimeter, in the planes preceding the start of the track in the iron; up to 14 hits in the magnet system are selected. The selection criteria are less strict for short tracks, where all reasonable signals are taken.

When the energy deposition measured by the scintillation counters inserted in the gaps between the discs of the end magnet is inconsistent with the energy deposition of a muon track alone, the track is treated specially at this point. If the hit-multiplicity is consistent with the number of muons, the energy deposition is used in the fit to correct the track-parameters at that point; if the multiplicity is higher, the track is cut at this point and only the first part is used in the fit.

The ambiguity resolution

The left-right ambiguity in the position measurement using the drift-times is then resolved. First, all possible straight-line fits are tried through the points on the straight section. The best solution is used to fix the ambiguity of one point, which will be used in the fit, and a point on the magnet face is generated. This point, together with the ambiguity resolution provided by the double measurement of the last four planes is used to fix the end points for the ambiguity resolution inside the magnet system.

These ambiguities are resolved trying all possible parabola-fits through the points on non-inclined planes. The ambiguities on the inclined wires are resolved by a comparison with the prediction of the best parabola on this plane.

The fit

The muon momentum is obtained by a least-squares fit to the track positions obtained with the drift-times.

The estimate of the weight matrix is done following a method due to Regler [54] and implemented by Frühwirth [55].

In this method the multiple scattering and energy-loss are taken into account. Depending on the nature of the material traversed by the particle, the scatterer is treated as a continuous or discrete scatterer.

The actual fitted parameters are the two projections of a point on a reference plane, two direction cosines and the inverse momentum. In a first attempt, all points are used with their drift-time information, yielding a position measurement with a precision of the order of 1 mm, rather than the ≈9 mm corresponding to the 3 cm tube granularity. Roughly 75% of these fits are succesful above the 0.001 probability level.

In subsequent trials one or more position measurements are replaced by their wire position and correspondingly larger resolution. The selection of points to be degraded is done on the basis of their drift-times. Smaller

drift-times are more likely to be generated by extra particles, or δ-rays; in addition, the ambiguity resolution is more likely to fail for short drift-distances. The fit yielding an acceptable χ^2 with the least number of points degraded is than taken as the final estimate. This procedure yields finally ≈5% of the tracks fitted with only the wire coordinates as momentum estimate.

The efficiency of the momentum fit is 95% for tracks which have a sufficient number of points measured on the track. The additional geometrical inefficiency is ≈12% for the narrow-band beam spectrum. This geometrical inefficiency is caused by steep tracks leaving the sides of the apparatus and by a small number of straight tracks traversing the hole in the end system.

The momentum of stopping muons can be obtained from their range. This is the only way to define the momentum of muons stopping in the marble part of the calorimeter. For some muons stopping in the end system, the momentum can be obtained from both the magnetic deflection and the range. A comparison of the two different momentum estimates is shown in figure 28.

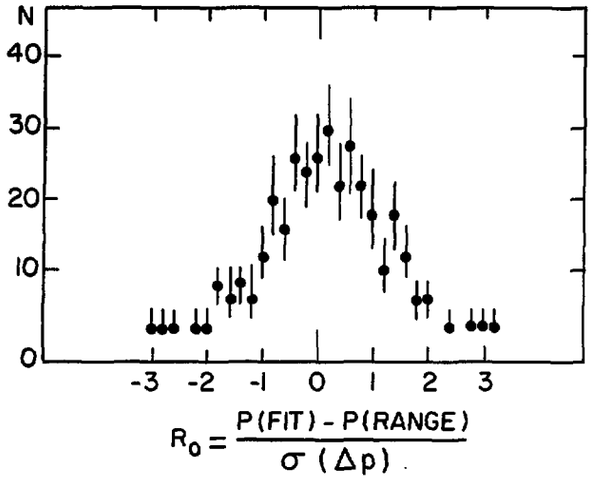

Figure 28: Comparison of muon momentum obtained by the range and by the magnetic deflection.

4.2.7 Muon momentum resolution

The measurement error in the muon momentum is the result of multiple scattering in the iron disc-magnets and of the limited chamber resolution. The first gives rise to a constant term in the relative resolution, the latter to a momentum dependent term.

For ideal tracks, i.e. tracks visible along a straight section before the magnet system and traversing the complete end system, the average relative resolution, $\sigma^0(p)/p$, for a momentum, p (given in GeV/c), is

$$\sigma^0(p)/p = \sqrt{\{(0.14)^2 + (0.001 \cdot p)^2\}}$$

The two terms yield equal contributions for 140 GeV muons.

An estimate of the variance of each individual fit is calculated during the fit. This estimate is used to analyse the distribution of normalized relative measurement errors $\sigma(p)/p \;/\; \sigma^0(p)/p$ (fig.29(a)). The actual shape of the distribution making up this average is only very slightly momentum dependent. It is well described by three components (fig.29(b)):

1. a peak at $0.85 \cdot \sigma^0(p)/p$ for ≈80% of the cases;

2. a shoulder around $1.3 \cdot \sigma^0(p)/p$ for ≈12% of the fits;

3. a tail around $3.0 \cdot \sigma^0(p)/p$. The population of this tail is ≈5% for low momenta and increases to ≈10% at 200 GeV.

For less ideal tracks, the resolution is modified. Tracks without a straight section in the marble calorimeter show an enhancement of the shoulder. Tracks not traversing the whole end system, i.e. stopping tracks, tracks partly traversing the holes, and tracks leaving the sides are fitted with a resolution according to the amount of magnetized iron seen. The worsening factor is shown in fig.30.

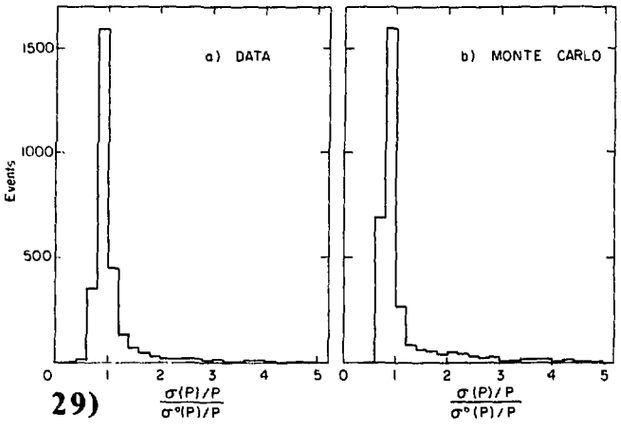

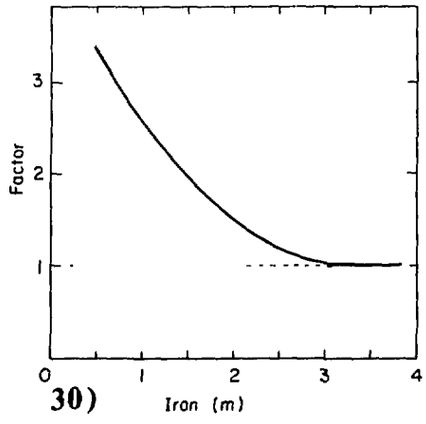

Figure 29: Normalized relative measurement errors for the muon momentum fit. Shown are the measured (a) and simulated (b) distribution for muons traversing the end system.

Figure 30: The factor, by which the muon momentum resolution is degraded when a muon traverses less than the maximum amount of magnetized iron. For muons traversing less than 0.5 m, the deflection is not sufficient to measure the momentum.

4.2.8 The muon angle measurement

The muon angle is measured in the marble part of the calorimeter. For this purpose a section of the track is defined as close as possible to the shower region, only using points not likely to be contaminated by the shower.

The length of the section is defined matching the position measurement error to the uncertainty introduced by multiple scattering. The point selection uses criteria similar to those used in the momentum fit.

The straight-line fit uses the drift-time information of the tubes. If this treatment does not yield an acceptable χ^2, or the number of points measured on the track is insufficient to resolve the ambiguities of the position measurement, a fit to the wire-position on a longer section is performed. The fit to the wires is only necessary in 5% of the cases.

If the track is not visible for a sufficiently long section in the marble, the first few points in the frames are accepted in the fit; for tracks only seen in the end system, the direction-cosines of the momentum-fit are used for the angle measurement.

Angular resolution of muon tracks

In the straight-line fits only the diagonal elements of the weight-matrix are used, giving an estimate of the measurement error which is too small. An average correction factor is used afterwards to account for this approximation.

The resolution of the angle of muon tracks follows directly from the error on the straight-line fit and the multiple scattering on the part of the

track obscured by the shower. The error in the measurement of the slope of the straight track is given by the length of the section used, the number of measurements on that section and the multiple scattering. The length of the straight section depends strongly on the actual geometry of the event and on the length of the shower.

In fig.31, the range of measurement errors as a function of the muon momentum is shown.

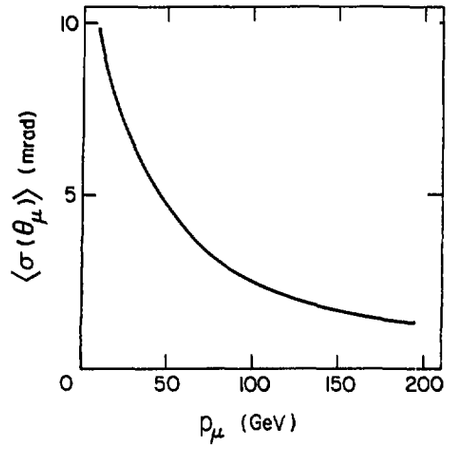

Figure 31: Average muon angular resolution as function of the momentum. The multiple scattering in the region inside the shower, where the muon is not visible, is taken into account in addition to the uncertainty in the measurement of the angle of the visible part of the track.

4.3 THE KINEMATICAL FIT

4.3.1 Measured kinematical quantities

An ideal reconstruction of charged-current events yields the following kinematical quantities:

1. the muon momentum;
2. the shower energy;
3. both projections of the muon angle;
4. both projections of the shower angle;
5. the knowledge of the vertex position giving the neutrino energy in the narrow-band beam (section 2.3.3).

The full kinematics of an event is determined by a subset of these quantities. This makes it possible to impose a few constraints on the measurements and hence to improve them. The constraints are in this case energy and momentum conservation giving three additional relations between the variables.

The measurement of the neutrino energy suffers from an ambiguity introduced by the dichromatic spectrum. This ambiguity is resolved with the use of the other information available. An estimate of the neutrino energy is obtained fitting all available measurements, excluding the knowledge of the beam spectrum. This estimate is compared with the two possible beam energies. The energy which suits better is assigned as an extra measurement.

With this complete set of measurements a second fit is attempted providing the best possible estimate of the kinematics.

For events, where not all quantities are reconstructed, some relations are lost. The following cases can occur:

1. Muon momentum not reconstructed (neither by magnetic deflection, nor by range): two relations are left, the constraint of energy-balance is lost.

2. Before the ambiguity due to the neutrino energy spectrum is resolved, the neutrino energy is not known: again only two relations survive. In the subsequent second fit the neutrino energy obtained from the radius of the interaction is used, adding a constraint in the second fit in this case.

3. Both muon momentum and neutrino energy unknown: only one relation (co-planarity) is available.

4. The shower angle is not reconstructed (this happens for low-energy showers only): one relation (energy balance) remains.

5. In some cases, the kinematics is not overdetermined and no fit can be performed. This occurs when e.g. only the muon momentum, muon angle and shower energy are known.

4.3.2 Fit method

The fit uses a χ^2-minimization procedure, the constraints are introduced with the method of Lagrange-multipliers [56].

The least-squares method requires a normal distribution of measurement errors. This is not the case for the error of the muon momentum. The magnetic deflection is more related to $1/p$ and therefore the error in $1/p$ will be approximately normally distributed. In all other measurements the normal distribution is a fair approximation of the actual distribution. Hence the fit varies the inverse of the muon momentum and the other quantities as they are defined in the previous section.

From the way the measurements are obtained in the reconstruction program, it is clear that a diagonal covariance matrix can be used. In some cases, this is only an approximation, e.g. for events where the muon is used to improve the vertex estimate of the shower for the shower-angle measurement. Here a small correlation of the muon and shower-angle error is neglected.

The errors on the individual measurements are estimated either on an event-by-event basis, where the reconstruction program gives an estimate of the error (muon momentum and angle), or by means of a parametrization in the other cases.

Chapter 5

EXPERIMENTAL RESULTS

In this chapter results on total and differential cross-sections will be presented. The first section deals with the measurement of total cross-sections of both charged and neutral-current neutrino and antineutrino interactions. The second section describes the analysis of differential cross-sections of charged-current interactions.

5.1 TOTAL CROSS-SECTIONS

Total cross-sections of neutrino and antineutrino interactions were obtained using data taken in the CERN 200 GeV narrow-band neutrino beam (section 2.2.1). The momentum of the extracted proton beam was 400 GeV/c. Roughly 2×10^{18} protons on target were collected during a running period of in total four months.

First the method used for the normalization of the neutrino flux and the event selection will be discussed. Then results on total cross-sections and neutral-current coupling constants will be given.

5.1.1 Normalization of neutrino fluxes

The neutrino and antineutrino fluxes were obtained with a method combining measurements obtained with the beam current transformer in the secondary hadron beam and solid-state muon counters in the iron shielding (section 2.2.2 and 3.2.2). For the calculation of the absolute neutrino flux one has to know the number of pions and kaons in the decay tunnel, the branching ratios of the decays of these particles into neutrinos (section 2.3.4), and the properties of the secondary hadron beam. The latter is required in order to be able to calculate the energy spectrum and the radial dependence of the neutrino flux. Some of the neutrinos in the beam do not enter the fiducial volume of the neutrino detector due to the width of the neutrino beam. Hence the fiducial volume and the resolution of the measurement of the interaction vertex have to be taken into account in the calculations. In all calculations the divergence of the secondary hadron beam was taken 10% larger than the nominal divergence, as indicated by the energy-radius correlation measured in the neutrino detector.

The beam current transformer in the secondary beam provides a good measurement of the total number of pions and kaons in the antineutrino beam; the contribution of antiprotons is small ($\approx$0.6%). In the neutrino beam, the pion and kaon fluxes are much more uncertain because of the large proton content of the positively charged hadron beam ($p/\pi = 4.4 \pm 0.2$) [44]. The shield measurement of the ratio of the muon fluxes in the neutrino and antineutrino beams is not affected by this problem. Therefore, we have used the beam current transformer to obtain the absolute antineutrino flux, and the solid-state muon detectors to measure the ratio of the neutrino and antineutrino fluxes.

The absolute calibration of the beam current transformer is known to $\pm$3% [44], while its temporal stability is estimated to be better than 1% as a result of a check against ionization chambers both in the secondary beam and in the shield, and against the solid-state muon counters in the shield. The relative calibration of the solid-state detectors is known to better than 1%

[47], thus the effect of variations in the beam steering on the total muon detection efficiency is smaller than 0.5%. An absolute calibration of these detectors is therefore unnecessary.

The secondary hadron beam is accompanied by low-energy electrons produced in the matter (foils, air) traversed by the beam. A correction of 5.5% ± 3% was applied to the signal of the beam current transformer for the contribution of these δ-rays [44]. The magnitude of this correction is obtained by a comparison of the signal of the BCT and the signal of the differential Cerenkov counter in the negative and positive hadron beam. The Cerenkov counter is only sensitive to relativistic particles, while the BCT also records the current induced by soft electrons. The current induced by the soft particles does not change sign when the beam polarity is changed, and hence a comparison of the ratio of the BCT and Cerenkov signals for different polarities measures the contribution of soft particles. This ratio changes by (11 ± 2)% when the beam changes polarity. With the assumption that the contribution of soft particles is equal for both beam polarities one obtains a correction of 5.5%. An extra uncertainty is assigned to this value due to the uncertainty in the assumption of equal contributions of the soft particles for both beam polarities. The component of this secondary radiation, which is sufficiently relativistic to be measured by the Cerenkov counter, adds to the Cerenkov signal in both beam polarities. Hence this contribution cancels when the ratio of the Cerenkov signal in the positive and negative beam is taken, and does not change the argument.

The detection efficiencies for muons produced by the decays of pions and kaons in the secondary hadron beam are different. This effect was estimated by a Monte Carlo simulation of the muon trajectories in the shielding. According to the calculation described in section 2.3.5, the acceptance of the solid-state detectors for muons from kaon decay is a factor of 1.30 ± 0.08 higher than for muons from pion decay. The uncertainty in this number is mainly due to the uncertainty in the divergence of the hadron beam. Corrections corresponding to the different K/π ratios were applied.

The flux of muons measured in the shielding was corrected for contributions from particles decaying before the momentum-defining slits. This background was determined experimentally with the momentum slits closed; it amounts to (4.1 ± 0.2)% in the neutrino beam and (3.4 ± 0.2)% in the antineutrino beam.

The uncertainty in the ratio of the neutrino and antineutrino fluxes is given by the uncertainty of the relative muon fluxes, and is estimated to be 2%. The acceptance calculation for the detection of muons contributes an 0.8% uncertainty, other contributions are due to electronic instabilities of the solid-state detector system and the beam jitter (≃1%), and the subtraction of background muons. The absolute flux, measured in the negative beam is known with a precision of 5%, mainly due to the calibration of the BCT and the correction for δ-rays.

Dead-time effects in the neutrino detector were corrected using a signal from a threshold Cerenkov counter placed in the beam line and recorded independently during the active time of the target calorimeter and the gate time.

In order to have a consistency check on the monitoring of the neutrino beam, we have determined the event rate normalized to the absolute neutrino flux for different samples of the data. The spread of the distribution of these normalized event rates is compatible with being purely statistical (fig.32).

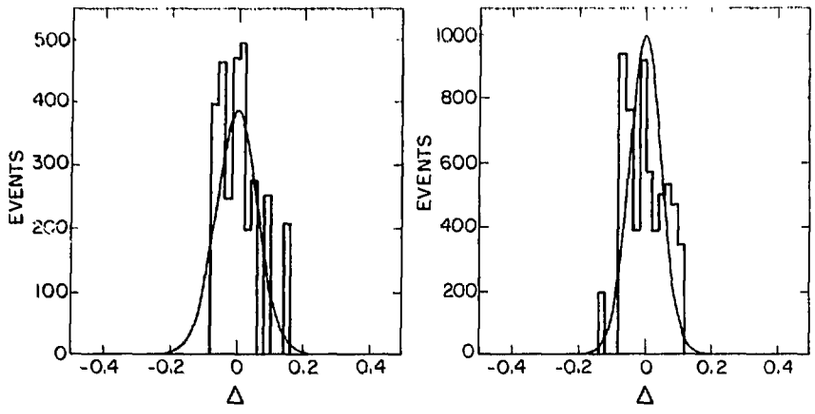

Figure 32: Spread of event rate (NC + CC) normalized to the total neutrino flux for (a) antineutrinos and (b) neutrinos. The events have been divided into sub-samples in chronological order. For each sub-sample the number of events, normalized to the neutrino flux, is plotted against the relative deviation from the global mean. The curve shows the distribution expected for purely statistical deviations.

5.1.2 Selection criteria and corrections

The fine spatial resolution of the calorimeter is such that classification of events as neutral-current (NC) or charged-current (CC) candidates may be made on an event-by-event basis.

The criteria used to select neutrino interaction candidates were the following:

1. The interaction vertex lies within a fiducial volume chosen to ensure good pattern recognition and low background conditions; this fiducial volume covers an area of 120 cm (90 cm) radius perpendicular to the beam axis in neutrino (antineutrino) exposures, and extends longitudinally from target plate 7 to target plate 60, inclusive, corresponding to a target mass of 65 (37) tons. The end of the fiducial volume was chosen in order to ensure a good muon recognition. The six active plates in front of the fiducial volume ensure an efficient suppression of events induced by entering particles. The radial fiducial cut of 120 cm in neutrino exposures was applied for the pattern recognition. This radius was chosen to be 90 cm in antineutrino exposures in order to suppress wide-band background, which is relatively more important at large radii.

2. The event contains no charged track entering the front or the sides of the detector.

3. The shower energy is greater than 2 GeV. The shower energy cut ensures a full trigger efficiency for events satisfying the selection criteria. This requirement is not necessary for CC events, where the energy deposition of the muon is sufficient for a fully efficient trigger. Therefore, for some analyses of CC events where no comparison with NC events had to be made, this requirement was dropped.

The neutrino event candidates were classified as CC or NC interactions according to the following criteria:

1. A CC event has a track identified as a muon associated with the interaction vertex (a track is called a muon if it has a range corresponding

to more than 1.0 GeV/c and if it is clearly visible outside the hadron shower for a length corresponding to a range of more than 0.67 GeV/c; the track is further required to have no kink or interaction within the ranges defined above).

2. All other events are classified as NC.

The automatic reconstruction and classification of all NC candidates have been verified by an eye scan. The 5% wrong classifications of these candidates were corrected individually. In the case of CC candidates, a sample was scanned and a correction, amounting to nine out of 9000 CC events, was applied accordingly.

We thus find 9000 neutrino and 4000 antineutrino CC and NC events (see table 5).

TABLE 5
Corrections to raw event numbers for showers > 2 GeV.

	$\bar{\nu}$		ν	
	NC	CC	NC	CC
Raw event numbers	1126 ± 34	2751 ± 53	2361 ± 49	6503 ± 81
Wide-band and cosmic background	-143.8 ± 26.3	-244.0 ± 35.1	-95.4 ± 11.6	-112.6 ± 13.1
μ selection criteria	-22.6 ± 2.2	+22.6 ± 2.2	-96.5 ± 9.3	+96.5 ± 9.3
K and π decay in flight	+15.2 ± 3.1	-15.2 ± 3.1	+53.5 ± 10.9	-53.5 ± 10.9
ν_e events from K_{e3} decay	-26.4 ± 3.0		-163.6 ± 10.0	
Corrected event numbers	948.3 ± 43.3	2514.4 ± 63.7	2059.0 ± 53.5	6433.4 ± 84.3

These two samples of data were corrected for backgrounds and for various effects mixing NC and CC events. The following corrections have been considered:

1. The wide-band background of events induced by neutrinos and antineutrinos produced by the decay of hadrons before the momentum slits in the beamline is evaluated using special runs during which the momentum slits were closed. The exposure in these runs is normalized relative to the normal data-taking exposure, using the secondary beam intensity as monitored by the secondary emission foil downstream from the target.

2. The number of cosmic-ray events classified as neutrino events is obtained by analysing data taken under identical trigger conditions while the accelerator was off. The total contribution of these events is small.

3. The number of events lost by the automatic pattern recognition is determined by an eye scan of a sample of the rejected events. On the basis of this scan we have added 21 (15) NC events and 16 (12) CC events to the neutrino (antineutrino) event samples.

4. The selection criteria for muon tracks results in a number of CC events being classified as NC events. This effect is mainly caused by muons leaving the sides of the detector before being identified and, to a lesser extent, by muons obscured by the hadronic shower. The contributions were evaluated using a semi-Monte Carlo method, where Monte Carlo generated muons were superimposed on showers of real events and then reconstructed.

5. The decay in flight of pions and kaons in the shower can produce a muon track which satisfies the selection criteria for CC events. This correction was determined experimentally from an analysis of dimuon events [57]. The origin of the second muon in dimuon events was compared with the origin of the primary muon. Using the relative distance of the two muons as a criterion, the secondary muons from pion and kaon decays can be separated from muons created at the vertex (e.g. from charmed meson decays). In this way the number of decay muons satisfying the selection criteria was obtained normalized to the number of hadronic showers. The probability for such a muon was found to be proportional to the shower energy.

6. The narrow-band beam contains a component of electron-neutrinos from K_{e3} decays. Neither their CC nor NC interactions give a muon in the final state, and have to be subtracted from the NC sample. The correction is calculated using the known K-decay branching ratios [45] and assuming electron-muon universality.

5.1.3 Total cross-sections

From the corrected event numbers listed in table 5 we obtain directly the following cross-section ratios on an isoscalar target for the shower energies above 2 GeV:

$$R = \frac{\sigma(\nu N \to \nu X)}{\sigma(\nu N \to \mu^- X)} = 0.320 \pm 0.010$$

and

$$\bar{R} = \frac{\sigma(\bar{\nu} N \to \bar{\nu} X)}{\sigma(\bar{\nu} N \to \mu^+ X)} = 0.377 \pm 0.020$$

The systematic error in these results is small (about one third) compared to the statistical one.

Measurements of the ratio of the neutral-current and charged-current cross-sections reported by other experimental groups [58,59,60,61,62] are compared with the results of this analysis in table 6. In addition, the various shower energy cuts applied in the analyses are listed for completeness.

TABLE 6
Comparison of neutral to charged-current ratios.

	target material	R	$\bar{R}$	E_h cut
CHARM	marble	0.320 ± 0.010	0.377 ± 0.020	2 GeV
GGM	freon	0.26 ± 0.04	0.39 ± 0.06	0 GeV
HPWF	liquid scintillator	0.29 ± 0.04	0.39 ± 0.10	4 GeV
CITF	iron	0.27 ± 0.02	0.40 ± 0.08	12 GeV
BEBC	NeH_2	0.32 ± 0.03	0.39 ± 0.07	15 GeV
CDHS	iron	0.307 ± 0.008	0.373 ± 0.025	10 GeV

Making use of the absolute normalization of the neutrino fluxes and weighting the spectrum assuming a linear rise of the cross-sections with neutrino energy in the laboratory frame, E, we measure the total CC cross-sections of neutrinos and antineutrinos on an isoscalar target (including the quasi-elastic contributions):

$$\sigma_{tot}(\nu N \rightarrow \mu^- X) = (0.604 \pm 0.032) \times 10^{-38} \times E \text{ cm}^2 \text{ (GeV nucleon)}^{-1} \quad (42)$$

$$\sigma_{tot}(\bar{\nu} N \rightarrow \mu^+ X) = (0.301 \pm 0.018) \times 10^{-38} \times E \text{ cm}^2 \text{ (GeV nucleon)}^{-1} \quad (43)$$

These total cross-sections were obtained for the full neutrino energy spectrum, effectively averaging over the range 20 to 200 GeV (fig.15). No shower energy cut was applied in this case. No absolute normalization of the neutrino fluxes is needed for the ratio of the charged-current neutrino and antineutrino total cross-sections. With the relative normalization of the neutrino and antineutrino fluxes measured with the muon counters in the shielding we obtain:

$$r = \frac{\sigma(\bar{\nu} N \rightarrow \mu^+ X)}{\sigma(\nu N \rightarrow \mu^- X)} = 0.498 \pm 0.019$$

again without shower energy cut. The CC cross-section ratio with a 2 GeV shower energy cut is needed in order to be able to compare NC and CC cross-sections (e.g. in the Paschos-Wolfenstein relation equation (2)). When this cut is introduced we obtain:

$$r(E_h \geq 2 \text{ GeV}) = 0.470 \pm 0.017.$$

The 2 GeV cut in shower energy removes the contribution of quasi-elastic events efficiently. These events represent the coherent interactions of neutrinos with the whole nucleon and do not probe the internal structure of the nucleon. The cross-section ratio obtained for a 2 GeV shower energy cut can be corrected for this cut, explicitly neglecting the quasi-elastic contribution. In this way an inelastic cross-section ratio was obtained, $r_{inel} = 0.492 \pm 0.019$, which can be interpreted in terms of the quark-parton model. With the assumption of equal fractional antiquark contributions probed by neutrinos and antineutrinos, we obtain (equation (31)):

$$\frac{\bar{q}}{q+\bar{q}} = 0.16 \pm 0.01$$

The antiquark contributions for neutrino and antineutrino interactions separately will be obtained from the y-distributions.

Assuming that the Callan-Gross relation (equation (11)) is valid and that the structure functions are equal for neutrino and antineutrino interactions, we evaluate the momentum sum rule (equation (32)) for the energy range of this experiment, interpreted in the quark model as the fractional momentum carried by the quarks and antiquarks in the nucleon (section 1.3.10):

$$\frac{3\pi}{4G^2ME} \left[\sigma_{tot}(\nu N \rightarrow \mu^- X) + \sigma_{tot}(\bar{\nu} N \rightarrow \mu^+ X) \right] = \int_0^1 F_2(x)dx = 0.44 \pm 0.02$$

from the sum of the total cross-sections quoted in equation (42) and (43). This result suggests that roughly one half of the momentum of a nucleon is carried by non-weakly interacting partons.

In table 7 the total cross-sections obtained in this experiment are compared with other experimental results [63,64,65,66]. All quoted cross-sections are averaged over a comparable energy range, roughly 20-200 GeV. The various experimental results agree with each other, with the exception of the CFRR (Caltech-Fermilab-Rochester-Rockefeller) result. The reason for this discrepancy is not known. The ratios of the cross-section of neutrinos and antineutrinos agree. This implies that the absolute scale of the flux normalization measured with the BCT at CERN and with a ionization chamber in the

case of the CFRR experiment do not correspond. The flux normalization of the negative beam at CERN using the solid-state muon counters, which provide a measurement of comparable quality, agrees within 3% with the BCT normalization [67].

TABLE 7
Comparison of total cross-sections.

	target	neutrinos	antineutrinos	ratio (r)
CHARM	marble	0.604 ± 0.032	0.301 ± 0.018	0.498 ± 0.019
CITF	iron	0.609 ± 0.03	0.290 ± 0.015	0.476 ± 0.019
BEBC	NeH_2	0.63 ± 0.04	0.29 ± 0.02	0.46 ± 0.04
CDHS	iron	0.62 ± 0.03	0.30 ± 0.02	0.48 ± 0.02
CFRR	iron	0.719 ± 0.036	0.371 ± 0.019	0.516 ± 0.009

x 10^{-38} x E cm^2 (GeV nucleon)$^{-1}$

5.1.4 Energy-dependence of the cross-sections

The energy-dependence of the total cross-sections was obtained measuring the cross-sections separately for two parts of the neutrino spectrum. A natural choice was the separation into the kaon part and the pion part of the neutrino spectrum.

In order to increase the statistics of the high-energy part of the antineutrino data the radius of the fiducial volume was taken to be 120 cm rather than 90 cm. The increase of the wide-band background otherwise introduced was suppressed by a cut of 30 GeV in the measured neutrino energy. For the purpose of this cut the neutrino energy assignment using the energy-radius correlation of the beam is not used, because it produces wrong results for the wide-band background events. This cut is only possible for CC events; the total energy is not accessible in NC events. The wide-band background is reduced by a factor four, while less than 10% of the wanted events are lost. No shower energy cut was applied.

TABLE 8
Corrected event numbers and total cross-sections.

Beam	Energy	Corrected event numbers	Cross-sections $10^{-38}cm^2 \cdot E$ [GeV·nucl.]$^{-1}$
Neutrino	30-90	3383.2 ± 71	0.625 ± 0.040
	90-200	3074.5 ± 68	0.578 ± 0.040
Antineutrino	30-90	2173.2 ± 58	0.303 ± 0.018
	90-200	684.8 ± 38	0.275 ± 0.025

The total number of events after corrections, together with the cross-sections obtained for different parts of the energy spectrum, are given in table 8. The errors are larger than the errors in the total cross-sections obtained for the full energy spectrum due to the following sources:

1. The uncertainty in the K/π ratio enters directly in the higher part of the spectrum (3%).

2. The uncertainty in the tails of the resolution functions enters. This contributes a 2.5% error to the low-energy part. The uncertainty in

the migration of events from the lower to the higher part and vice-versa contributes a 1% uncertainty, except for the high-energy part of the antineutrino spectrum, where a 3.5% uncertainty is induced. This large effect is due to the asymmetric population of high-energy and low-energy events in this exposure.

3. The statistics is reduced. This contributes a 2% uncertainty (4% for the high-energy part of the antineutrinos).

The ratios of the cross-section slopes σ/E can be compared with predictions from scaling and QCD calculations. This comparison is shown in table 9. In the absence of a quasi-elastic contribution, the scaling prediction would give 1 for this ratio. The QCD calculations are based on the model of the structure functions, described in section 1.1.4 and 1.4.3. An ad hoc contribution of quasi-elastic events was used in both predictions with a constant cross-section [68]

$$\sigma_{qe} = 0.5 \cdot 10^{-38} \text{ cm}^2 \text{ nucleon}^{-1}$$

Effects of the W-propagator can be neglected in this energy range. The uncertainties in the measurements are too large to be sensitive to the small differences in the predictions. The results are consistent with both hypotheses.

TABLE 9
Ratios of total cross-sections for two energy regions.

	neutrinos	antineutrinos
This measurement	0.93 ± 0.06	0.91 ± 0.07
Scaling prediction	0.99	0.97
QCD prediction	0.95	0.97

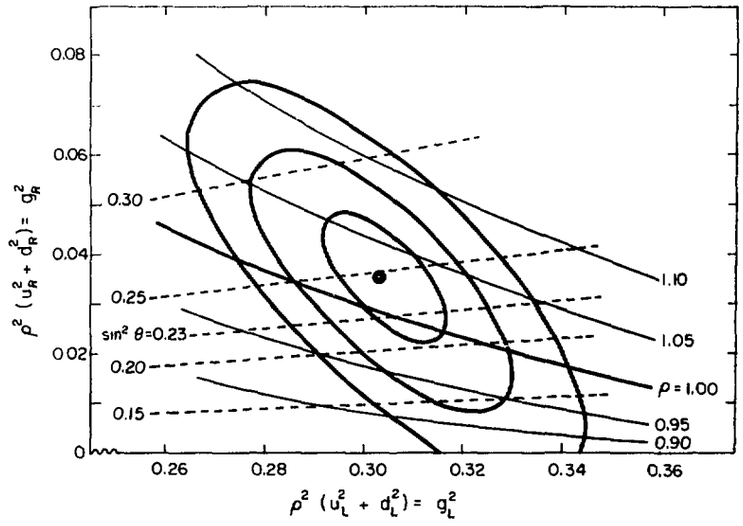

Figure 33: Best fit and confidence limits of 39%, 87%, and 99% on the chiral coupling constants as determined in this experiment. The drawn curves are lines of constant ρ, and the dashed curves are lines of constant $\sin^2\theta$.

5.1.5 Coupling constants

From the measured cross-section ratios, we obtain the chiral coupling constants or, equivalently, the relative strength of the NC to CC coupling ρ and the electroweak mixing angle $\sin^2\theta$. We first analyse the results within the framework of an SU(2) x U(1) gauge theory, in which no specific value of the parameter ρ is assumed.

We find from equations (3) and (4) the following values of the left-handed and right-handed coupling constants after correction for the strange and charmed sea, the non-zero Cabibbo angle, and the shower energy cut:

$$g_l^2 = \rho^2(u_l^2 + d_l^2) = 0.305 \pm 0.013 \qquad (44)$$

$$g_r^2 = \rho^2(u_r^2 + d_r^2) = 0.036 \pm 0.013 \qquad (45)$$

We thus obtain a non-zero value of the right-handed coupling with more than 90% confidence (see fig.33) without constraining the value of ρ. Therefore, this measurement of the right-handed coupling is independent of the Glashow-Salam-Weinberg model. Values of these coupling constants obtained by other experiments [61,62] are given in table 10; the values corrected for the different energy cuts and the contribution of strange quarks are taken from [69].

TABLE 10
Comparison of results on chiral coupling constants.

	CHARM	CDHS	BEBC
g_l^2	0.305 ± 0.013	0.292 ± 0.013	0.313 ± 0.034
g_r^2	0.036 ± 0.013	0.034 ± 0.017	0.023 ± 0.025

This result can also be expressed in terms of the parameters ρ and $\sin^2\theta$. From equations (7) and (8) and the measurement of the coupling constants (equations (44) and (45)) follows:

$$\rho = 1.027 \pm 0.023 \qquad (46)$$

$$\sin^2\theta = 0.247 \pm 0.038 \qquad (47)$$

In the framework of the Glashow-Salam-Weinberg model, NC and CC coupling have equal strength, $\rho = 1$. To obtain the electroweak mixing angle in the context of this model, we have made use of an equation proposed by Paschos and Wolfenstein [24] (see equation (2) in section 1.1.4):

$$\frac{\sigma(\nu\to\nu) - \sigma(\bar{\nu}\to\bar{\nu})}{\sigma(\nu\to\mu^-) - \sigma(\bar{\nu}\to\mu^+)} = \rho^2(1/2 - \sin^2\theta) \qquad (48)$$

Assuming $\rho = 1$ and inserting event numbers and the ratio of neutrino and antineutrino fluxes, we find for a 2 GeV shower energy cut,

$$\sin^2\theta = 0.230 \pm 0.023 \qquad (49)$$

Relation (48) holds only if the structure functions and their scaling violations in neutrino and antineutrino interactions are equal, if the charmed sea is negligible and if the neutrino and antineutrino energy spectra are equal. The dominant corrections to equation (48) involve the threshold behaviour of charmed quark production, due to the different spectra of the neutrino and antineutrino beam (see also section 1.1.4). We estimate an additional systematic error of ±0.008 due to these effects, in agreement with the calculations

of Paschos [25]. Experimentally, the influence of these effects can be estimated qualitatively by varying the shower energy cut. Inserting the event numbers obtained with a 25 GeV shower energy cut, we find

$$\sin^2\theta = 0.224 \pm 0.025$$

in agreement with the result for the lower cut.

The systematic error in the results given in eqs. (44), (45), (46), (47), and (49) is composed of approximately equal contributions from the uncertainties in the various corrections applied to the raw data sample and from the uncertainties in the neutrino flux monitoring.

The measurements of R and $\bar{R}$ alone can also be used to determine $\sin^2\theta$ in a model-dependent analysis. We have used a recent QCD model calculation by Kim et al. [23], as described in section 1.1.4. They use a model based on the parametrization of the structure functions of Buras and Gaemers [22] (see section 1.4.3). Taking the beam spectra and selection criteria of the present experiment into account, we deduce a value of the electroweak mixing angle of the Glashow-Salam-Weinberg model corresponding to

$$\sin^2\theta = 0.220 \pm 0.014 \qquad (50)$$

Kim et al. [23] estimate an additional error of 0.009 on this value because of uncertainties in the model calculation. In fig.34 we compare these results with previous measurements; the result of the model calculation is shown for different values of $\sin^2\theta$. The measurement of R determines the electroweak mixing angle, while the measurement of $\bar{R}$ serves as a consistency check of the model.

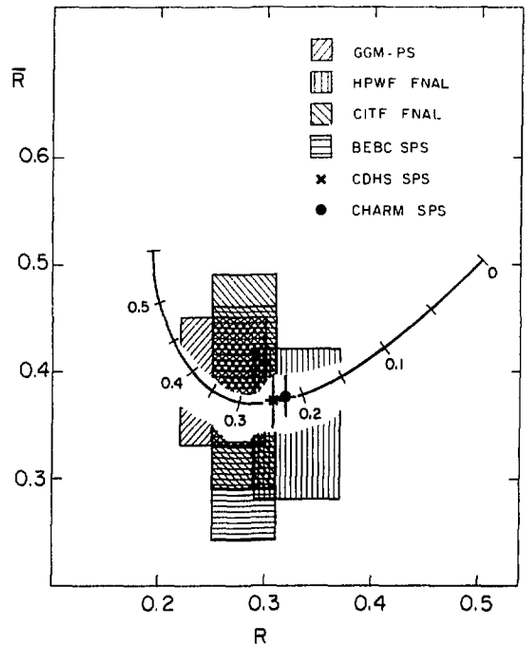

Figure 34: Comparison of the results of various experiments on R and $\bar{R}$ with the Glashow-Salam-Weinberg model. The rectangles indicate the $\pm 1\sigma$ limits. The data are taken with different cuts in shower energy (the cuts being 0 GeV, 4 GeV, 12 GeV, 15 GeV, and 10 GeV for experiments GGM [58], HPWF [59], CITF [60], BEBC [61], and CDHS [62], respectively. Our data have a cut of 2 GeV. The curve is obtained for our conditions following the model calculations of ref.[23], for different values of $\sin^2\theta$.

The model-dependence of the measurement of $\sin^2\theta$ (equation (49)) using the Paschos-Wolfenstein relation is due to the experimental problem of unequal beam spectra, whereas the result quoted in equation (50) is obtained by an explicit use of model calculations, and hence the model-dependence is inherent in this method. However, the model-dependent uncertainties in the two results turn out to be nearly equal. Because the experimental uncertainties are larger in the result quoted in equation (49), we prefer to quote the more precise result of equation (50) based on the model-dependent analysis:
$\sin^2\theta = 0.220 \pm 0.014$.

The measurement of $\sin^2\theta$ in this experiment is in good agreement with the value $\sin^2\theta = 0.224 \pm 0.020$ obtained with measurements of parity violating asymmetries in the inelastic scattering of longitudinally polarized electrons from deuterium [70].

The measurement of $\sin^2\theta$ can be compared with predictions made in the context of grand unified theories. The result of a calculation of Marciano and Sirlin [71] for an SU(5) theory, obtained for neutrino scattering off nucleons around $Q^2 = 20$ GeV^2 is

$$\sin^2\theta = 0.2098 + 0.004\cdot(N_h-1) + 0.006\cdot\log(0.4\ \text{GeV}/\Lambda(\overline{\text{MS}}))$$

where N_h is the number of Higgs doublets in the theory and $\Lambda(\overline{\text{MS}})$ is the free mass-scale parameter of QCD valid for a particular renormalization scheme (more details can be found in ref.[71]). For the presently accepted values of the free parameters, $\Lambda(\overline{\text{MS}}) \simeq 0.4$ GeV and $N_h = 1$, the SU(5) prediction is in good agreement with the measurements.

5.2 DIFFERENTIAL CROSS-SECTIONS OF CHARGED-CURRENT INTERACTIONS

The differential cross-sections $d\sigma/dy$ and $d\sigma/dx$ were obtained for neutrino and antineutrino charged-current interactions. The data were recorded during a 200 GeV/c narrow-band beam exposure. The momentum of the extracted proton beam was 400 GeV/c for the largest fraction of the exposure. Also data taken with a 450 GeV/c extracted proton beam were used. The analysis is based on 6317 neutrino and 4294 antineutrino charged-current events satisfying all selection criteria. The selection criteria used for this analysis are identical to those described in section 5.1.4.

5.2.1 The interpretation of measured distributions

Experimental distributions, obtained by a measurement with finite resolutions, can not be interpreted without knowledge of the measurement resolution. In addition, cuts applied in the analysis have to be taken into account. Resolution effects can be taken out in different ways:

1. The measured distributions are untouched, and compared with a theoretical prediction of the same distribution. To make the comparison meaningful, one has to include all resolution effects and cuts in the prediction. This method is useful if one wants to reject or accept a definite theory, or to measure a parameter in a theory. It has the disadvantage that no corrected distribution can be shown.

2. A different approach is to correct the measured distributions for resolution effects and cuts. The advantage of this method is that the physical distributions are obtained. Furthermore, one can make a check whether the physical distribution obtained in the procedure gives a good description of the data. This check is done comparing the measured raw distribution with the simulated distribution obtained by mod-

ifying the physical distribution obtained in the procedure, according to the experimental resolution and acceptance. This method will be described below.

5.2.2 The unfolding procedure

The adopted unfolding procedure is developed in order to find a physical distribution in the most model-independent way. The problem it solves can be stated as follows:

> Find that distribution, which, when transformed according to the resolutions, gives the best description of the measured distribution of events.

The measured variable accumulated in the frequency distribution of measurements is defined to give optimum sensitivity of the measurement. The choice depends on the resolution functions of the experiment. Usually one can define a measured variable, which is the best estimate of the physical variable. However, the method is more general and also the space of measured variables can have a different dimension than the space of physical variables.

Let the measured variable be z_m, its frequency distribution $g(z_m)$, the physical variable z and its physical distribution $f(z)$. The resolution functions are known and are given by the distribution function $r(z,z_m)$, which gives for an event with the physical property z the probability to yield the measured value z_m. For a measurement with infinitely small uncertainties the smearing distribution function reduces to:

$$r(z,z_m) = \delta(z-z_m)$$

Acceptance effects and kinematical cuts are incorporated in this function r. Due to these effects the measured number of events can be smaller than the number of interactions with the property z. The acceptance can be written in terms of r:

$$A(z) = \int r(z,z_m)dz_m \leq 1$$

In this way, the acceptance corrections do not need a model for the physical distribution in the variable z. The distribution function $r(z,z_m)$ describing the experimental resolution and acceptance is obtained by integration of the detector response over all kinematic variables except z, and over all geometrical variables. In practice, this integration is performed by a Monte Carlo simulation of events, which will be described in the following section.

In general, the measured distribution is given as a histogram; we define:

$$G_i = \int_{x_i}^{x_{i+1}} g(z_m)dz_m$$

as the content of the i^{th} bin in the histogram. With these definitions, we can write down the integral equation which has to be solved in the unfolding procedure:

$$G_i = \int_{x_i}^{x_{i+1}} dz_m \int dz\ f(z)\cdot r(z,z_m) \qquad ;\ i = 1,k$$

where the integration interval of the inner integral is the whole physical range of z. This equation can be solved with the ansatz

$$f(z) = \Sigma_j \cdot a_j\ \beta_j(z) \qquad ;\ j = 1,n \qquad (51)$$

where $\beta_j(z)$ are n arbitrary fixed functions of z, and a_j are the coefficients to be measured. The simplest choice for $\beta_j(z)$ are histogram bins:

$$\beta_i(z) = 1 \quad \text{for } z_i \leq z < z_{i+1}$$
$$\beta_i(z) = 0 \quad \text{outside the interval.}$$

With this choice, the estimate of f(z) will be in general a discontinuous function. Better choices for the functions β_j can be made, which yield a continuous function as a result. With a chosen set of functions β_j, the integral equation takes the form

$$G_i = \int_{x_i}^{x_{i+1}} dz_m \, \Sigma_j \, a_j \int dz \, \beta_j(z) \cdot r(z, z_m)$$

Apart from the coefficients, the right-hand side contains only known functions. With the notation

$$H_{i,j} = \int_{x_i}^{x_{i+1}} dz_m \int dz \, \beta_j(z) \cdot r(z, z_m)$$

one obtaines the system of k equations with n unknowns a_i

$$G_i = \Sigma_j \, a_j \, H_{i,j} \qquad ; \; i = 1,k \; ; \; j = 1,n \qquad (52)$$

which has a unique solution for n = k. For the case k > n the unknowns a_j can be estimated by a least-squares fit. When the coefficients a_j are found, the unfolded physical distribution is given by equation (51). Of course, the choice of the functions β_j is arbitrary, and is a critical step in the procedure.

For the purpose of presentation, histograms can be obtained by integrating the function f(z) over intervals of z. The covariance matrix of the histogram bin contents can be found by a straightforward error propagation of the covariance matrix of the coefficients a_j.

As a consequence of the finite resolutions, the coefficients a_j have usually non-vanishing negative correlation coefficients. The contents of the histogram bins (the integrals over f(z)) can have a mixture of negative and positive correlation coefficients. These correlations have to be taken into account when e.g. fits are made to the data points. With an optimal choice of the bin size compared to the experimental resolution, the positive correlations introduced by the integration over the bins can be made to cancel approximately the negative correlations inherent in the unfolding procedure. This was achieved e.g. in the unfolding of the experimental y-distributions by choosing the bin width roughly twice the size of the resolution.

In our analysis we have used B-splines [72] for the functions β_j. In fig.35 an example is given of cubic B-splines with equidistant knots x_j (a) and quartic B-splines with non-equidistant knots (b). The most important properties of cubic B-splines are:

1. They are third order polynomials in the intervals $x_i < x < x_{i+1}$.

2. They are continuous over the interval where they are defined.

3. The first and second derivatives are continuous over the interval.

4. The third derivatives are in general discontinuous at the knots x_i.

Quartic B-splines are fourth order polynomials of which the first, second and third derivatives are continuous and of which the fifth derivatives may be

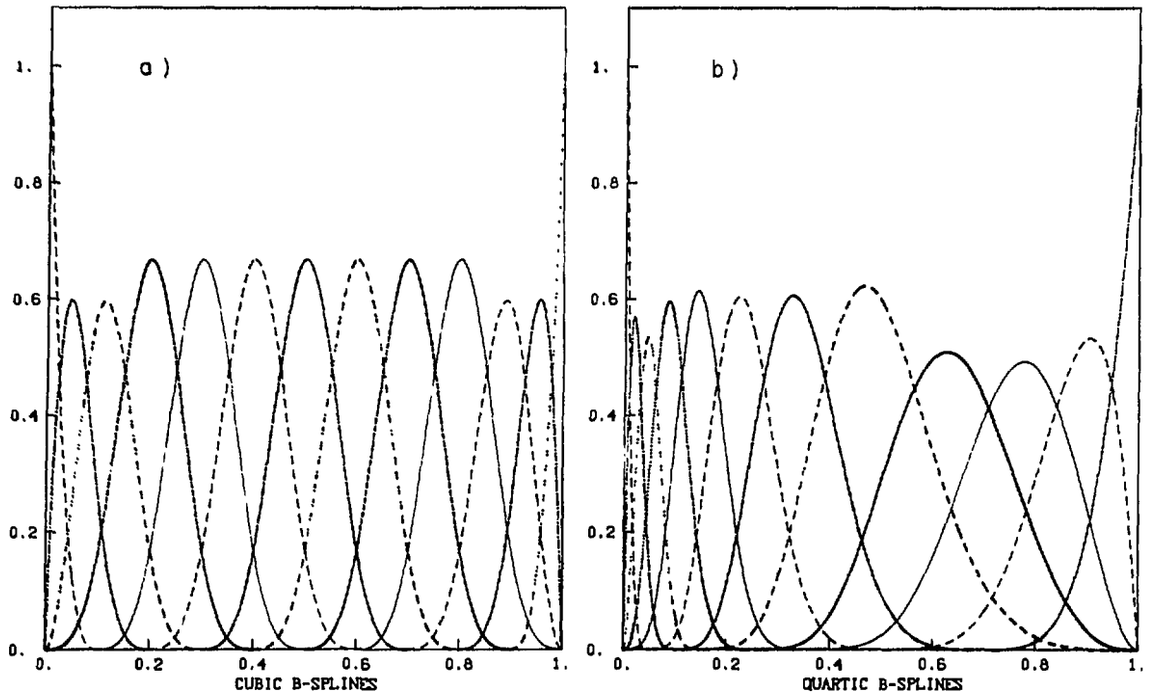

Figure 35: Cubic B-splines with equidistant knots (a) and quartic B-splines with non-equidistant knots (b).

discontinuous at the knots. With this choice of the functions no physical assumption is made other than that the physical distribution varies smoothly over an interval comparable to the knot distance.

5.2.3 Monte Carlo simulation of events

The acceptance and resolution corrections applied to the experimental data were obtained using a Monte Carlo method. On the one hand, the simulation was used in order to obtain the distribution functions $r(z,z_m)$ for the unfolding of measured distributions, as described in the previous section. On the other hand, distributions smeared by experimental resolutions and acceptance were generated for the comparison of theoretical predictions with the measurements. The latter method was used in the fits to the y-distributions described in a following section. The integration over the kinematic variables is performed simulating the performance of the detector and the pattern recognition on the basis of single events.

The first step in the simulation program is the generation of the kinematic variables of the events. One necessary input is the beam spectrum and the energy-radius correlation of the neutrino flux. The different angles of the incoming neutrinos at different radii and the spread in the angles were taken into account. The magnitude of this effect is of the order of the muon angular resolution.

The other input is the model assumed for the differential cross-sections, necessary as a weight function in the integration over the resolution and acceptance. In the unfolding method no assumption is necessary about the differential cross-section dependence in the variable to be measured. However, a model of the dependence on orthogonal variables has to be assumed, when the unfolding is performed in one dimension. This can be explained with the following example.

For the unfolding of the y-distribution one has to know the resolution function for the measurement of the y-variable. This is ob-

tained by integrating the double differential cross-section $d^2\sigma/dxdy$ at a fixed y over x, and over the beam spectrum and the interaction radius in the detector. The spectrum and the radial dependence of the neutrino beam are calculable. However, for the integration over x one needs a model of the x-distributions at fixed values of y. This model-dependence is removed when one does the unfolding in x and y (or in x and Q^2) simultaneously. Then, one integrates only over the known beam properties.

The model-dependence introduces some unavoidable arbitrariness in the results of one dimensional distributions. The influence of the choice of the model was tested in the individual cases by varying the assumptions within reasonable limits.

The kinematics of an event are fixed by three variables only, say the scaling variables x and y and the neutrino energy E. From these variables and the interaction vertex all kinematic variables can be generated. When Fermi-motion is neglected these quantities, the "true" variables, follow directly. However, due to Fermi-motion effects the kinematic variables follow only when the four-momentum of the nucleon is known in addition. The analysis is done with and without these corrections for Fermi-motion separately. Details are described in the following section.

The second step is the resolution smearing of the generated kinematic variables of the event. Simultaneously the selection criteria for muons are simulated. In order to be able to use the resolution functions for the muon momentum and the angle, muons are tracked through the geometry of the detector. The visible path length in the marble region outside the shower, and the path length in the magnetized iron is calculated. The number of points measured on the track in the various regions are simulated, taking the efficiencies into account. From these numbers the resolutions can be simulated and the muon selection criteria applied. The shower resolutions are defined as global parametrizations. The event vertex measurement is simulated using the muon angular resolution and multiple scattering together with the shower vertex resolution.

The simulated measurements are then passed through the same kinematical fit as the recorded data events described is section 4.3. Like for real data events the measured neutrino energy is assigned from the energy-radius correlation of the beam spectrum. Fiducial cuts are applied on the smeared variables.

5.2.4 Fermi-motion corrections

The aim of the Fermi-motion corrections applied to the data is to obtain a measurement of neutrino interactions on nucleons in their rest frame. Nucleons of elements other than hydrogen are not at rest in the laboratory system due to nuclear binding effects (Fermi-motion). These effects are only negligible if the kinetic energy of the nucleons is small compared to their mass, independent of the incident neutrino energy. The influence of the Fermi-motion corrections on the final results of the analysis was checked for all results by performing the analysis with and without these corrections. The distribution of the kinetic energy of nucleons was calculated using an average potential of nuclei in the marble target, to which was added a 25% contribution of tails due to short-range forces obtained from the deuteron wavefunction [73]. Indications of short-range nucleon-nucleon correlations were observed in electron-nucleus scattering experiments [74]. The energy distribution is shown in fig.36.

The actual four-vector of the struck nucleon is generated randomly according to this energy-distribution; the direction is generated isotropically in the laboratory system. Both the neutrino four-vector and the nucleon four-vector are now Lorentz-transformed to the rest system of the nucleon; the

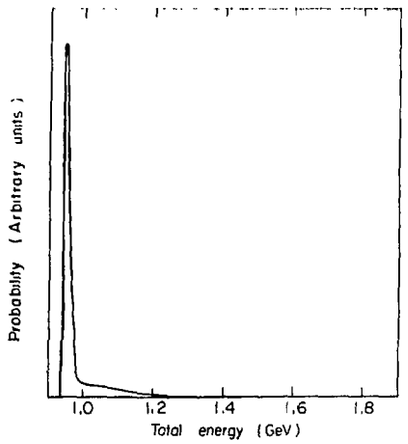

Figure 36: Total energy distribution of nucleons in the target used in the calculations of the Fermi-motion corrections.

transformation yields trivially zero for the value of the nucleon momentum. The scaling variables are then defined in the nucleon rest system. Together with the transformed neutrino energy this is sufficient to calculate the four-vectors of the muon and the hadronic system. The four-vectors are transformed back to the laboratory frame. The resulting four-vectors are used as starting point of the same resolution smearing and acceptance simulation. In this way one obtains simulations of measured distributions originating from a set (x,y,E) defined in the nucleon rest frame.

5.2.5 Radiative corrections

The measured differential cross-section differs from the "bare" neutrino nucleon cross-section due to the radiation of photons by the outgoing muon. We have used the prescription given by de Rujula et al. [75]. The diagrams contributing to the effect in the leading order approximation are shown in fig.37, together with the diagram corresponding to the "bare" cross-section.

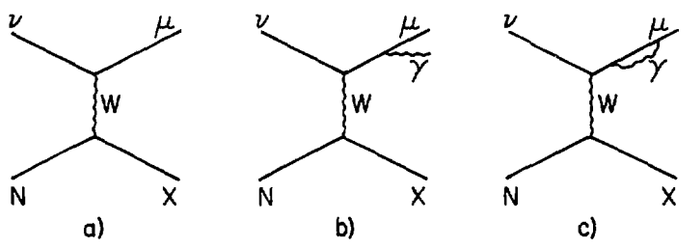

Figure 37: Bare cross-section (a) and diagrams involving real photon emission (b) and virtual photon emission (c) by the muon.

In this approximation only the emission and eventual reabsorption of collinear photons was considered (peaking approximation). The emitted photons cause the measured muon energy to be less than the energy at the primary vertex; the angle is not changed in this approximation. The energy of the photon is sampled as a part of the hadronic energy.

The equation for the measured cross-section, σ_0, in terms of the bare cross-section, σ_b, is written in its most transparent form in terms of the muon energy and space angle:

$$\frac{d^2\sigma_0}{dE_\mu d\Omega} = \frac{d^2\sigma_b}{dE_\mu d\Omega} + \frac{\alpha}{2\pi}\cdot\log\left[\frac{4E_\mu^{*2}}{\mu^2}\right]\cdot\int_0^1 dz\frac{1+z^2}{1-z}\cdot\left[\frac{1}{z}\cdot\frac{d^2\sigma_b}{d\tilde{E}_\mu d\Omega}\right|_{\tilde{E}_\mu=E_\mu/z}$$

$$\cdot\theta(z-z_{min}) - \frac{d^2\sigma_b}{dE_\mu d\Omega}\Bigg] + O\left[\frac{\alpha}{2\pi}\right]$$

with

$$4E_\mu^{*2} = 2ME(1-y+xy)^2$$

$$z_{min} = \frac{E_\mu}{E}\cdot\left[1 + \frac{E}{M}(1-\cos\theta)\right] = 1-y+xy$$

The first term of the integrand corresponds to real photon emission (changing the muon energy), the second term to virtual photon emission and reabsorption (not changing the muon energy). According to de Rujula et al. [75] this equation is expected to be a good approximation, to ≈10% of the effect, everywhere except at very large y.

The equation involves the input of a known bare cross-section. With a guess of this bare cross-section the ratio of the observed differential cross-section and the bare cross-section can be computed. This ratio depends on x, y and E. The correction is incorporated in the unfolding procedure.

The Monte Carlo events generated for the integration of the resolution and the acceptance are weighted in the integration with the correction factor to obtain a radiatively distorted simulated event distribution. Thus predicted smeared distributions are obtained, corresponding to a bare cross-section for a value of the physical variable. In this way the measured distributions, which are distorted by radiative effects, are compared with radiatively distorted simulated distributions.

In this procedure the migration of events is approximated by a multiplication with correction factors. The magnitude of the effect, typically smaller than 10%, ensures that this is a good approximation when a reasonable choice of the bare cross-section is made. This can be checked comparing the assumed model with the result of the analysis. We have applied corrections only for radiation of photons by the muon. Other effects involving the interference of radiation by the hadrons and the muon are expected to be much smaller and are neglected. The radiation of photons by hadrons need not be corrected for, because the hadronic system is measured inclusively in this experiment.

5.2.6 Subtraction of backgrounds from differential distributions

The following backgrounds were subtracted from the differential distributions of charged-current events.

1. Wide-band background. The energy-spectrum and event-numbers were obtained using closed-collimator runs. The ratio of neutrino induced events to antineutrino induced events was measured using the sign of the muon charge, given by the magnetic deflection.

2. π and K decay in showers of NC events. The characteristics of this background were measured in dimuon events. The probability to observe a decay muon in an NC event faking a CC event was shown to be proportional to the shower energy. Also the angular distribution was obtained.

Distributions were generated with a simulation program for both types of background and normalized to the correct number of events. Resolution effects were taken into account in the simulation of these events. A model of the differential cross-sections was necessary.

3. The subtraction of interactions of neutrinos from other decays of the kaon than the decay into a muon and a neutrino was incorporated in the unfolding procedure. Only the energy spectrum and the total number of these events had to be known a priori. The details of the differential cross-sections of their interaction followed automatically from the unfolding procedure, with the assumption that they were identical to those of the non-background events.

5.2.7 The y-distribution of charged-current interactions

Resolution and acceptance

In charged-current interactions the inelasticity, y, is defined by the measurement of the shower energy and the energy of the muon, $y = E_h/(E_h+E_\mu)$. The estimate of y can be improved by adding in the kinematical fit (described in section 4.3) the constraints of transverse momentum balance provided by the measurement of the shower and muon angles. Also the energy of the neutrino, E, can be infered from the radial position of the interaction in the detector and the beam spectrum, thus adding a further constraint in the kinematical fit by the requirement of energy balance ($E_h + E_\mu = E$).

The resolution in y obtained with the kinematical fit mentioned before is shown in fig.38 for different parts of the neutrino energy spectrum. The resolution improves with increasing energy, no large x-dependence is observed. The resolution is calculated with the simulation program for all events satisfying the cuts.

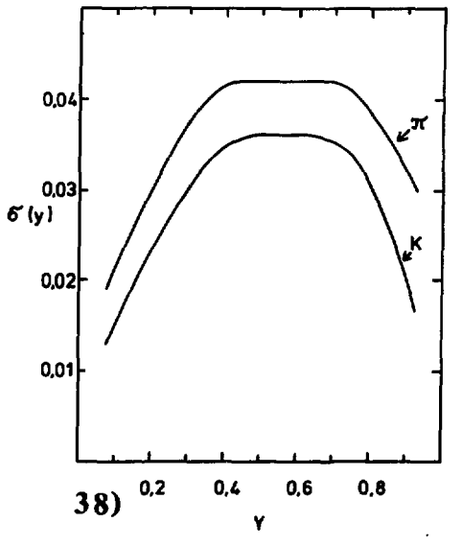

38)

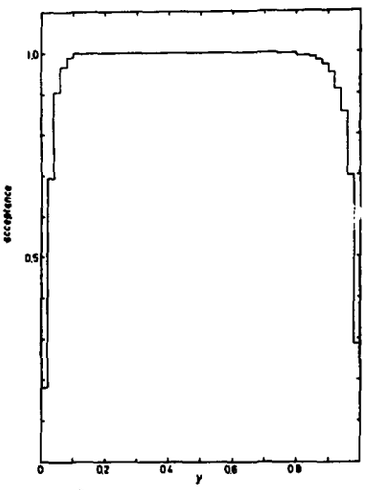

39)

Figure 38: Resolution of the measurement of y as a function of y for the two components of the neutrino spectrum.

Figure 39: Calculated y-dependence of the acceptance for charged-current events. The cut-off towards y = 1 is a consequence of the selection criteria for the recognition of muons. The drop towards y = 0 is due to the 2 GeV shower energy cut.

The acceptance, calculated with the simulation program (section 5.2.3) is shown in fig.39. For values of y between 0.1 and 0.8 the acceptance is essentially 100%. At low y the acceptance drops due to the shower energy cut, at high y due to the selection criteria for the recognition of muons.

The raw y-distributions thus obtained were corrected for backgrounds by subtraction of Monte Carlo generated distributions. The distributions were

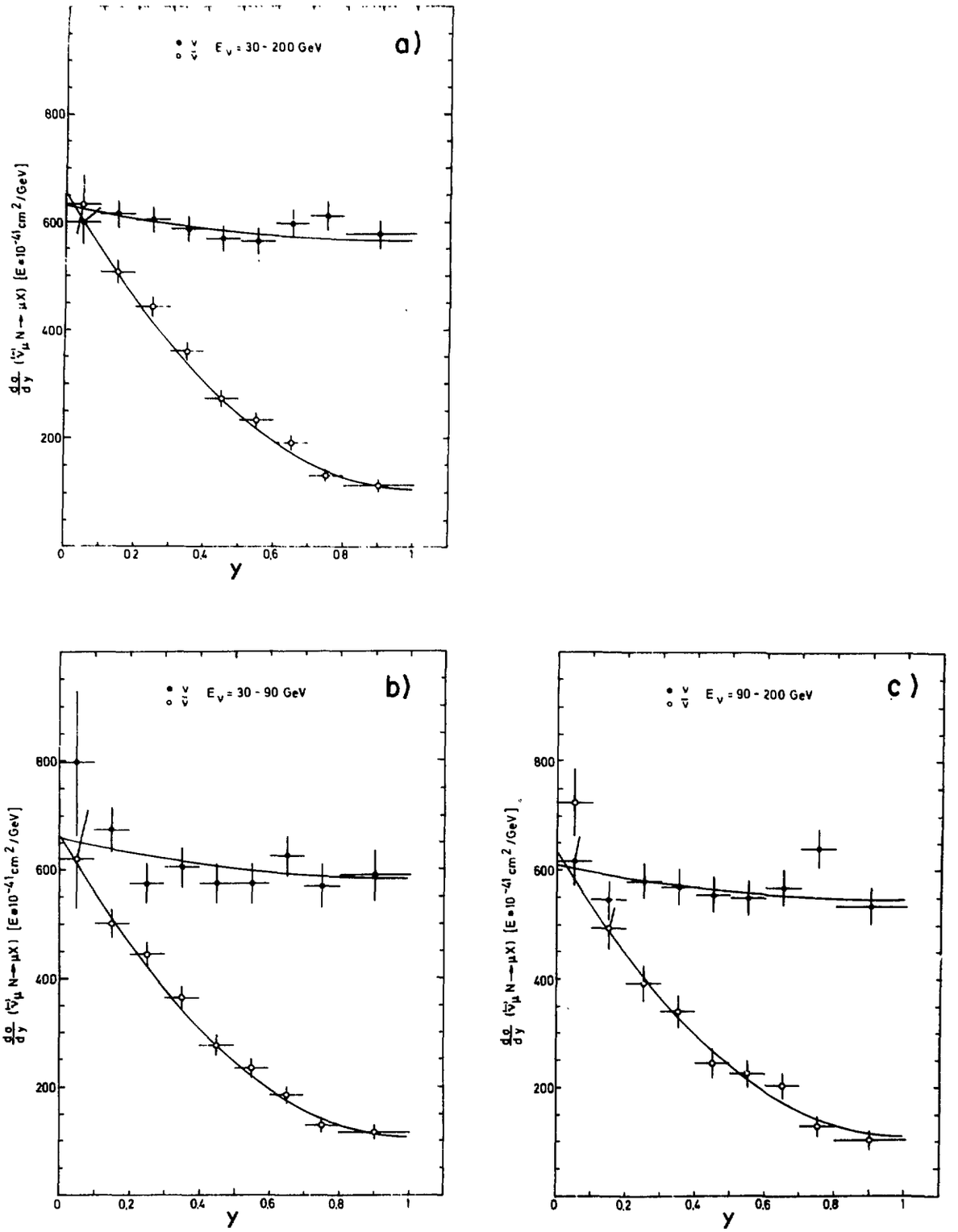

Figure 40: The resolution unfolded, acceptance corrected differential cross-sections dσ/dy for neutrinos and antineutrinos measured for the full energy spectrum (a), and the low (b) and high (c) part of the spectrum. The curves are theoretical predictions for the physical distributions corresponding to fits to the raw distributions (see the text in a following section). The numerical values of the data points are given in Appendix A.

corrected for kinematical cuts and smearing effects due to measurement errors using the unfolding procedure described above.

Corrections

The data were corrected for radiative effects. Due to their limited expected influence, no Fermi-motion corrections were applied to the y-distributions as a standard procedure. However, where appropriate the results with these corrections included will be mentioned. In addition, the effect of the radiative corrections will be shown by a comparison with results from uncorrected data.

A set of cubic B-spline functions was used with equidistant knots, providing ten intervals of width 0.10. The use of these functions corresponds to the implicit assumption that the y-distributions vary smoothly over the knot-distance.

Measured distributions

The corrected, resolution unfolded y-distributions obtained for the full energy spectrum and the parts corresponding to kaon and pion decays are shown separately in fig.40.

The last two bins are averaged, because the acceptance corrections play an important role in the last bin of the y-distributions. Hence the results depend on the details of the simulation program for y larger than ≈0.9.

In principle, the measurement uncertainties follow from the full covariance matrix. However, due to the matching of the bin width and the resolution, the negative correlations necessarily introduced by the unfolding are cancelled approximately by the positive correlations introduced by the use of B-splines. Hence the vertical error bars shown in the figure, corresponding to the diagonal elements of the covariance matrix are a meaningful measure of the uncertainties. The horizontal bars merely indicate the bin sizes.

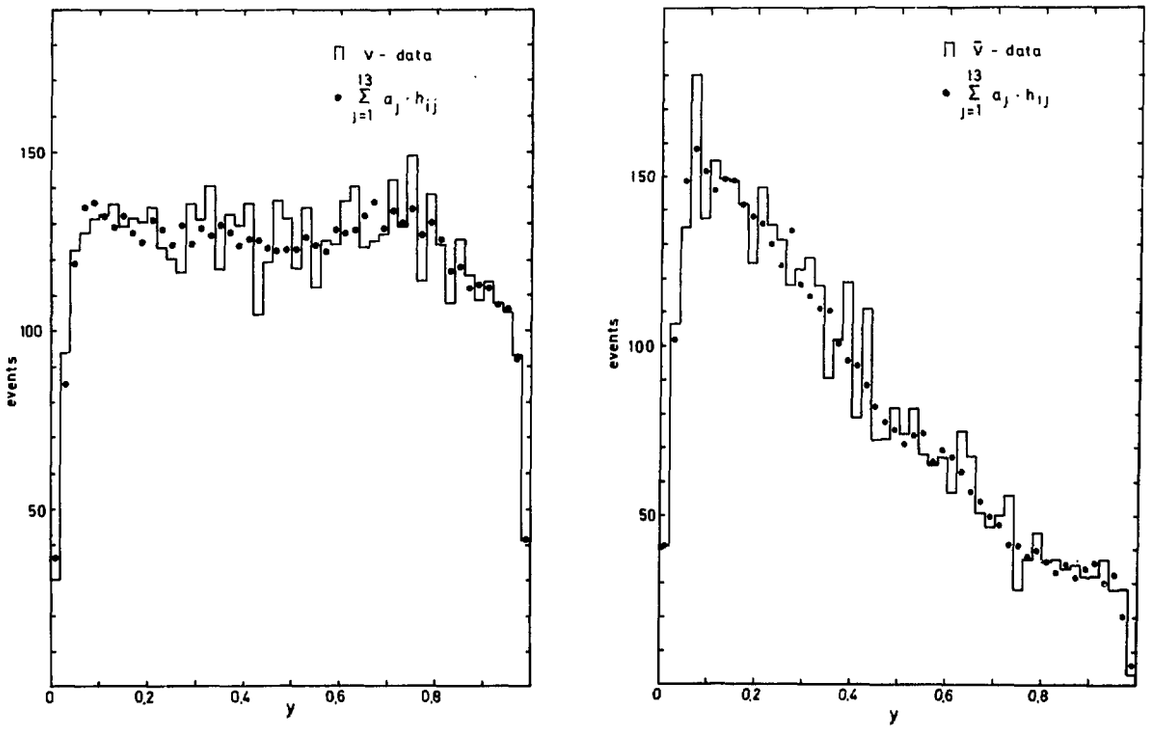

Figure 41: Comparison of the raw y-distribution (histogram) with the simulation based on the measured differential cross-sections (full dots).

As a check of the procedure, the y-distributions obtained in the unfolding were smeared with the experimental resolution, and acceptance cuts were applied. The smeared y-distributions thus obtained can be compared with the measured, raw y-distributions from which backgrounds were subtracted. The comparison is shown in fig.41. As can be seen, the simulated distribution fits the data well.

Fits to the y-distributions

The simple form of the theoretical prediction enables one to extract the parameters from the raw distributions in a transparent way. In these fits not the resolution unfolded distributions are used, but the directly measured, raw distributions. Backgrounds were not subtracted from the raw distributions, but considered as a separate term in the fit. The measured y-distributions were separated into two parts, corresponding to kaon and pion decays. These two parts were compared separately with a linear superposition of simulated histograms. These histograms were obtained by simulating the detector response to physical input distributions, which were integrated over the two parts of the beam spectrum. The theoretically predicted y-distribution can be obtained from a linear superposition of the various physical input distributions, the coefficients of the input distributions being free parameters in the fit. The theoretical formalism was already given in sections 1.3.4, 1.3.5, and 1.3.9. The terms considered in the various fits to the raw distributions are the histograms corresponding to

1. a constant term;
2. a term proportional to $(1-y)^2$;
3. a term proportional to y^2;
4. the wide-band background;
5. NC events with a decay muon faking a CC event.

These histograms are calculated for the part of the beam spectrum corresponding to kaon and pion decays separately for both the neutrino and antineutrino distributions. The effects of resolutions and experimental cuts are simulated by a Monte Carlo integration (see section 5.2.3).

In this method the uncertainties of the relative normalizations of the neutrino and antineutrino flux and of the K/π ratios can be taken into account rigorously. Also the uncertainties in the absolute scale of the background subtractions, giving rise to a bin-to-bin correlation of the background histograms can be treated correctly. Three different types of fits attempted with this procedure will be discussed below.

Shape parameters of the y-distributions

With the assumption that the Callan-Gross relation is valid and the assumption of charge symmetry, the y-distribution is described by equation (26). With the absolute normalization of the fluxes, the neutrino and antineutrino distributions can be fitted simultaneously. The results of this fit can be expressed in terms of the shape parameters, α and $\bar{\alpha}$, as defined in equation (28). The shape parameters, α, measure the contribution of the momentum fraction carried by antiquarks in the nucleon. The difference of these fractions, $\bar{\alpha}-\alpha$, is interpreted as twice the contribution of strange quarks (equation (29)).

The functions corresponding to the best fit are shown in figure 40. The values of the parameters are shown in table 11. The difference of the antineutrino and neutrino shape parameters is given separately because the measurement errors of these two parameters are correlated. The first column gives the results for the analysis including radiative corrections, the re-

sults in the second column are obtained including Fermi-motion corrections in addition, and the third column shows data uncorrected for both effects.

The results in column four are obtained without making use of the knowledge of the beam spectrum in the kinematical fit. Otherwise the analysis was equal for the results in columns one and four. Both types of analysis produce equivalent results, which indicates that the calibration of the muon momentum and the shower energy are consistent with the nominal beam energy.

TABLE 11
Shape parameters of the y-distributions.

	Radiative corrections only	Radiative and Fermi-motion corrections	No radiative no Fermi-motion corrections	Energy not from beam spectrum
a	0.10 ± 0.04	0.11 ± 0.04	0.06 ± 0.06	0.10 ± 0.04
$\bar{a}$	0.16 ± 0.01	0.16 ± 0.01	0.18 ± 0.01	0.17 ± 0.01
$\bar{a}$-a	0.06 ± 0.04	0.05 ± 0.05	0.12 ± 0.08	0.07 ± 0.04

From a and $\bar{a}$ can be concluded that the contribution of antiquarks agrees with the amount indicated by the cross-section ratio of neutrinos and antineutrinos, around 15%. Furthermore, there is room for a contribution of the strange quark, although with a statistical significance of only 1.5 standard deviations.

The inclusion of the Fermi-motion corrections does not produce significant changes to the results. However, the shape parameter of the neutrino y-distribution is changed considerably after radiative corrections.

TABLE 12
Energy-dependence of the shape parameters.

Energy range	30-90 GeV	90-200 GeV
a	0.11 ± 0.04	0.12 ± 0.05
$\bar{a}$	0.16 ± 0.01	0.17 ± 0.02
$\bar{a}$-a	0.05 ± 0.05	0.06 ± 0.05

Separate results of fits to the high-energy part (kaon decays) and low energy part (pion decays) are shown in table 12. The numbers are quoted for the results with radiative corrections, but without Fermi-motion corrections. The influence of Fermi-motion on these results is small. No significant energy-dependence can be observed.

The errors quoted in the tables include statistical and systematic errors. The systematic uncertainties follow naturally from the uncertainties found in the fit; a small systematic uncertainty due to the simulation of the muon acceptance is neglected.

TABLE 13
Comparison with other measurements of shape parameters.

	CHARM	HPWFRO	CDHS	BEBC	CITF
a	0.10 ± 0.04	0.13 ± 0.02	0.15 ± 0.04	0.11 ± 0.03	0.24 + 0.08 - 0.13
$\bar{a}$	0.16 ± 0.01	0.14 ± 0.01	0.15 ± 0.02		

Results on these quantities obtained by other experiments [63,64,65,76] are listed in table 13. The BEBC and CITF groups have not extracted α for neutrinos and antineutrinos separately and report the average value. (The acronym HPWFRO is an abbreviation of the combination Harvard-Pennsylvania-Wisconsin-Fermilab-Rutgers-Ohio.)

Test of the Callan-Gross relation

Violations of the Callan-Gross relation show up in the y-distributions as a y^2 term. The coefficient of this term is expected to be equal for the case of neutrinos and antineutrinos. We have tested the existence of this terms under the assumption of charge symmetry. We find a value for the Callan-Gross violation parameter, R, as defined in equation (14):

$$R = 0.01 \pm 0.11$$

indicating no deviation from the Callan-Gross relation. The influence of Fermi-motion is negligible, while for data not corrected for radiative effects a value of

$$R = 0.10 \pm 0.12$$

is obtained. No significant energy dependence of this value is observed. Previously obtained results from other experiments [64,65,76] are given in table 14. The BEBC and HPWFRO groups give the statistical and systematic error separately; in this case the statistical error is given on the first row and the systematic one below. The BEBC result was not corrected for radiative effects.

TABLE 14
Violations of the Callan-Gross relation.

	CHARM	HPWFRO	CDHS	BEBC
R	0.01 ± 0.11	0.11 ± 0.04 ± 0.03	0.03 ± 0.05	0.15 ± 0.10 ± 0.04

Test of charge symmetry

Charge symmetry was tested comparing the energy-weighted neutrino and antineutrino flux ratio, $\Phi/\bar{\Phi}$, with the ratio of the values of the two y-distributions at y = 0. The value of the functions at y = 0 was obtained from a fit, in which the validity of the Callan-Gross relation was assumed; no y^2 term was permitted. Unlike the fits mentioned before, the function values were not constrained at y = 0 according to the neutrino and antineutrino flux ratios. We find the following result for the double ratio

$$S = \left.\frac{d\sigma(\bar{\nu}\to\mu^+)}{dy}\right|_{y=0} \Big/ \left.\frac{d\sigma(\nu\to\mu^-)}{dy}\right|_{y=0} = 1.06 \pm 0.06$$

compatible with charge symmetry, S = 1. In the QPM one expects S to be a few percent larger than 1 (see also section 1.3.9). The effects of Fermi-motion corrections are negligible. No considerable difference is observed when radiative effects are neglected. No significant energy dependence of S is observed.

In table 15 the results are compared with previously reported measurements [63,64,65].

TABLE 15
Tests of charge symmetry.

	CHARM	CDHS	BEBC	CITF
S	1.06 ± 0.06	1.01 ± 0.07	0.9 ± 0.2	0.98 ± 0.09

5.2.8 The x-distributions of charged-current interactions

Analysis

The x-distributions of CC events were obtained with a procedure similar to the one used for the y-distributions. However, some details were changed due to some characteristic differences of the problems. The main differences are:

1. The resolution varies as a function of x from values around 0.01 at x = 0 to 0.25 at x = 1. The resolution in x is shown in fig.42.

2. The expected population of events over the physical region is peaked towards x = 0.

3. Fermi-motion effects are expected to have a considerable influence on the results.

4. The acceptance is not a strong function of x. Only at high y the acceptance decreases slightly with increasing x.

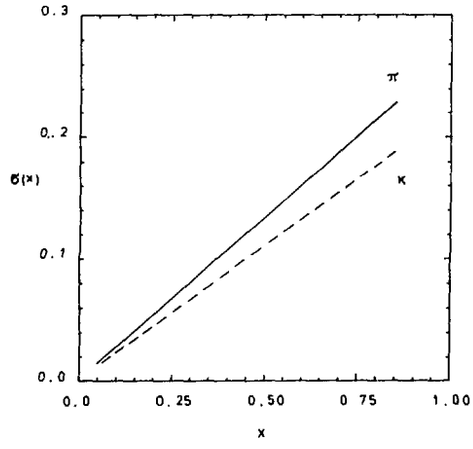

Figure 42: Resolution of the measurement of x as a function of x for the two components of the neutrino spectrum.

Therefore, the following changes were made:

1. In order to exploit the good resolution near x = 0, and to have a more uniform distribution, we used $\sqrt{x}$ rather than x as measured variable.

2. A non-equidistant binning in unfolded x was chosen for the same reasons.

3. Because of the coarse resolution near x = 1, the constraints $f(x=1) = 0$, $f'(x=1) = 0$ and $f''(x=1) = 0$ were imposed on the function, f, in the unfolding. These constraints are justified by the raw x-distributions (fig.43) and by high-energy electron scattering experiments (see e.g. [77]). However, due to these constraints imposed on the re-

sults the last bin $0.7 < x \leq 1.0$ cannot be considered as an independent measurement.

4. In order to accommodate rapid variations of the distributions, quartic rather than cubic splines were used.

5. Corrections for Fermi-motion were incorporated in the standard analysis.

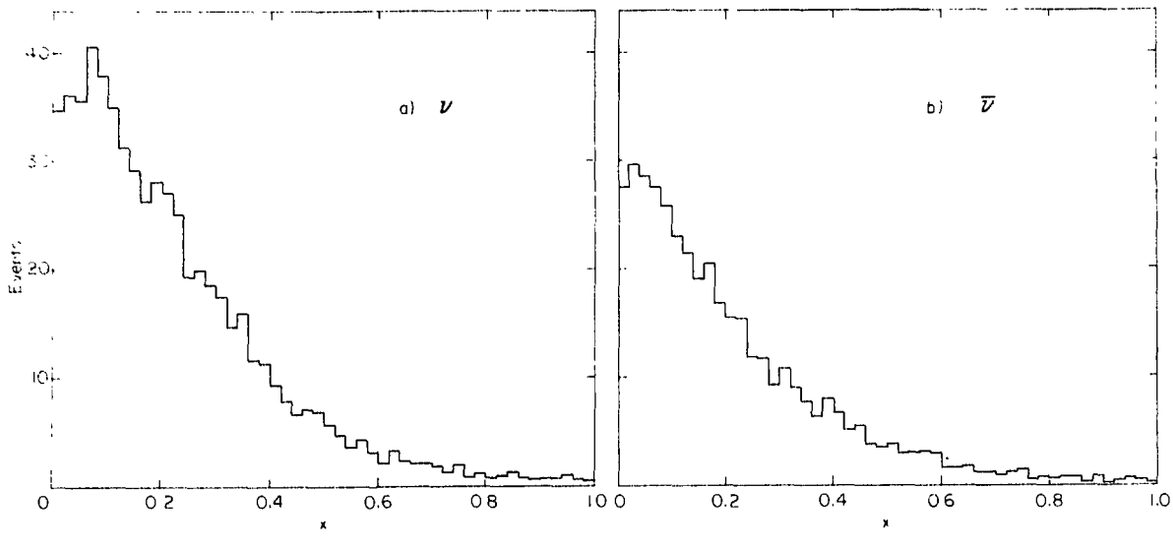

Figure 43: Raw x-distributions for neutrino and antineutrino exposures. Backgrounds were subtracted.

Results

The corrected, resolution unfolded differential cross-sections $d\sigma/dx$ are shown for both neutrino and antineutrino interactions in fig.44. Displayed are the average cross-sections calculated for bins in x. Error bars according to the diagonal elements of the covariance matrix are drawn. The non-diagonal elements are small near $x = 0$, but are significant for $x > 0.15$. The bin-to-bin correlations are negative in this region. No cut in Q^2 was applied in this analysis.

In the presence of scaling violations, i.e. when the structure functions acquire a Q^2-dependence, a quantitative interpretation of these results is difficult. The reason is, that the Q^2 region probed varies as a function of x. The maximum Q^2 reached for a beam with a maximum neutrino energy, E_{max} ($\simeq$200 GeV in this experiment), at a value of x is:

$$Q^2_{max} = 2ME_{max} \cdot x$$

The Q^2 at which a bin in x is measured ranges from 0 to Q^2_{max}. This range is the same for the corresponding x-bins for the neutrino and antineutrino distributions. However, due to the different beam spectra and different y-distributions of neutrinos and antineutrinos, the average Q^2 is different for corresponding x-bins. The average Q^2 as measured in the experiment is given as a function of x for the two beams in fig.45.
From this figure one can read off that the first two x-bins are measured for low Q^2 only: $Q^2 < 1$ GeV^2 essentially. Furthermore, the average Q^2 is considerably different for neutrino and antineutrino exposures.

One can argue that inclusion of low Q^2 data in the results should be avoided. The interpretation of the scaling x variable is not quite clear in the low Q^2 region. For sufficiently high Q^2, the neutrino scatters off almost free quarks. In this domain the quark-parton interpretation of x as the mo-

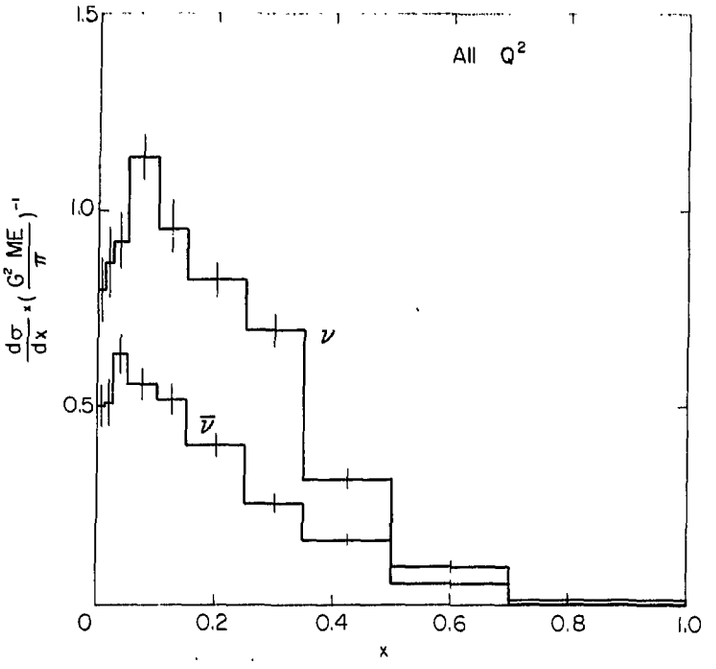

Figure 44: The differential cross-sections $d\sigma/dx$ for neutrinos and antineutrinos obtained for all Q^2. Shown are the averages over the bins.

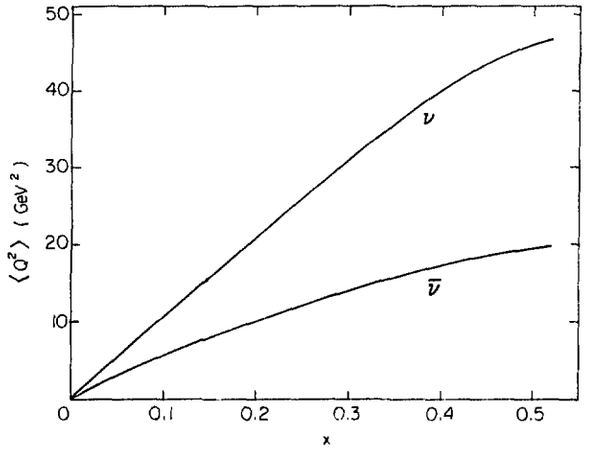

Figure 45: Measured average Q^2 as a function of x for neutrinos and antineutrinos.

mentum fraction of the nucleon carried by the struck quark makes sense. For small Q^2, say smaller than the nucleon mass squared, this interpretation is not applicable and no scaling is expected.

In order to have a qualitative indication of the influence of these effects, different cuts in Q^2 were applied. In fig.46 differential cross-sections are displayed with the cuts, $Q^2 > 0$, $Q^2 > 1$ GeV^2, $Q^2 > 2$ GeV^2 respectively.
The first three bins are taken together in this case, because a cut in Q^2 cuts away the very low x-region. The Q^2 cut is corrected for by extrapolating the measured part of the bin into the unmeasured region, assuming no explicit Q^2-dependence of the cross-section.

When a cut in Q^2 is applied, the neutrino distributions do not change considerably, while it can be observed, that the antineutrino distributions show a rise towards $x = 0$ when a cut in Q^2 is applied.

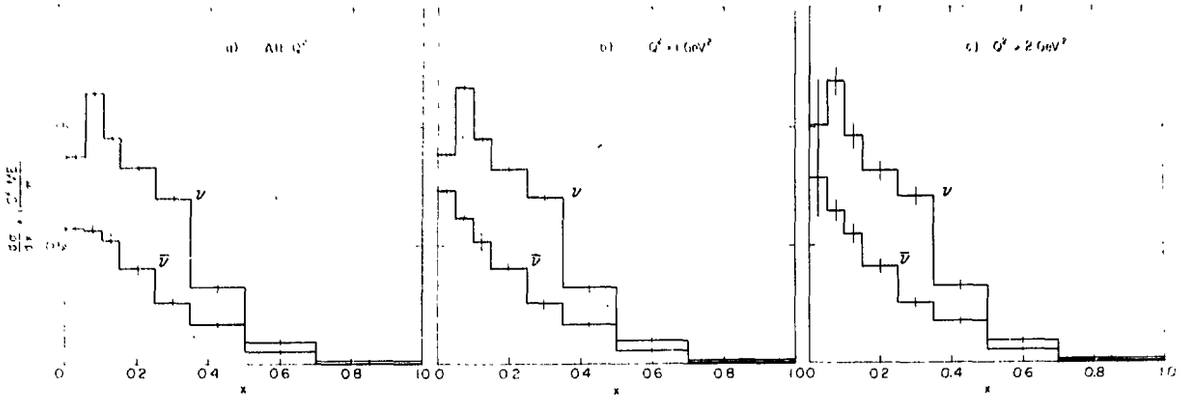

Figure 46: Differential cross-section $d\sigma/dx$ obtained for (a) all Q^2, (b) $Q^2 > 1$ GeV^2, and (c) $Q^2 > 2$ GeV^2.

To conclude, a quantitative analysis of these distributions in terms of the quark structure of the nucleon is difficult, because the distributions are not stable against different cuts in Q^2. Moreover, scaling violations are expected to be present in all models beyond the naive quark-parton model with massless quarks (see section 1.3.12 and 1.4), and were first observed in electron and muon scattering experiments [78,79]. A more quantitative analysis is possible when the structure functions are measured as function of x and Q^2. This analysis will be given in a later section.

5.2.9 The Gross-Llewellyn-Smith sum rule

Problem

The measurement of the integral

$$\int_0^1 F_3(x)dx$$

tests the Gross-Llewellyn-Smith sum rule (section 1.3.8). The value of this integral is predicted to be equal to three, i.e. the number of valence quarks in the nucleon.

Experimentally the values of $xF_3(x)$ are obtained rather than $F_3(x)$ (see equation (23)). This fact creates the experimental problem:

> The value of $xF_3(x)$ is divided by x to obtain the integral, and for a non-vanishing value of $xF_3(x)$ at $x = 0$ the integral diverges. In general, due to the finite resolution of the experiment the value of $xF_3(x=0)$ will be finite.

Furthermore, due to the large weight of the events near $x = 0$ the integral will be dominated by statistical fluctuations of a small number of events. The problem is solved by defining a cut-off, x_{min}, below which the integral is completed by a parametrization.

Analysis

The experimental procedure followed in this analysis can be summarized as follows:

1. *The neutrino and antineutrino event distributions were unfolded in terms of the variable* $\xi = -^{10}\log x$. This has the advantage that the details of the distribution are emphasized near $x = 0$. Quartic spline functions were used, with equidistant binning, $\Delta\xi = 0.25$.

2. The measured part of the integral was calculated integrating the spline function, obtained in the unfolding procedure, weighted exponentially with ξ. This integration was performed over the interval $0 \leq \xi \leq \xi_{max}$; ξ_{max} corresponds to x_{min}.

3. The missing part of the integral was obtained using the parametrization:

$$xF_3(x) = A \cdot x^a \cdot (1-x)^b$$

This gives in terms of ξ the distribution:

$$f(\xi) = A \cdot \exp\{-(a+1) \cdot \xi/t\} \cdot \{1-\exp(-\xi/t)\}^b \qquad (53)$$

where $t = {}^{10}\log e$. This functional form was fitted to the spline function to obtain the values of the parameters A, a and b. For sufficiently large ξ_{max} the missing part of the integral was obtained by the analytical integration of equation (53) weighted exponentially with ξ/t. The correction for the missing part of the integral is then

$$\int_0^{x_{min}} F_3 dx = \frac{A}{t \cdot a} \cdot \exp(-a \cdot \xi_{max}/t)$$

which is the result of the integration over the interval $\xi_{max} < \xi < \infty$.

4. The value of x_{min} was optimized with the criterion of minimum uncertainty in the result. The uncertainty in the measured part follows from the unfolding procedure. The uncertainty in the missing part was taken to be one third of its value. This number was suggested by the precision of the definition of the fitted parameters.

Results

The value of the integral (the sum of the measured and fitted part) and the value of the measured part alone for different choices of x_{min} are shown in fig.47. The minimum uncertainty is obtained for $x_{min} = 0.01$. The result for this optimum value of x_{min} is

$$\int_0^1 F_3 dx = 2.66 \pm 0.39(\text{stat.}) \pm 0.13(\text{syst.})$$

consistent with the predicted value. Corrections for radiative effects and Fermi-motion were included in this analysis. The additional systematic uncertainty of 5% quoted in the result has to be added due to the absolute normalization uncertainty of the neutrino fluxes.

The value three is only predicted for fixed Q^2. Scaling violations as predicted by QCD tend to decrease the measured value when the whole Q^2-range is included in the data. At large x the structure function is probed at large Q^2, at small x the Q^2 is correspondingly lower. QCD predicts a shrinkage of the structure functions towards smaller x with increasing Q^2, and hence a decrease of the measured integral compared to three. The influence of different Q^2 admixtures can be tested partly using data separated into the kaon and pion part of the spectrum. We obtain for the high-energy part:

$$\int_0^1 F_3(x) dx = 2.46 \pm 0.46(\text{stat.}) \pm 0.12(\text{syst.})$$

and for the lower part:

$$\int_0^1 F_3(x) dx = 2.83 \pm 0.39(\text{stat.}) \pm 0.14(\text{syst.})$$

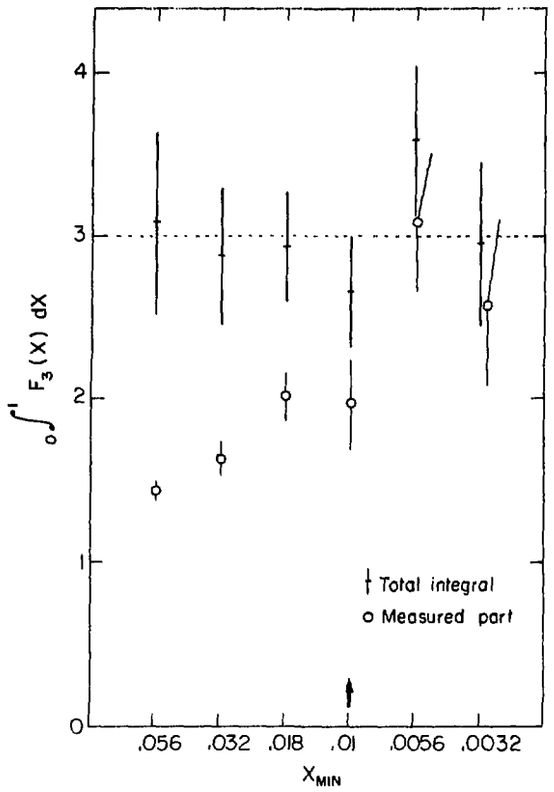

Figure 47: Total integral of F_3 and the measured part of the integral for different values of the cut-off x_{min}.

for the same value of x_{min}. Hence the influence of this effect is probably small compared to the statistical error. Results of other experiments [64,65] in this energy region are given in table 16. The BEBC group has not corrected the value for the missing part of the integral and gives a lower limit; the minimum x in this result was 0.02.

TABLE 16
Measurements of the Gross-Llewellyn-Smith sum rule.

	CHARM	CDHS	BEBC
$\int F_3$	2.66 ± 0.41	3.2 ± 0.5	≥2.5 ± 0.5

5.2.10 Structure functions

When scaling is exact, the structure functions depend only on one variable, x. However, in general the structure functions depend on x and Q^2.

Unfolding of x and Q^2 distributions

The x-Q^2 distributions of neutrino and antineutrino data were unfolded in these two dimensions. The problem encountered in the procedure is the triangular shape of the physical region in the x-Q^2 plane. The resolution unfolding method in two dimensions works only for a square physical region. Therefore, a coordinate transformation was performed:

$$(x,Q^2) \rightarrow (x,g(x,Q^2))$$

such that this requirement was fulfilled. We have used g = $\sqrt{E_h}$. This choice has the advantage that the experimental resolution is constant in this variable. Hence the x-distributions in bins of E_h are a direct result of the unfolding procedure. However, at every point in the x-$\sqrt{E_h}$ plane the best estimate of the distribution function is known (fig.48).

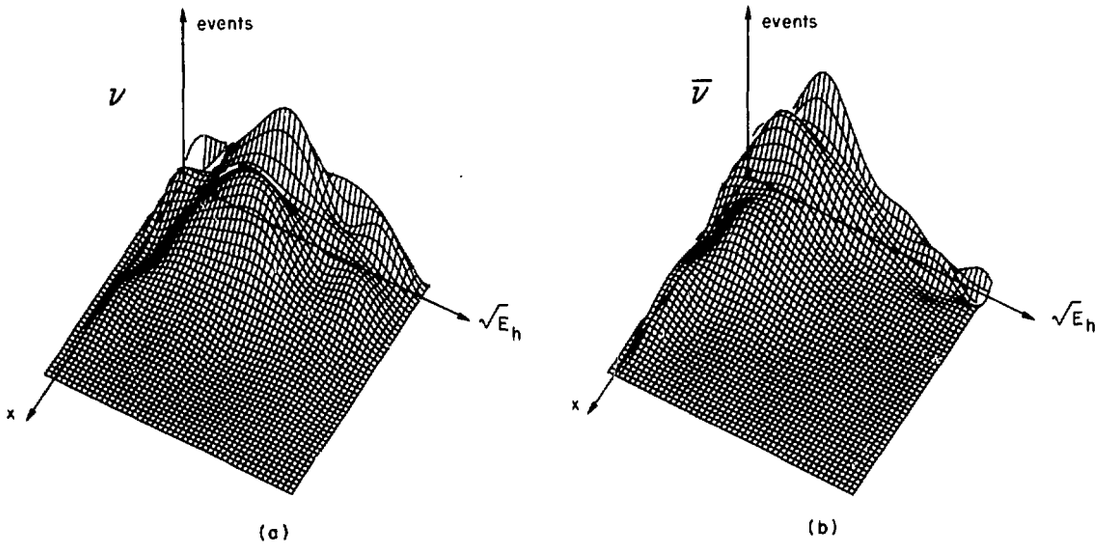

Figure 48: Two dimensional spline function as representation of the best estimate of the event distribution in x and $\sqrt{E_h}$ for neutrinos (a) and antineutrinos (b).

This fact can be used to extract the structure functions in terms of x and Q^2. The number of events, corrected for resolution effects, is found by integrating the distribution measured in the x-$\sqrt{E_h}$ plane over a region in this plane corresponding to a rectangular cell in x and Q^2. Due to the coarse resolution of the experiment in the region near x = 1 the same procedure was used to treat this kinematic boundary as in the one dimensional unfolding of the x-distributions (section 5.2.8). Hence no independent measurements of the structure functions were obtained for the region near x = 1.

Although, in principle, the contents of cells overlapping with the boundary of the physical region can be measured, most of these are not used for the analysis due to the uncertainties in the beam spectrum at the end of the energy range. No explicit cut in shower energy was applied. However, cells with most of their data in the region E_h < 2 GeV were not used in the analysis.

Extraction of structure functions

Assuming the Callan-Gross relation, the differential cross-section can be written as

$$\frac{d^2\sigma}{dxdy} = \frac{G^2ME}{\pi} \cdot \left[g_2(y) \cdot F_2(x,Q^2) \pm g_3(y) \cdot xF_3(x,Q^2) \right]$$

The functions g(y) can be found from equation (12); g_2 is not strictly a function of y only, for simplicity the term Mxy/2E is dropped in the text; this term was taken into account in the analysis. With the absolute normalization of the energy weighted neutrino flux

$$\Psi = \int E \cdot \Phi(E) dE$$

where $\Phi(E)$ is the flux, we have measured the normalized number of events in bins of x and Q^2:

$$N(i,j) = \frac{1}{\Psi} \cdot \int dE\ \Phi(E) \int dx \int dQ^2 \cdot \frac{d^2\sigma}{dx dQ^2}$$

The outer integral is over the full energy spectrum, while the inner two are within the cell in x and Q^2. The chosen normalization Ψ is suitable, because it is roughly proportional to the number of events; also other normalizations could have been chosen. By integrating the right-hand side over the flux one can define the event numbers expected in the same bin in x and Q^2 if F_2 or xF_3 would take the value one in this cell [64]:

$$N_k(i,j) \equiv \frac{G^2 M}{\pi \cdot \Psi} \cdot \int E \cdot \Phi(E) \cdot dE \int dx \int dQ^2 \cdot \frac{1}{2xME} \cdot g_k(y(x,Q^2)) \qquad ; k = 2,3$$

again normalized to the energy-weighted flux Ψ. The factor $(2xME)^{-1}$ enters because the Jacobian of the transformation $(x,y) \rightarrow (x,Q^2)$ has to be taken into account. In this notation the measured numbers of events for neutrinos and antineutrinos can be expressed in terms of the structure functions

$$N(i,j) = N_2(i,j) \cdot F_2(i,j) + N_3(i,j) \cdot xF_3(i,j)$$

$$\bar{N}(i,j) = \bar{N}_2(i,j) \cdot F_2(i,j) - \bar{N}_3(i,j) \cdot xF_3(i,j)$$

The structure functions are taken to be equal for neutrino and antineutrino interactions. These equations can be solved for F_2 and xF_3.

The values of the structure functions are defined here as averages over the cell. This point introduces problems, which are particularly important near the boundary of the physical region. A correction was applied, such that the measured points are defined as the value of the structure function at the centre of the bin.

Structure functions and scaling

The measurements of $F_2(x,Q^2)$ and $xF_3(x,Q^2)$ are shown in fig.49 and are given numerically in Appendix B. The error bars in this figure correspond to the diagonal elements of the covariance matrix. An additional scale uncertainty of ≈5% due to the flux normalization is not shown in the figure. In fits to the data the non-diagonal elements have to be taken into account. The bin-to-bin correlations are positive for adjacent Q^2-bins and negative for adjacent x-bins. The error bars include resolution unfolding uncertainties. The method used for the unfolding of experimental resolutions enables one to include the statistical uncertainties induced by the finite resolutions in the errors in a mathematically rigorous way. The general trend of an increase of the structure functions with increasing Q^2 for small x and the opposite behaviour for large x is visible for F_2. In the case of xF_3 the slopes as a function of Q^2 are not significant. In the large x region the functions F_2 and xF_3 coincide, which indicates that the sea quarks do not contribute here significantly (see equation (17)). The scaling violation parameter, B, defined by

$$B = \frac{d \log F_2}{d \log Q^2}$$

is shown in fig.50 for the measured bins in x. The violations of scaling are only significant in the two lower x bins and in the highest x bin. The general trend of these violations coincides with the prediction from QCD.

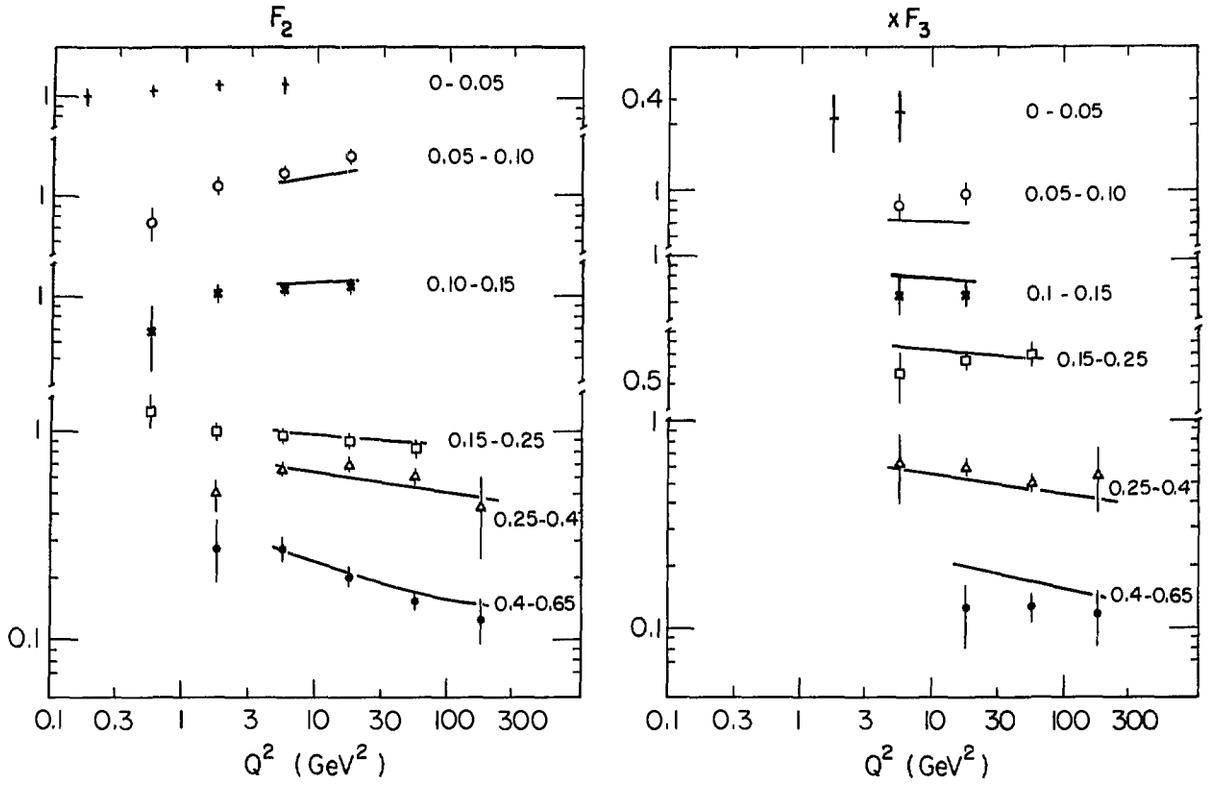

Figure 49: Measured Q^2-dependence for (a) F_2 and (b) xF_3 in bins of x. The curves are QCD fits following the Buras and Gaemers approach explained in the text in a following section. The data points are given in Appendix B.

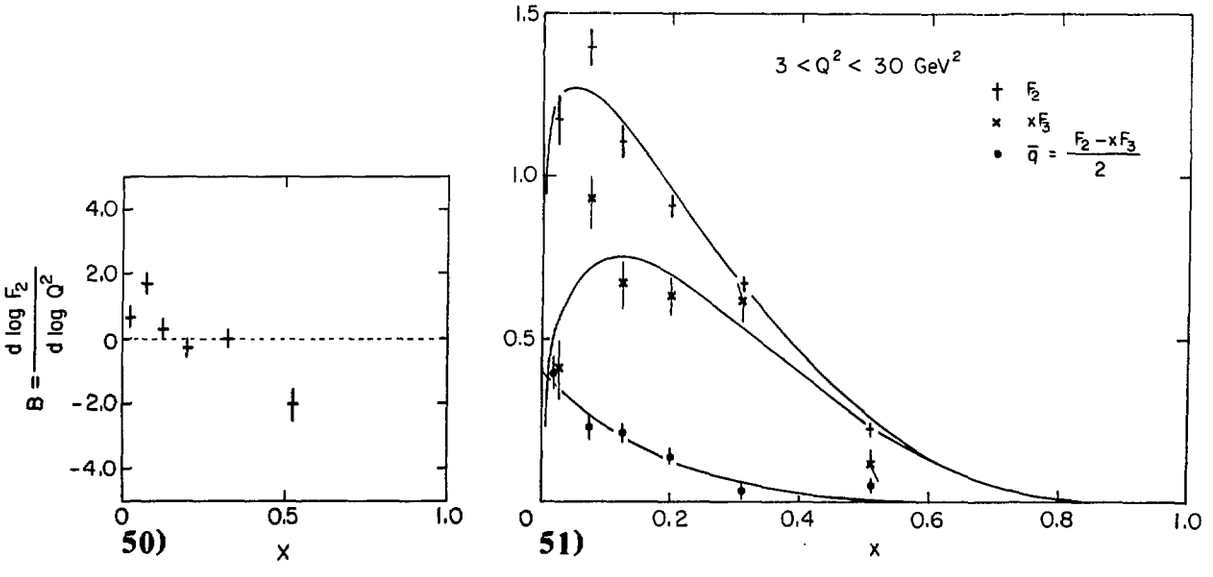

Figure 50: Logarithmic slopes of the variation of F_2 with Q^2.

Figure 51: The x-dependence of F_2, xF_3 and the sea structure function for $3 < Q^2 < 30$ GeV^2.

In fig.51 the x-dependence of the structure functions is shown for a region 3 GeV^2 < Q^2 < 30 GeV^2. The functions $F_2(x)$, $xF_3(x)$ and the structure function of the sea $q_s(x) = (1/2)\cdot(F_2(x)-xF_3(x))$ (section 1.3.6) are shown. The curves are fits of the form

$$xF_3(x) = A \cdot x^a \cdot (1-x)^b$$

$$2q_s(x) = B \cdot (1-x)^c$$

The values of the free parameters are given in table 17. Other experiments have reported values of the exponents averaged over all Q^2. The BEBC group finds for the antiquark exponent c = 4.9 (+2.4/-1.7) [64]. The results of CDHS are given for a = 0.5 fixed; they find c = 6.5 ± 0.5 and b = 3.5 ± 0.5 [65].

TABLE 17
Parameters of the fits to F_2 and xF_3 for $3 < Q^2 < 30$ GeV^2.

A	2.63 ± 0.81
a	0.41 ± 0.11
b	2.96 ± 0.31
B	0.80 ± 0.09
c	4.93 ± 0.91

Phenomenological approach to scaling violations

A more quantitative approach was persued following Buras and Gaemers [22]. This prescription was slightly modified, as described in section 1.4.3, to allow for a non-SU(3) symmetric sea at Q_0^2 and a non-vanishing Cabibbo angle. In the fits the parameter $\bar{s}/\bar{u}$ was fixed to 0.5 at $Q_0^2 = 5$ GeV^2. The data are not sensitive to this value, taking $\bar{s}/\bar{u} = 1.0$ (SU(3) symmetry) does not change the results. In order to exclude data where perturbative QCD is not supposed to be reliable, all data points with $Q^2 < 3$ GeV^2 were excluded, removing a large fraction of the measurements. Due to the conditions imposed on the unfolded distributions at x = 1 (the function, its first and second derivatives are required to be zero at x = 1) no measurements for x > 0.65 can be given. This resolves the problem whether the Bjorken x-variable or the Nachtmann ξ-variable (see equation (34) in section 1.3.12) has to be used for the scaling expressions, because they are only different from each other at large x.

When the data are corrected for Fermi-motion and radiative effects we find for the mass scale of QCD defined in leading order (equation (36)), from a fit of the parametrization of Buras and Gaemers to the data on F_2 and xF_3 for $Q^2 > 3$ GeV^2:

$$\Lambda = (0.29 \pm 0.12) \text{ GeV}$$

This value is obtained after correction for the small differences expected for the structure functions as measured by neutrino and antineutrino interactions. This difference is due to the charm threshold (see section 1.3.7), and can be calculated only when the free parameters of the model are fixed by the fit. Therefore, an iteration procedure was used, in which the data after correction based on the results of the previous fit were used in the next fit. The influence of this correction is small, and the procedure converges in a few iterations. The structure functions are in this way defined as the average of the neutrino and antineutrino structure functions.

The results for all free parameters are given in the first column of table 18. The notation is used as it was introduced in section 1.4.3. The values of η_{11} and η_{12} follow directly from the fitted values of η_{01} and η_{02} as pointed out in section 1.4.3, and are therefore not additional free parameters. The fixed value of $\bar{s}/\bar{u}$ is given for completeness. The curves in fig.49 correspond to the fit given in the first column of table 18, and are only drawn through data points used in the fit ($Q^2 > 3$ GeV^2).

The effects inducing the largest change in the values of Λ are given for comparison. The second column gives the results ignoring Fermi-motion, the

third column applies to data obtained without radiative corrections and Fermi-motion corrections. It should be noted that the fits for the non Fermi-motion corrected data are worse, especially in the high x region. The increase of the valence exponent does not correspond to the broadening of the shape of the distributions as seen in the data points themselves. The fourth column gives the results if no correction was applied for the effect that the average value of x inside a bin changes for different values of Q^2.

TABLE 18
Parameters of the fit with different corrections included.

	All corrections	No Fermi-motion corrections	No Fermi-motion and radiative corrections	No corrections for changing average x
η_{01}	0.53 ± 0.03	0.54 ± 0.03	0.55 ± 0.03	0.52 ± 0.03
η_{11}	-0.81	-0.88	-0.88	-0.81
η_{02}	3.08 ± 0.16	3.35 ± 0.16	3.46 ± 0.16	3.01 ± 0.18
η_{12}	5.56	5.69	5.75	5.56
η_S	4.55 ± 0.49	5.04 ± 0.67	5.58 ± 0.67	4.69 ± 0.50
$\bar{q}/(q+\bar{q})$	0.12 ± 0.01	0.11 ± 0.01	0.12 ± 0.01	0.11 ± 0.01
$\bar{s}/\bar{u}$	0.5	0.5	0.5	0.5
Λ	0.29 ± 0.12	0.18 ± 0.10	0.12 ± 0.09	0.37 ± 0.13

When the first two corrections are neglected the measured value of Λ decreases significantly. When the latter correction is not included the Λ estimate is increased by one standard deviation. These variations can be interpreted as an indication of the systematic uncertainty in the value of Λ. Although it is difficult to estimate the uncertainty in these corrections, a guess of 10% to 25% of the magnitude of the correction seems reasonable. It may be worthwile to note that not all experimental groups have incorporated Fermi-motion corrections in their analysis of structure functions. The influence of Fermi-motion corrections on the measurement of the Q^2-dependence found with the method adopted (described in section 5.2.4) is in agreement with the results of an analysis of these corrections reported by Bodek and Ritchie [80].

TABLE 19
Sensitivity of Λ to changes in the analysis.

Change in analysis	Effect on Λ
$\bar{\nu}/\nu$ flux ratio $+1\sigma$	+0.012
-1σ	-0.014
Absolute scale of fluxes $+1\sigma$	-0.008
-1σ	+0.002
Wide-band background $\pm1\sigma$	±0.008
Resolution function uncertainty	±0.025
K/π ratio uncertainty	±0.030
No correction for $\Delta F_2 \neq 0$, $\Delta x F_3 \neq 0$	-0.017
$\bar{s}/\bar{u}=1$, SU(3) symmetric sea	+0.028
No charmed sea	+0.021
No processes with charm	-0.078
Cabibbo angle neglected	-0.018
$\eta_{gluons} = \eta_{sea} - 1$	+0.025
$R = 0.1$ (constant)	-0.082
$R(x,Q^2) = 1.2(GeV^2)\cdot(1-x)/Q^2$	-0.013

The influence of other variations in the analysis is summarized in table 19. These effects turn out to be less important than the previously mentioned ones. The flux normalizations, the ratio of the fluxes and the most important background contribution (wide-band background) were varied by one standard deviation.

The variation of the result, when the charmed sea or all processes including charm have been neglected in the model, is given to illustrate the sensitivity to the assumptions made in the parametrization.

The influence of the assumption that the x-dependence of the gluon distribution has the same shape as the sea-quark distributions at Q_0^2 (section 1.4.3) was evaluated. One could argue that the x-dependence of the gluons is less steep than the x-dependence of the sea but steeper than the x-dependence of the valence-quarks, in the picture that the valence-quarks radiate gluons and the gluons create the sea (see section 1.3.13). The result for $\eta_{gluons} = \eta_{sea} - 1$ is given in the table.

For the extraction of the structure functions the Callan-Gross relation (equation (11)) was assumed, R = 0, supported by the result of the fit to the y-distributions (equation (14)). However, this measurement leaves room for a 10% violation of this relation. (Electron scattering experiments find such a value [77]). The result of the alternative assumption R = 0.1 is given in the table. In QCD one expects R to decrease with increasing x [81]. The result of an analysis with the approximation $R = 1.2(GeV^2)\cdot(1-x)/Q^2$ suggested by the CHIO (Chicago-Harvard-Illinois-Oxford) muon scattering experiment [82] is also given in the table.

Finally, in order to interpret the significance of the value of Λ found from the data, a fit was performed including higher twist effects. They were parametrized by the substitution (section 1.4.4)

$$F_2 \rightarrow F_2 \cdot \left[1 + \frac{\mu_1^2}{Q^2(1-x)} + \frac{\mu_2^4}{Q^4(1-x)^2} \right]$$

and a similar substitution for xF_3. No theoretical predictions for the mass parameters μ_1 and μ_2 exist. The parametrization can be used to investigate whether the scaling violations are better described by the logarithmic behaviour of QCD or by powers of Q^2 as expected for non-perturbative effects. In a fit using both μ_1 and μ_2 as free parameters we find an insignificant contribution of μ_2. Therefore, a fit using only μ_1 as additional free parameter, fixing $\mu_2 = 0$, was performed. We find for the best fit:

$$\Lambda = (0.29 \pm 0.12)\ GeV$$
$$\mu_1 = (0.28 \pm 0.09)\ GeV$$

The value of Λ is not changed considerably, its statistical significance is smaller due to the correlation of the simultanous measurement of Λ and μ_1. The correlation coefficient is large and negative. The fit including both mass parameters gives:

$$\Lambda = (0.24 \pm 0.12)\ GeV$$
$$\mu_1 = (0.28 \pm 0.24)\ GeV$$
$$\mu_2 = (0.11 \pm 2.50)\ GeV$$

The values of μ_1 and μ_2 are not well constrained by the data. Going even further, allowing the contributions of the μ_i terms to be negative, a value of Λ compatible with zero can be obtained combined with a suitable positive contribution of the first correction term and a negative contribution of the second correction term.

From table 18 and 19 one can read off that the result of the analysis is not rigorous when interpreted in terms of Λ. All kinds of assumptions made in the analysis have an influence on its value (radiative corrections, Fermi-mo-

tion correction, Callan-Gross relation, gluon distribution, higher twist effects, etc.). In addition, part of the violations of scaling at low x are expected to be due to charm production (included in the model); results of muon-scattering indicate that 1/3 of the scaling violations in this region are due to charm production [83]. For the higher x region $0.4 < x < 0.65$ this argument is not applicable nor can one argue that scaling violations in this region are due to higher twist effects only, as they are expected to contribute only at low Q^2. The scale-breaking is observed up to the highest Q^2 in the data. Hence some QCD scale-breaking must be present to explain the data.

The theoretical interpretation of the measurement of Λ using this approach is not unambiguous. The functional form assumed for the x-distributions at Q_0^2 is an empirical choice which is found to fit the data satisfactorily, but is not predicted by the theory. Only the change of the distributions with Q^2 is fixed by the evolution equations. An additional theoretical arbitrariness follows from the fact that the inclusion of higher order terms in the QCD perturbation expansion may influence the measured value of Λ.

However, scaling violations are observed in the data and they are reasonably well described by the fit of this model to the data. Hence as a phenomenological measure of scaling violations the value of Λ makes sense and can be used to compare results obtained by other experiments, although such a comparison is made difficult by the different correction procedures and different assumptions used in the analyses of the different groups.

Results of other experiments

The results of this analysis can be compared with recent measurements of structure functions obtained by other experiments. Various groups have used different binnings, because the particular experimental conditions are different such as statistics of the event sample, resolution functions and beam spectra. Therefore, in order to make a comparison possible the QCD-prediction based on the Buras and Gaemers fit to the data of this experiment were superimposed on the data points of other experiments. The data are compared with recent CDHS [84], Gargamelle [85] and HPWFRO [76] data.

The kinematic region in x and Q^2 probed by the various experiments is shown in fig.52. For constant x the high Q^2 limit is given by the beam spectrum and the low Q^2 limit by the hadron energy resolution at low shower energies. The x-resolution limits the measurements at high x. In this region the resolution is dominated by the resolution of the muon momentum, which is well measured in bubble chamber experiments (e.g. Gargamelle).

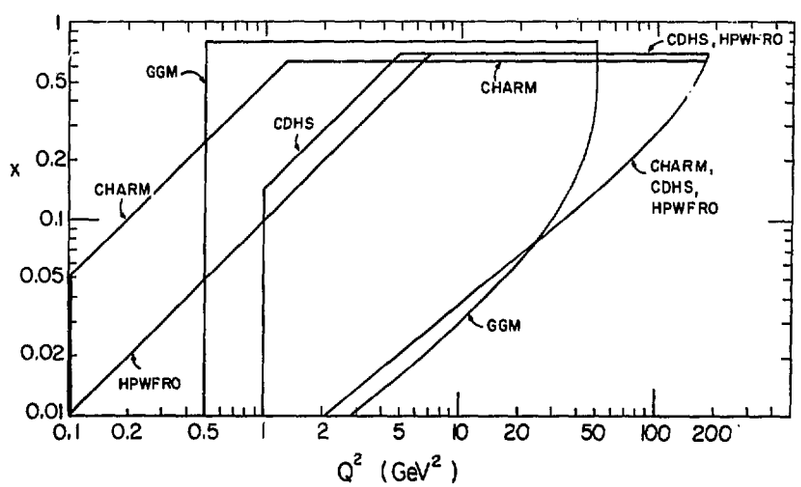

Figure 52: The kinematic region probed by various experiments.

In fig.53 data on F_2 and xF_3 of the GGM-SPS collaboration are shown. These results are based on 3000 neutrino and 3800 antineutrino events taken in the CERN wide-band beam. An overall scale error of 10% was estimated due to the normalization of the beam. Following the preference of the Gargamelle collaboration, this error is linearly added and included in the error bars shown in the figure. Fermi-motion corrections were applied to the data, radiative corrections were neglected. The curves represent the prediction based on the fit to the CHARM data. The agreement of the curve and the data points is excellent.

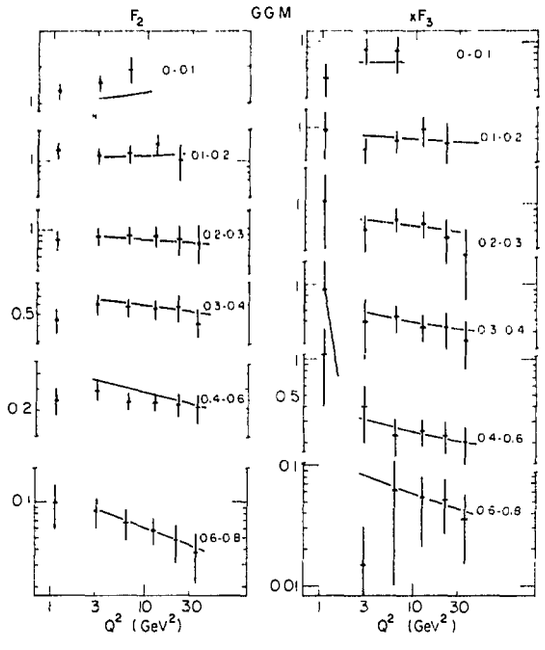

Figure 53: Measurements of F_2 and xF_3 by the Gargamelle collaboration. The curves represent the prediction from the fit to the CHARM data.

In fig.54 recent high-statistics data of the CDHS collaboration are shown. The measurements of F_2 and xF_3 are based on 65000 neutrino and 25000 antineutrino events obtained in the CERN narrow-band beam. The structure functions are obtained with the assumption R = 0.1. Fermi-motion corrections were not applied to the data. The ≈5% scale uncertainty due to the normalization of the beam is not included in the errors. The curves represent the prediction for the data points obtained from the fit to the CHARM data. The agreement for small x is good, but for x > 0.45 a clear discrepancy shows up. A part of the discrepancy can be explained by the fact that no Fermi-motion correction was applied to the CDHS data. The Fermi-motion smearing for an iron target as calculated by Bodek and Ritchie [80] was incorporated in the dashed curves in this figure; the effect is to small to explain fully the discrepancy of the two measurements. The Q^2-dependence of the two sets of data are compatible. The shapes of the structure functions do not agree (broader for CDHS and narrower for CHARM). Presumably the differences are due to unknown systematics, such as resolution functions and possibly the procedure used to correct for the resolutions.

The structure functions measured by the HPWFRO collaboration are shown in fig.55 together with the prediction for this binning obtained by the fit to the CHARM data. The results are based on 21500 neutrino and 7500 antineutrino events obtained in the Fermilab quadrupole triplet and sign-selected bare-target beam. In the analysis of this group the assumption R = 0.1 was used; no Fermi-motion corrections were applied to the data. An additional scale uncertainty of ≈5% is not shown in the figure. The data points and the curves

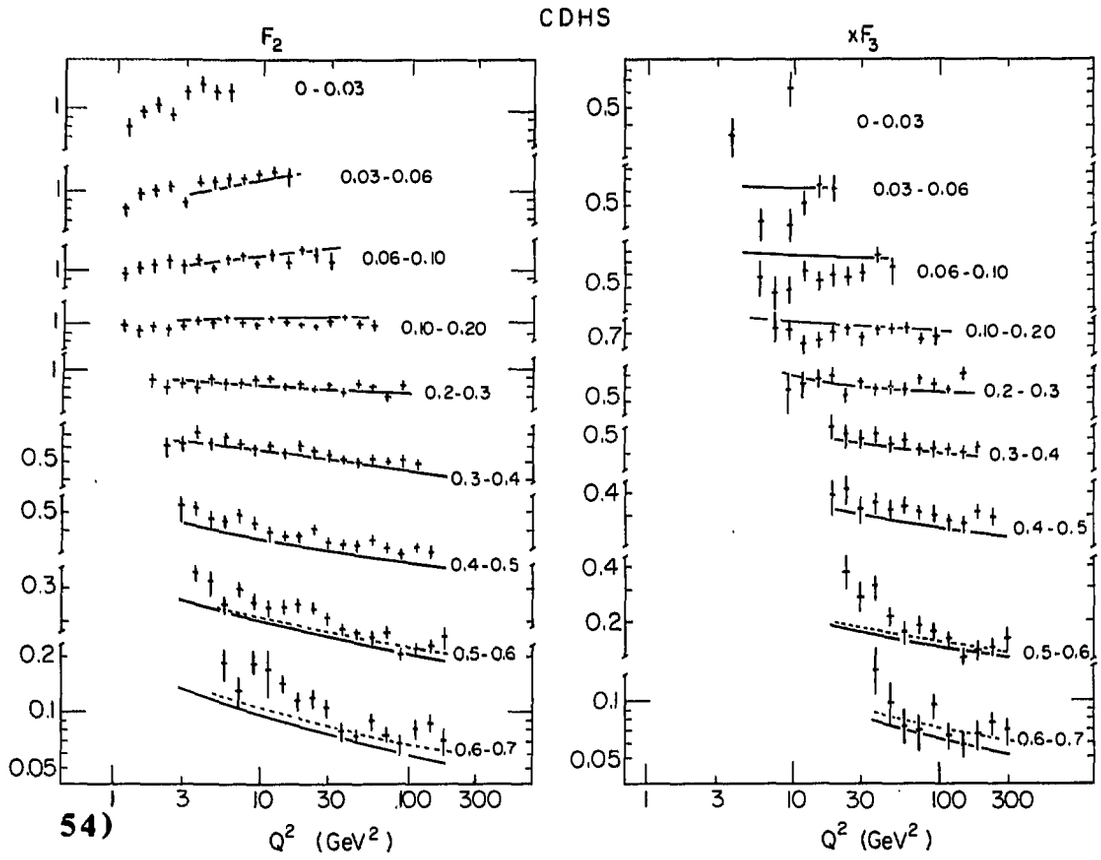

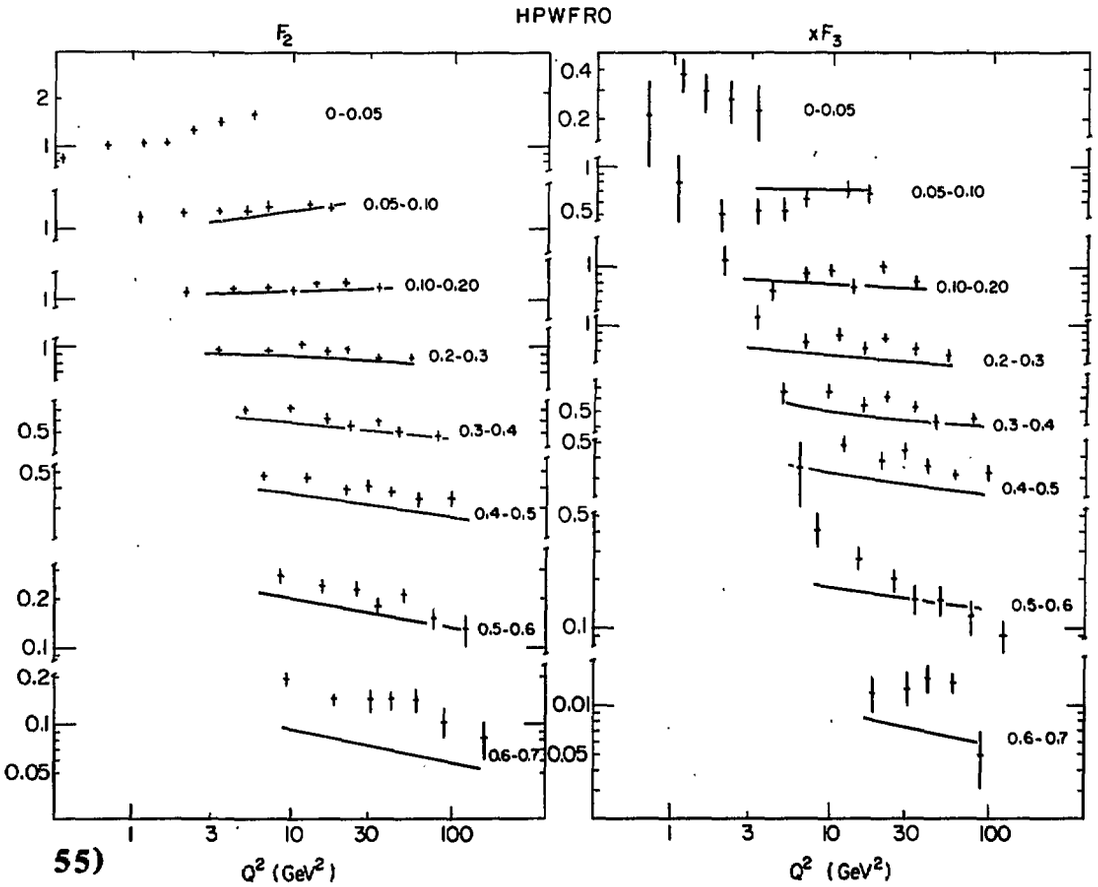

Figure 54: Structure function measurements by CDHS. The drawn curves represent the prediction from the fit to the CHARM data. The dashed curve gives the prediction smeared with Fermi-motion.

Figure 55: HPWFRO structure function data. The curves show the prediction from the fit to the CHARM data.

agree reasonably well, except at the large x region, where the HPWFRO data show a significantly broader x-dependence than the CDHS, Gargamelle and CHARM data. Nevertheless, the Q^2-dependence of this data agrees with the other measurements.

The Q^2-dependences of the stucture functions can be compared using the parameter $B = d\log F_2/d\log Q^2$. In fig.56(a) the measurements of this parameter for F_2 are shown as a function of x for the BEBC [64] and CDHS [84] and CHARM data. Measurements of this parameter reported by electron [77] and muon [82] scattering experiments on isoscalar targets are shown in fig.56(b). The fits to the data of [64,77,82] are taken from [86]. The various experiments agree qualitatively on the Q^2-dependence of F_2.

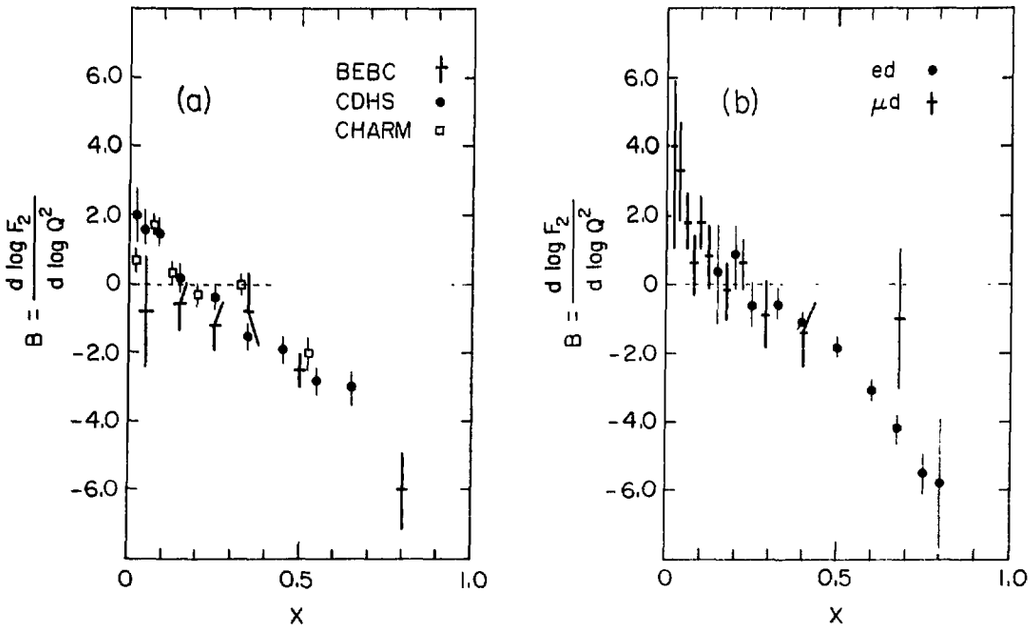

Figure 56: Comparison of (a) neutrino experiments and (b) electron and muon scattering experiments in terms of the scaling violation parameter B.

The value of Λ obtained in this experiment can be compared with results obtained by other experiments. The CDHS collaboration finds in a recent analysis [84] of their neutrino data Λ = (0.2 (+0.15,-0.10)) GeV, in which the error includes systematics. In this analysis R = 0.1 was assumed and no Fermi-motion corrections were made. This value was obtained by numerical integration of the Altarelli-Parisi equation (38) for data with $Q^2 > 2$ GeV^2 and $W^2 > 11$ GeV^2. Previous CDHS results [65] based on four times less events were obtained with the Buras and Gaemers method and yielded Λ = (0.47 ± 0.11 (± 0.1 syst.)) GeV. In this case R = 0 was assumed and only data with $Q^2 > 3$ GeV^2 were included. A combined analysis of the non-singlet structure function xF_3 obtained by the BEBC group [64] and CDHS [65] were reported by Barker et al. [87]. They find for these data the allowed range $0.13 \leq \Lambda \leq 0.91$ GeV. Their analysis of the non-singlet electromagnetic structure function (the difference of protons and neutrons) yields the allowed range $0.13 \leq \Lambda \leq 0.64$ GeV, combining SLAC electron scattering data [88] and CHIO muon scattering data [82]. The EMC (European Muon Collaboration) muon scattering experiment [89] finds Λ =(0.1 ± 0.1) GeV, where the error is dominated by systematic uncertainties.

In summary, although the values of Λ obtained by different experiments using different probes, different experimental techniques and different analysis methods differ quite much, they agree within the rather large uncertainties.

5.3 CONCLUSIONS

5.3.1 Total cross-sections

The cross-sections of deep inelastic neutrino and antineutrino scattering on isoscalar targets were measured, making use of an event-by-event classification of NC and CC interactions. The results are summarized in table 20.

TABLE 20
Results of the total cross-section measurements.

R	$= 0.320 \pm 0.009$ (stat) ± 0.003 (syst) [a]
$\bar{R}$	$= 0.377 \pm 0.020$ (stat) ± 0.003 (syst) [a]
σ^{CC}_{tot}	$= 0.604 \pm 0.009$ (stat) ± 0.031 (syst) $\times 10^{-38} \times E_\nu$ cm^2 GeV nucleon^{-1}
$\bar{\sigma}^{CC}_{tot}$	$= 0.301 \pm 0.008$ (stat) ± 0.016 (syst) $\times 10^{-38} \times E_{\bar{\nu}}$ cm^2 GeV nucleon^{-1}
r	$= 0.498 \pm 0.015$ (stat) ± 0.012 (syst)
$\sin^2\theta$	$= 0.220 \pm 0.013$ (stat) ± 0.004 (syst) [b]
$\sin^2\theta$	$= 0.230 \pm 0.022$ (stat) ± 0.005 (syst) [c]

a) For shower energy > 2 GeV.

b) From QCD model calculations. The systematic errors quoted do not include the uncertainties of the model.

c) From Paschos-Wolfenstein relation.

The neutral-current chiral coupling constants were obtained without making use of the Glashow-Salam-Weinberg model. The results were:

$$g_l^2 = \rho^2(u_l^2 + d_l^2) = 0.305 \pm 0.013$$

$$g_r^2 = \rho^2(u_r^2 + d_r^2) = 0.036 \pm 0.013$$

A statistically significant contribution of the right-handed coupling of the neutral hadronic current was observed, interpreted in the standard model of Glashow-Salam-Weinberg as being due to the mixing with the electromagnetic current.

The strengths of the NC and the CC weak coupling were found to be equal to within ±2.5%:

$$\rho = 1.027 \pm 0.023$$

A value of the electromagnetic mixing angle within the framework of the Glashow-Salam-Weinberg model (ρ=1) was deduced corresponding to

$$\sin^2\theta = 0.220 \pm 0.014$$

The values of the left-handed and the right-handed coupling constants of the weak neutral hadronic current determined by these measurements, and the total cross-sections, agree with previous results obtained with different methods.

5.3.2 Charged-current y-distributions

The differential cross-sections $d\sigma/dy$ were obtained for charged-current interactions. From simultaneous fits to the neutrino and antineutrino data the following results were deduced:

> The relative contribution of antiquarks as measured by neutrinos is 0.10 ± 0.04 and 0.16 ± 0.01 for antineutrino interactions. The difference, attributed to the strange-quark contribution is 0.06 ± 0.04. The relative contribution of antiquarks obtained from the shape of the y-distributions agrees with the value deduced from the charged-current cross-section ratio.
>
> No significant deviation from the Callan-Gross relation was found. The sensitivity of the test is 11%.
>
> Extrapolations of the y-distributions to $y = 0$ are compatible with charge symmetry at the level of one standard deviation (6%).

The results agree with previous measurements.

5.3.3 Structure functions

Charged-current differential cross-sections $d\sigma/dx$ were obtained. No significant quantitative conclusions were drawn due to the different admixtures of the values of Q^2 as a function of x for the neutrino and antineutrino distributions. The evaluation of the Gross-Llewellyn-Smith sum rule yielded

$$\int_0^1 F_3 dx = 2.66 \pm 0.41$$

compatible with three valence quarks in the nucleon.

The nucleon structure functions F_2 and xF_3 were obtained as a function of x and Q^2. As a consequence of the good shower energy resolution, F_2 could be obtained for a large range of Q^2, especially down to low values of Q^2. The Q^2-range over which xF_3 was measured is limited by the statistics of the data. The following can be concluded.

> Statistically significant violations of scaling were observed for the structure function F_2. The value of F_2 increases with Q^2 for small x and decreases with Q^2 for large x, in qualitative agreement with QCD predictions. The rise of F_2 for small x could be explained qualitatively by charm production, without the need of QCD effects. However, the decrease of F_2 for $0.4 < x < 0.65$ is visible over the whole Q^2-range up to large Q^2 and is difficult to be explained without QCD scaling violations.
>
> A quantitative comparison with QCD was persued with the method of Buras and Gaemers. From a simultaneous fit to F_2 and xF_3 taking only data with $Q^2 > 3$ GeV^2, a value of Λ in the leading order approximation was obtained
>
> $$\Lambda = (0.29 \pm 0.12) \text{ GeV}$$
>
> where the error is statistical only. The systematic uncertainties were found to be large (≈ 0.1), due to uncertainties in various corrections. Especially radiative and Fermi-motion corrections changed the value of Λ considerably.

The main disadvantage of the method of Buras and Gaemers is the introduction of a model of the x-dependence of the structure functions, and the need of extra assumptions to describe the sea and gluon distributions. These model dependences can in principle be removed by integrating the Altarelli-Parisi equation for the non-singlet function xF_3. The statistical significance of the measurement of xF_3 is not sufficient to justify a QCD analysis on the basis of this structure function alone.

The observed scaling violations are in agreement with results obtained by other experiments. The scaling violations are consistent with the QCD picture.

The measurements of the x-dependence of the structure functions of the various experiments agree less well. At large x significant differences are observed in the comparison of the measurements. The discrepancies may be explained by systematic uncertainties in the corrections for the experimental resolutions. Due to the steepness of the structure functions at large x, and the coarse resolution of all experiments in the large x region, the differences in the analyses are likely to show up in this region.

A quantitative analysis in terms of QCD is difficult due to the fact that a significant part of the data is obtained below the value of Q^2 above which QCD is supposed to give reliable results. These difficulties are enlarged because a satisfactory theoretical description of the so-called higher twist effects is not available. For these reasons experiments with higher-energy beams are needed to give precise and reliable measurements of Λ.

REFERENCES

[1] M.Jonker, J.Panman, F.Udo (NIKHEF, Amsterdam, Netherlands); J.V.Allaby, U.Amaldi, G.Barbiellini, A.Baroncelli, V.Blobel, G.Cocconi, W.Flegel, W.Kozanecki, K.H.Mess, M.Metcalf, J.Meyer, R.S.Orr, F.Schneider, V.Valente, A.M.Wetherell and K.Winter (CERN, Geneva, Switzerland); F.W.Büsser, P.D.Gall, H.Grote, B.Kröger, E.Metz, F.Niebergall, K.H.Ranitzsch and P.Stähelin (II. Institut für Experimentalphysik, Universität Hamburg, Hamburg, Germany); E.Grigoriev, V.Kaftanov, V.Khovansky and A.Rosanov (Institute of Theoretical and Experimental Physics, Moscow, USSR); R.Biancastelli, B.Borgia, C.Bosio, A.Capone, F.Ferroni, E.Longo, P.Monacelli, F.de Notaristefani, P.Pistilli and C.Santoni (Istituto Nazionale di Fisica Nucleare, Roma, Italy).

[2] G.Danby et al., Phys. Rev. Lett. 9 (1962) 36.

[3] F.J.Hasert et al., Gargamelle coll., Phys. Lett. B46 (1973) 138.

[4] P.Berge et al., Fermilab report FN-282 (1975) unpublished.

[5] P.Musset and J.P.Vialle, Phys. Reports 39 (1978) 1.

[6] P.C.Bosetti et al., BEBC-ABCLOS coll., Nucl. Phys. B142 (1978) 1.

[7] B.C.Barish et al.,CITF coll., Proc. Sixth Hawaii Topical Conf. in Particle Physics (1975).
B.C.Barish et al., CITF coll., Nucl. Instr. Methods 130 (1975) 49.

[8] A.Benvenuti et al., HPWF coll., Nucl. Instr. Methods 125 (1976) 447,
A.Benvenuti et al., HPWF coll., Nucl. Instr. Methods 125 (1976) 457.

[9] E.D.Miller et al., Phys. Rev. Lett. 23 (1969) 930.
G.Bloom et al., Phys. Rev. D5 (1972) 528.

[10] M.Holder et al., CDHS coll., Nucl. Instr. Methods 148 (1978) 235.

[11] M.Jonker et al., CHARM coll., Phys. Lett. B93 (1980) 203.

[12] M.Jonker et al., CHARM coll., Phys. Lett. B86 (1979) 229.

[13] M.Jonker et al., CHARM coll., Phys. Lett. B96 (1980) 435.

[14] M.Jonker et al., CHARM coll., Phys. Lett. B99 (1981) 265.

[15] M.Jonker et al., CHARM coll., Phys. Lett. B102 (1981) 67.

[16] N.Cabibbo, Phys. Rev. Lett. 10 (1963) 531.

[17] J.Schwinger, Ann. Phys. (NY) 2 (1957) 407.
S.L.Glashow, Nucl. Phys. 22 (1961) 579.
A.Salam and J.Ward, Phys. Lett. 13 (1964) 168.
S.Weinberg, Phys. Rev. Lett. 19 (1967) 1264.
A.Salam, Elementary Particle Theory, edited by N.Svartholm, (Almquist and Forlag, Stockholm, 1968).
S.Weinberg, Phys. Rev. D5 (1972) 1412.
A short historical review of the many contributions which led to this theory is given in:
M.Veltman, Proc. 6th International Symposium on Electron and Photon Interactions at High Energies, Bonn 1973.

[18] S.L.Glashow, J.Iliopoulos and L.Maiani, Phys. Rev. D2 (1970) 1285.

[19] G.'t Hooft, Nucl. Phys. B35 (1971) 167.

[20] See e.g.:
P.Q.Hung and J.J.Sakurai, Phys. Lett. B36 (1976) 295
L.M.Sehgal, Phys. Lett. B71 (1977) 99.

[21] J.D.Bjorken, In Proceedings of 3rd International Symposium on Electron and Photon Interactions, Stanford, California (1967).
J.D.Bjorken and E.A.Paschos, Phys. Rev. 185 (1969) 1975.
R.P.Feynman, Phys. Rev. Lett. 23 (1969) 1415.

[22] A.J.Buras and K.J.F.Gaemers, Nucl. Phys. B132 (1978) 249.

[23] J.E.Kim et al., Rev. Mod. Phys. 53 (1981) 211.
[24] E.A.Paschos and L.Wolfenstein, Phys. Rev. D7 (1973) 91.
[25] E.A.Paschos, Proc. Rencontre de Moriond, Les Arcs (1980).
[26] The derivation of this equation can be found in textbooks, see e.g.:
F.E.Close, An Introduction to Quarks and Partons, Academic Press, London (1979).
[27] M.Gell-Mann, Phys. Lett. 8 (1964) 214.
G.Zweig, CERN-preprints TH401, TH412 (1964).
[28] J.D.Bjorken, Phys. Rev. 179 (1969) 1547.
[29] C.Callan and D.J.Gross, Phys. Rev. Lett. 22 (1969) 156.
[30] A.Benvenuti et al., HPWF coll., Phys. Rev. Lett. 34 (1975) 419.
[31] B.C.Barish, Proc. Intern. Symp. "La Physique du Neutrino a Haute Energie", Ecole Polytechnique, Paris (1975).
[32] D.J.Gross and C.H.Llewellyn-Smith, Nucl. Phys. B14 (1969) 337.
[33] D.H.Perkins, P.Schreiner and W.G.Scott, Phys. Lett. B67 (1977) 347.
[34] H.Georgi and H.D.Politzer, Phys. Rev. Lett. 36 (1976) 1281
Erratum Phys. Rev. Lett. 37 (1976) 68;
and Phys. Rev. D14 (1976) 1829.
[35] O.Nachtmann, Nucl. Phys. B63 (1973) 237;
O.Nachtmann, Nucl. Phys. B78 (1974) 455.
[36] See e.g.:
J.Ellis and C.T.Sachrajda, Proc. 1979 Cargese Summer Institute on Quarks and Leptons, Cargese, France (1980).
E.Reya, Phys. Reports 69 (1981) 197.
[37] G.Altarelli and G.Parisi, Nucl. Phys. B26 (1977) 298.
[38] See e.g.:
L.F.Abbott, W.B.Atwood and R.M.Barnett, Phys. Rev. D22 (1980) 582.
L.F.Abbott and R.M.Barnett, Ann. Phys. (N.Y.) 125 (1980) 276.
H.D.Politzer, Nucl. Phys. B172 (1980) 349.
[39] H.W.Atherton, CERN/Lab.II/EA/74-6, unpublished.
[40] G.Sigurdsson and G.Stefanini, CERN/NP/BEAM/75-1 (1975) (unpublished).
[41] G.Cavallari et al., IEEE Transactions on Nuclear Science, NS-25 (1978) 600.
[42] H.W.Atherton et al., CERN 80-07 (1980).
[43] K.L.Brown and Ch.Iselin, CERN 74-2 (1974).
[44] J.May, G.Sigurdsson and G.Stefanini (CERN), private communication.
[45] Particle Data Group, Review of particle properties, Phys. Lett. B75 (1978).
[46] Particle Data Group, Rev. Modern Phys. 52 No.2 (1980).
[47] H.Heyne (CERN), private communication.
[48] A.N.Diddens et al., CHARM coll., Nucl. Instr. Methods 178 (1980) 27.
[49] M.Ferrat, F.Udo and V.Valente, preprint CERN-EP/79-2.
[50] C.Bosio et al., CHARM coll., Nucl. Instr. Methods 157 (1978) 35.
A.N.Diddens et al., CHARM coll., Nucl. Instr. Methods 176 (1980) 189.
G.Fremont et al., CHARM coll., CERN 80-5 (1980).
[51] W.Tanenbaum, Nucl. Instr. Methods 106 (1973) 393.
[52] K.H.Mess et al., CERN DD/80-7 (1980).
[53] M.Metcalf, M.Regler and C.Broll, CERN 73-2 (1973).
[54] M.Regler, Acta Phys. Austr. 4 (1978).
[55] R.Frühwirth, CERN-DD/77/23 (1977).
[56] S.Brandt, Statistical and Computational Methods in Data Analysis, North-Holland, Amsterdam (1970).
[57] M.Jonker et al., CHARM coll., Experimental study of opposite and same-sign dimuon events produced by neutrinos and antineutrinos (in preparation).
[58] J.B.Blietschau et al., Gargamelle coll., Nucl. Phys. B118 (1977) 218.
[59] P.Wanderer et al., HPWF coll., Phys. Rev. D17 (1978) 1679.
[60] F.S.Merritt et al., CITF coll., Phys. Rev. D17 (1978) 2199.
[61] P.C.Bosetti et al., BEBC ABCLOS coll., Phys. Lett. B76 (1978) 505.
M.Deden et al., BEBC ABCLOS coll., Nucl. Phys. B149 (1979) 1.

[62] M.Holder et al., CDHS coll., Phys. Lett. B71 (1977) 222.
C.Geweniger, CDHS coll., Proc. Int. Conf. Neutrino '79, Bergen, 1979 (eds. A.Haatuft and C.Jarlskog), vol.2, p.392. Bergen, Norway (1979).
[63] B.C.Barish et al., CITF coll., Phys. Rev. Lett. 38 (1977) 314.
B.C.Barish et al., CITF coll., Phys. Rev. Lett. 39 (1977) 741.
B.C.Barish et al., CITF coll., Phys. Rev. Lett. 39 (1977) 1595.
B.C.Barish et al., CITF coll., Phys. Rev. Lett. 40 (1978) 1414.
[64] P.C.Bosetti et al., BEBC ABCLOS coll., Phys. Lett. B70 (1977) 273.
P.C.Bosetti et al., BEBC ABCLOS coll., Nucl. Phys. B142 (1978) 1.
[65] J.G.H. de Groot et al., CDHS coll., Z. Physik C1 (1979) 143.
[66] T.Kondo, CFRR coll., to be publ. Proc. Rencontre de Moriond, Les Arcs (1981).
[67] J.May and H.Wachsmuth (CERN), private communication.
[68] S.J.Barish et al., Report ANL-HEP-CP-75-40 (1975).
M.Rollier, Gargamelle coll., Proc. Intern. Symp. "La physique du neutrino a haute energie", Ecole Polytechnique, Paris (1975).
[69] I.Liede and M.Roos, Nucl. Phys. B167 (1980) 397.
[70] C.Y.Prescott et al., Phys. Lett. B84 (1979) 524.
[71] W.J.Marciano and A.Sirlin, Invited Talk VPI Workshop on "Weak Interactions as probes of Unification", (1980).
[72] C.de Boor, A practical guide to splines, Springer (1978).
[73] H.von Geramb, University of Hamburg, private communication.
J.P.Jeukenne, A.Lejeune and C.Mahaux, Phys. Reports C25 (1976) 83.
[74] F.H.Heinlich et al., Nucl. Phys. A228 (1974) 478.
[75] A. de Rujula, R.Petronzio and A.Savoy-Navarro, Nucl. Phys. B154 (1979) 394.
[76] S.M.Heagy et al., HPWFRO coll., Phys. Rev. D23 (1981) 1045.
[77] A.Bodek et al., SLAC MIT coll., Phys. Rev. D20 (1979) 1471.
[78] E.M.Riordan et al., SLAC-PUB-1634 (1975) unpublished.
[79] D.J.Fox et al., Phys. Rev. Lett. 33 (1974) 1504.
Y.Watanabe et al., Phys. Rev. Lett. 35 (1975) 898.
H.L.Anderson et al., Phys. Rev. Lett. 37 (1976) 4.
[80] A.Bodek and J.L.Ritchie, Phys. Rev. D23 (1981) 1070.
[81] A.Gonzalez-Arroyo, C.Lopez and F.J.Yndurain, Phys. Lett. B98 (1981) 215.
[82] B.A.Gordon et al., CHIO coll., Phys. Rev. D20 (1979) 2645.
[83] A.R.Clark et al., Phys. Rev. Lett. 45 (1980) 1465.
[84] H.Wahl, CDHS coll., to be publ. Proc. Rencontre de Moriond, Les Arcs (1981).
[85] P.Heusse and C.Matteuzzi, Gargamelle coll., private communication.
[86] W.S.C.Williams, Proc. Intern. Symp. on Lepton and Photon Interactions, Fermilab, Batavia, Illinois (1979).
[87] I.S.Barker, C.S.Langensiegen and G.Shaw, CERN preprint TH 2988 (1980).
[88] A.Bodek et al., Phys. Rev. D20 (1979) 1471.
M.Mestayer et al., SLAC-rep-214 (1979).
J.S.Poucher et al., Phys. Rev. Lett. 32 (1974) 118, and SLAC-PUB-1309 (1973).
W.B.Atwood et al., Phys. Lett. B64 (1976) 479, and SLAC-PUB-185 (1975).
E.D.Bloom et al., SLAC-PUB-653.
S.Stein et al., Phys. Rev. D12 (1975) 1884.
G.Miller et al., Phys. Rev. D5 (1972) 528.
[89] P.R.Norton, EMC coll., Proc. Intern. Conf. on High-Energy Physics-1980, Madison, Wisconsin (1980).

APPENDIX A

The numerical values of the differential cross-sections dσ/dy are given in table 21. The errors correspond to the diagonal elements of the covariance matrix. The off-diagonal elements are small, typically smaller than 10%. The full covariance matrix can be supplied on request.

TABLE 21
Differential cross-sections dσ/dy.

30 GeV < E < 200 GeV

y	neutrinos	antineutrinos
0.0 - 0.1	5.99 ± 0.42	6.29 ± 0.53
0.1 - 0.2	6.15 ± 0.26	5.03 ± 0.21
0.2 - 0.3	6.07 ± 0.24	4.41 ± 0.19
0.3 - 0.4	5.87 ± 0.24	3.59 ± 0.16
0.4 - 0.5	5.68 ± 0.24	2.27 ± 0.15
0.5 - 0.6	5.66 ± 0.24	2.32 ± 0.14
0.6 - 0.7	5.97 ± 0.25	1.89 ± 0.12
0.7 - 0.8	6.11 ± 0.26	1.29 ± 0.11
0.8 - 1.0	5.78 ± 0.26	1.13 ± 0.10

x 10^{-39} x E cm^2/GeV

30 GeV < E < 90 GeV

y	neutrinos	antineutrinos
0.0 - 0.1	8.05 ± 1.37	6.23 ± 0.93
0.1 - 0.2	6.70 ± 0.41	4.95 ± 0.25
0.2 - 0.3	5.77 ± 0.37	4.39 ± 0.22
0.3 - 0.4	6.03 ± 0.36	3.65 ± 0.20
0.4 - 0.5	5.72 ± 0.36	2.74 ± 0.18
0.5 - 0.6	5.77 ± 0.36	2.33 ± 0.16
0.6 - 0.7	6.22 ± 0.37	1.82 ± 0.15
0.7 - 0.8	5.66 ± 0.39	1.26 ± 0.13
0.8 - 1.0	5.90 ± 0.47	1.15 ± 0.13

x 10^{-39} x E cm^2/GeV

90 GeV < E < 200 GeV

y	neutrinos	antineutrinos
0.0 - 0.1	6.15 ± 0.44	7.19 ± 0.62
0.1 - 0.2	5.46 ± 0.33	4.92 ± 0.39
0.2 - 0.3	5.83 ± 0.32	3.94 ± 0.32
0.3 - 0.4	5.68 ± 0.32	3.38 ± 0.29
0.4 - 0.5	5.55 ± 0.32	2.44 ± 0.26
0.5 - 0.6	5.50 ± 0.33	2.25 ± 0.24
0.6 - 0.7	5.70 ± 0.33	2.04 ± 0.23
0.7 - 0.8	6.40 ± 0.35	1.29 ± 0.19
0.8 - 1.0	5.34 ± 0.31	1.02 ± 0.15

x 10^{-39} x E cm^2/GeV

APPENDIX B

The measurements of the structure functions F_2 and xF_3 are given in bins of x and Q^2 in table 22. The errors correspond to the diagonal elements of the covariance matrix. In fits to the data the full covariance matrix has to be used, which can be supplied on request. The off-diagonal elements are large in some of the cases.

TABLE 22
Structure function data.

x	Q^2(GeV^2)	F_2	xF_3
0.00 - 0.05	0.1 - 0.3	1.01 ± 0.10	-
0.00 - 0.05	0.3 - 1.0	1.07 ± 0.07	-
0.05 - 0.10		0.74 ± 0.16	-
0.10 - 0.15		0.67 ± 0.23	-
0.15 - 0.25		1.21 ± 0.22	-
0.00 - 0.05	1.0 - 3.2	1.16 ± 0.07	0.33 ± 0.11
0.05 - 0.10		1.13 ± 0.08	-
0.10 - 0.15		1.03 ± 0.10	-
0.15 - 0.25		0.99 ± 0.10	-
0.25 - 0.40		0.50 ± 0.09	-
0.40 - 0.65		0.28 ± 0.09	-
0.00 - 0.05	3.2 - 10.0	1.15 ± 0.09	0.35 ± 0.10
0.05 - 0.10		1.31 ± 0.07	0.87 ± 0.11
0.10 - 0.15		1.09 ± 0.06	0.65 ± 0.13
0.15 - 0.25		0.94 ± 0.05	0.57 ± 0.15
0.25 - 0.40		0.67 ± 0.05	0.62 ± 0.23
0.40 - 0.65		0.28 ± 0.04	-
0.05 - 0.10	10.0 - 31.6	1.56 ± 0.11	0.97 ± 0.13
0.10 - 0.15		1.11 ± 0.06	0.67 ± 0.08
0.15 - 0.25		0.89 ± 0.04	0.65 ± 0.06
0.25 - 0.40		0.68 ± 0.03	0.61 ± 0.05
0.40 - 0.65		0.20 ± 0.02	0.13 ± 0.04
0.15 - 0.25	31.6 - 100.0	0.84 ± 0.07	0.70 ± 0.08
0.25 - 0.40		0.60 ± 0.03	0.51 ± 0.04
0.40 - 0.65		0.16 ± 0.02	0.13 ± 0.02
0.25 - 0.40	100.0 - 316.2	0.43 ± 0.19	0.54 ± 0.19
0.40 - 0.65		0.13 ± 0.03	0.12 ± 0.04

SUMMARY

In this thesis the results of an analysis of neutrino and antineutrino interactions on nuclei are presented. The data were taken with the calorimeter of the Amsterdam-CERN-Hamburg-Moscow-Rome (CHARM) collaboration at the narrow-band beam of the CERN SPS. The detector combines a large target mass with a high power of pattern recognition.

The presently accepted theory of weak interactions of Glashow, Salam, and Weinberg is introduced. Applications of the quark-parton model in the context of deep-inelastic neutrino interactions on nuclei are summarized. The concept of scaling and its consequences are mentioned. Some sources of scaling violations are discussed.

The properties of the narrow-band neutrino beam at CERN, which are relevant for the experiment are given. The neutrino energy spectrum and the flux monitors are described. A short overview of the components of the neutrino detector is given. The on-line data-handling of counter signals and the beam monitor information is summarized. The off-line data-analysis is described. The reconstruction of hadronic showers and the recognition of muons are presented together with the achieved resolutions.

Measurements of total cross-sections are presented. From the ratios of neutral-current and charged-current cross-sections of neutrinos and antineutrinos the coupling constants of the weak neutral-current are deduced. A significant contribution of the right-handed coupling is found. The relative strengths of the neutral-current and charged-current couplings are compatible with the Glashow-Salam-Weinberg model. The electroweak mixing angle, the only free parameter in this model, is deduced from the data. The results are in agreement with previously reported measurements from other experiments.

Some details of the methods used in the analysis of differential distributions are discussed. The differential charged-current cross-sections $d\sigma/dy$ and $d\sigma/dx$ are measured. The relative contributions of quarks and antiquarks to the neutrino cross-sections are deduced from the y-distributions.

Finally, the analysis of the structure functions is presented in terms of x and Q^2. Scaling violations are observed in qualitative agreement with QCD predictions. The mass-scale parameter of QCD, Λ, is obtained with the method of Buras and Gaemers. The results are in agreement with results obtained by other experiments. It is pointed out that the systematic uncertainties in the value of Λ are large, both due to experimental and theoretical uncertainties.

SAMENVATTING

In dit proefschrift worden de resultaten van een analyse van neutrino en antineutrino wisselwerkingen behandeld. De gegevens werden verkregen met de teller opstelling van de Amsterdam-CERN-Hamburg-Moskou-Rome (CHARM) samenwerking in de impuls-geselecteerde neutrino bundel van het Super Proton Synchrotron van CERN (Europese organisatie voor kern onderzoek, Geneve). De detector verenigt een grote doelwit massa met goede mogelijkheden voor patroon herkenning.

De op dit moment aanvaarde zwakke wisselwerkingstheorie opgesteld door Glashow, Salam en Weinberg wordt geintroduceerd. Toepassingen van het quark-parton model op diep-inelastische neutrino wisselwerkingen met kernen worden samengevat. Het begrip schaalinvariantie en de gevolgen daarvan worden genoemd. Sommige oorzaken van schaalbreking worden besproken.

De eigenschappen van de impuls-geselecteerde neutrino bundel van CERN, die voor dit experiment van belang zijn, worden behandeld. Het energie spectrum van de neutrinos en de bundel intensiteits monitoren worden beschreven. Een kort overzicht van de onderdelen van de neutrino detector wordt gegeven. De verwerking van de teller signalen en de bundel monitor gegevens gedurende de bestraling wordt samengevat. De analyse van de verkregen gegevens wordt beschreven. De reconstructie van hadronische lawines en de herkenning van muonen worden behandeld tezamen met de bereikte oplossende vermogens.

Metingen van totale werkzame doorsneden worden vermeld. De koppelings constanten van de zwakke neutrale stroom worden afgeleid van de verhoudingen van de totale werkzame doorsneden van neutrale en geladen stroom wisselwerkingen van neutrinos en antineutrinos. Een significante bijdrage van de rechtshandige koppeling is verkregen. De relatieve sterkten van de koppeling van de neutrale en geladen stroom zijn in overeenstemming met het Glashow-Salam-Weinberg model. De hoek, die de menging van de electromagnetische en zwakke wisselwerkingen bepaald - de enige vrije parameter van het model - is afgeleid van de gegevens. De resultaten zijn in overeenstemming met eerder gepubliceerde metingen van andere experimenten.

Details van de methode toegepast in de analyse van differentiele verdelingen worden besproken. De differentiele werkzame doorsneden $d\sigma/dy$ en $d\sigma/dx$ van geladen stroom wisselwerkingen zijn gemeten. De verhoudingsgewijze bijdragen van quarks en antiquarks tot de werkzame doorsneden van neutrino wisselwerkingen zijn bepaald aan de hand van de y-verdelingen.

Tot slot is de analyse van de x- en Q^2-afhankelijkheid van de structuur functies besproken. Schaalbreking is waargenomen, in qualitatieve overeenstemming met QCD voorspellingen. De parameter, Λ, die de massa-schaal van QCD beschrijft, is verkregen volgens de methode van Buras en Gaemers. De resultaten komen overeen met resultaten verkregen door andere experimenten. Er wordt op gewezen, dat de systematische onzekerheden in de bepaling van Λ groot zijn, zowel tengevolge van experimentele als theoretische onzekerheden.

ACKNOWLEDGEMENTS

It is a great pleasure to thank all the members of the CHARM collaboration and its many technical collaborators for the work they have done, which entered into this thesis.

In particular I would like to thank V.Blobel, P.D.Gall, H.Grote, B.Kröger, K.H.Mess, M.B.Metcalf, F.Niebergall, R.S.Orr, K.H.Ranitzsch, and K.Winter for their co-operation in this analysis.

I am grateful to Prof. dr. A.N.Diddens for his interest in the work and his valuable suggestions and discussions during the analysis and the writing of this thesis.

I would like to thank Prof. dr. J.C.Kluyver for the careful reading of the manuscript.

STELLINGEN

1. De gemeten absorptie breedtes van de 3d-niveaus van pionische atomen van zware kernen kunnen niet gereproduceerd worden door de standaard optische potentiaal berekeningen.

   J.Konijn et al., Nucl.Phys. A326 (1979) 401.
   J.H.Koch en F.S.Scheck, Nucl.Phys. A340 (1980) 221.

2. Bij het meten van quadrupool momenten van kernen uit Röntgenspectra van pionische atomen moeten alle zichtbare achtergrond lijnen nauwkeurig geanalyseerd worden. Hierdoor kunnen systematische fouten vermeden worden die kunnen ontstaan bij de analyse van het hyperfijn complex.

   R.Beetz et al., Nucl.Phys. A300 (1978) 369.
   S.C.Cheng et al., Hyperfine Interactions 4 (1978) 145.
   C.J.Batty et al., Nucl.Phys. A355 (1981) 383.

3. De door Baltay et al. gebruikte methode voor het verkrijgen van x-distributies van neutrale-stroom neutrino wisselwerkingen is fundamenteel onjuist.

   C.Baltay et al., Phys.Rev.Lett. 44 (1980) 916.

4. Bij het bepalen van het aantal gebeurtenissen veroorzaakt door elastische verstrooiing van muon-neutrino's aan electronen hebben Heisterberg et al. de achtergrond op onzorgvuldige wijze in aanmerking genomen.

   R.H.Heisterberg et al., Phys.Rev.Lett. 44 (1980) 635.

5. Gemeten frequentie verdelingen worden in de praktijk vaak gecorrigeerd voor meetonnauwkeurigheden door middel van een methode waarbij een gesimuleerde verdeling, die verkregen is door meetfouten in aanmerking te nemen, direct te vergelijken met de originele gesimuleerde verdeling zonder meetfouten. De experimenteel gevonden frequentie verdeling wordt dan vermenigvuldigd met correctiefactoren, berekend door het quotient te nemen van de originele gesimuleerde verdeling en de door meetfouten vervormde gesimuleerde verdeling. Deze veelvuldig toegepaste methode is incorrect wanneer de meetfouten niet "klein" te noemen zijn.

   J.G.H.de Groot et al., Z.Physik C1 (1978) 143.
   S.M.Heagy et al., Phys.Rev. D23 (1981) 1045.

6. De hoeveelheid cellen met dubbele micronuclei gevonden door I.Diehl-Marshall en M.Bianchi na het bestralen van de wortelpunten van Vicia faba met neutronen afkomstig van 600 MeV protonen kan eenvoudig verklaard worden door aan te nemen dat de twee micronuclei veroorzaakt zijn door twee ongecorreleerde processen.

   I.Diehl-Marshall en M.Bianchi, Induction of micronuclei by irradiation with neutrons produced from 600 MeV protons, CERN-preprint 1980 HS-RB/020/RP, to be published in Brit.J.Radiol.

7. De biochemische zuiveringsmethoden en de biologische test gebruikt door M.Riedel et al. voor het aantonen van cytokinines, waarop de conclusie gebaseerd is dat de radiorestauratieve werking van gistextracten en de daaruit geïsoleerde bestanddelen zoals tRNA en mengsels van aminozuren toegeschreven kan worden aan hun cytokinine gehalte, zijn niet voldoende selectief. Ook andere moleculen, met name polyamines, kunnen zowel door de gebruikte methode geïsoleerd worden als positief op de biologische test reageren.

   M.Riedel et al., C.R.Acad.Sc. ser.D Paris 284 (1977) 1457.
   J.Jänne, M.Pösc en A.Raina, Biochimica et Biophysica Acta 473 (1978) 241.

8. Voor het overtuigend aantonen van gebeurtenissen die duiden op het verval van een proton is het aan te bevelen behalve de sporen ook de bewegingsrichting van de deeltjes langs het spoor in de detector te bepalen. Dit kan verwezenlijkt worden door van elk tellersignaal niet alleen de plaats, maar ook de tijd te meten.

9. Zolang de massa's van de verschillende typen neutrino's niet experimenteel bepaald zijn blijven alle modellen die de vorming van melkwegstelsels beschrijven speculatief.

   D.N.Schramm en G.Steigman, Astroph.J. 243 (1981) 1.
   F.R.Klinkhamer en C.A.Norman, Astroph.J. 243 (1981) L1.